Advances in experimental characterization and modelling of FRCM composites for structural retrofitting

Ph.D thesis submitted to the University of Palermo

by

Maria Concetta Oddo

Coordinator: Prof. Antonina Pirrotta

Tutors: Proff. Lidia La Mendola and Giovanni Minafò
University of Palermo
and
Prof. Catherine Papanicolaou
University of Patras

Maria Concetta Oddo
Palermo, 3 February 2023
e-mail:mariaconcetta.oddo01@unipa.it
e-mail:oddocetta@yahoo.it

Thesis of the Ph.D. course in *Civil, Environmental, Materials Engineering - Structural and Geotechnical Engineering*
(Ingegneria Civile, Ambientale, dei Materiali - Ingegneria Strutturale e Geotecnica)
Dipartimento di Ingegneria
Università degli Studi di Palermo
Viale delle Scienze, Ed.8 - 90128 Palermo, ITALY

Written in LaTeX
Examples and figures made with *Grapher*© and *Adobe Illustrator*©

A MIA MAMMA
IN QUESTO TRAGUARDO C'È ANCHE UN PEZZETTO DI TE

Come un aquilone senza corda
e una farfalla senza ali,
mia madre mi ha insegnato a volare con i sogni.
(William H. McMurry III)

SUMMARY

During the last decades, the use of Fabric Reinforced Cementitious Matrix (FRCM) in the field of structural retrofitting has became a wide-spread practice. The FRCM strengthening systems consist in fibre grids with various nature embedded between two layers of inorganic matrix based on lime or cement binders. They offer an improved compatibility with the substrate, especially masonry support, allowing to overcame some of the drawbacks related to the use of the well known Fibre Reinforce Polymers (FRPs).

Despite their growing popularity, the constitutive behaviour is not yet adequately studied due to the complex mechanisms established at the fibre-matrix and composite-support interface level. The available literature highlights an huge scatter of the experimental results, often associated with the inherent variability of the FRCM systems. Moreover, the technical codes still present numerous uncertainties resulting in several issues for the practice of qualification and the design procedures.

This thesis presents the results of an experimental campaign focused on the tensile characterization of basalt and glass FRCM and composite-calcarenite bond characterization (Chapter 2 and 3). The experimental work is complemented by the proposal of two numerical models both for tensile and bond tests, presented in Chapter 4.

The experimental investigation was carried out considering the influence of different reinforcements, matrices and testing methods. Experimental results provide for assessing the effect of mortar grade on the stress-strain curves, strength, ductility and failure modes. Moreover, the thesis provides an important contribution to assess the influence of different testing methods (i.e. clamping and clevis as reported by different standard and guidelines) on the performance of the FRCM systems tested in tension.

Moreover, the Digital image correlation was used to measure the tensile strains and to analyse the failure modes offering an accurate mechanical characterization.

The main element of novelty in Chapters 2 and 3, is the adoption of a modified bond test set-up designed to analyse the influence of the composite size on bond length and strength. A deep analysis of the results confirms the effectiveness of this innovative set-up.

Finally, two numerical models are presented in Chapter 4, attempt at providing a simple numerical tool for capturing the constitutive behaviour of the

FRCM systems. The models were calibrated on the basis of the experimental stress-strain and load-slip curves showing to be an effective tool for predicting the mechanical behaviour of the FRCM composites.

Contents

List of Figures

List of Tables

Index of symbols

Uppercase English Letters

Cross sectional area of bare textile	A_f
Cross sectional area of mortar matrix	A_m
FRCM bond width	B
Modulus of elasticity of the fibre	E_f
Modulus of elasticity of the mortar matrix	E_m
Modulus of elasticity of calcarenite stone	E_s
First cracking load in the mortar matrix	F_{cr}
Discrete value of fibre-matrix interface stiffness	$K_{D,fm}$
Discrete value of matrix-support interface stiffness	$K_{D,ms}$
FRCM bond length	L
Length of the FRCM coupons	L_{FRCM}
Debonding load	P_{deb}
Peak load at the end of Stage I in FRCM characteristic curve	P_I
Peak load at the end of Stage II in FRCM characteristic curve	P_{II}
Peak load at the end of Stage III in FRCM characteristic curve	P_{III}

Lowercase English Letters

Width of FRCM strip	b
Tensile strength of the fibre	f_{fu}
Compressive strength of the mortar matrix	$f_{m,c}$
Flexural strength of the mortar matrix	$f_{m,f}$
Tensile strength of the mortar matrix	$f_{m,t}$
Compressive strength of calcarenite stone	$f_{s,c}$
Continuous value of fibre-matrix interface stiffness value	$k_{C,fm}$
Continuous value of matrix-support interface stiffness value	$k_{C,ms}$
Maximum slip at the fibre-matrix interface	s_{int}
Equivalent dry thickness of the fibre	t_f
Thickness of the mortar matrix	t_m

Lowercase Greek Letters

Ultimate tensile strain of the fibre	$\varepsilon_{f,u}$
Conventional strain limit of strengthening element with FRCM	$\varepsilon_{lim,conv}$
Strain at transition point Stage I-II of FRCM characteristic curve	ε_I
Strain at transition point Stage II-III of FRCM characteristic curve	ε_{II}
Ultimate strain at Stage III in FRCM characteristic curve	ε_{III}
Conventional stress limit of strengthening element with FRCM	$\sigma_{lim,conv}$
Stress at transition point Stage I-II of FRCM characteristic curve	σ_I
Stress at transition point Stage II-III of FRCM characteristic curve	σ_{II}
Ultimate stress at Stage III in FRCM characteristic curve	σ_{III}
Maximum shear stress at the fibre-matrix interface	τ_{max}
Maximum shear stress at the matrix-support interface	$\tau_{max,ms}$

Introduction

The adoption of composite materials for structural retrofitting has become today a common usage in the most of engineering applications which aim to preserve the built environment. In this context, the development of alternative techniques for the structural rehabilitation of monuments and historical buildings has emerged as a crucial point of the engineering practice, when technicians need to take particular care in the application of externally bonded materials to stone or masonry supports.

The need of these alternative methods and materials led recently to the rapid growth of the interest on the possibility of using composite materials made up with a fibre grid of various nature and an inorganic matrix instead of the resins. These materials are known in the literature as Fabric-Reinforced Cementitious Matrix (FRCM) but often referred also as TRC (Textile Reinforced Concrete), TRM (Textile Reinforced Mortars), FRM (Fabric Reinforced Mortar) or even IMG (Inorganic Matrix-Grid composites).

FRCM composites are the result of coupling nets, made with long fibres with an inorganic matrix based on lime or cement binders. The interest and the attention of the technical community is demonstrated by the rapid development of recent International Standards, which aim to define the experimental procedures and methods for assessing the constitutive behaviour of FRCM materials. The provisions reported in these Standards are the summary of a huge amount of research work developed in the last years, which aimed to investigate the role of all the test variables on the mechanical behaviour of FRCM composites and establish the most suitable test configurations.

Despite this great research effort, several aspects related to the constitutive characterization of FRCM composites are still under discussion. As an example, some typologies of stone are not considered for the bond test from the Italian Guidelines for qualification of materials, and specific indications are not provided for the calcarenite stone masonry, which by contrast is particularly diffused and common in historical buildings in Sicily and in the overall Mediterranean area.

Apart from the experimental characterization, it is also observed that a few of modelling approaches were developed in the literature for representing the constitutive behaviour of FRCM materials, going from detailed Finite Element (FE) micromodels to simplified analytical approaches, pointing out as a reference study for a simple yet accurate numerical modelling method is still missing

or under study.

On these basis, this thesis aims to contribute to the advance of the knowledge of the mechanical behaviour of FRCM composites for structural retrofitting applications by studying in deep their constitutive characterization and the bond behaviour from both an experimental and a numerical point of view.

In particular, the first part of the work is devoted to perform an experimental comparative evaluation of the tensile behaviour by adopting the two main test setups available in the literature, namely the "clamping grip" and the "clevis" method. Contextually, two different test methods are also studied for investigating the bond behaviour of FRCM composites applied on a calcarenite stone support. In this field, a new set-up is proposed for double lap shear bond test, aiming to minimize the weight of the testing apparatus. The overall experimental study, including tensile and bond tests, is carried out on different types of FRCM, made up by combining a glass or a basalt fiber grid with a cement or lime-based mortar matrix, examining the role of the constituent materials on the test results. The outcomes of the different test methods are compared, assessing the effectiveness in reproducing the tensile or bond behaviour and the dependence of the results from the testing apparatus.

In the final part of the work, two numerical models are developed to predict the tensile and the shear bond behaviour by exploiting a simplified FE approach. Both models are developed with the aim of reducing the computational effort and providing an easy-reproducible and implementable model by using simple truss elements and shear zero-thickness discrete interface elements. It is shown as the adoption of this approach combined to a careful evaluation of the interface constitutive law allows to predict the experimental response of the FRCM systems under tension.

Chapter 1

Constitutive characterization of FRCM systems: state of the art

During the last decade, FRCM systems gained an increasing popularity among the composite materials for structural retrofitting.

A huge amount of experimental works was performed on their characterization and on the evaluation of their efficiency for structural retrofitting applications.

In spite of their growing spread, the modelling and characterization of the mechanical response of these innovative composites are still open issues, due to the inner mechanical complexity of the stress transfer mechanisms between fabric, matrix and support. For these reasons, several experimental studies were addressed to the mechanical characterization for the homologation and the acceptance of FRCM composites, with particular reference to their tensile and shear bond behaviour.

In this chapter, FRCM composites are presented with reference to their main physical and mechanical characteristics. An overview of the possible test methods for their characterization according to the current regulations is provided. The most important experimental studies are analyzed, focusing on the outcomes from tensile and shear bond tests as a function of different parameters, such as the test set-up, nature and treatment of fabric, mortar grade, influence of bond length, characteristics of the substrate. Finally, a short overview of the main theoretical studies for predicting the mechanical behaviour of FRCM materials is presented.

1.1 The mechanical behaviour of FRCM composites

FRCM materials consist of high strength textiles from various nature (e.g. basalt, glass, carbon, polyparaphenylene benzobisoxazole (PBO), aramid) embedded in an inorganic matrix (e.g. cement/lime based mortar, polymer-modified or fibre-reinforced mortar).

The FRCM composites represent a possible alternative and cost effective solution to the already widely used Fiber Reinforced Polymer (FRP) materials, for structural retrofitting of existing buildings, with particular reference to masonry structures.

Indeed, the inorganic matrix replacing the epoxy resin, offers numerous advantages due to the good compatibility with the masonry substrate, ensuring a better vapor permeability, adequate durability to external agents, good fire resistance and the reversibility of the intervention. From a structural point of view, it is well-known that the efficiency of a strengthening technique is usually based on the capacity of the newly added material to carry tensile loads and consequently to give the member an increase of structural performance. In this context, the tensile behaviour of FRCM materials is particularly complex and affected by the inner stress transfer mechanisms which develop in the materials. In fact, when the FRCM is loaded in tension, cracks are expected to open in the mortar matrix. Consequently, the compatibility with the fiber fabric is lost and the fabric can slip over the surrounding matrix. The capacity of the FRCM to keep carrying the external load is related to the capacity of the fabric-to-mortar interface to transfer stresses between the two materials.
Additionally, it should be noted that when externally-bonded applications are considered, an additional stress-transfer plane is expected between the FRCM and the support material. As a consequence, the overall capacity of the strengthened member is related to the capability to avoid the detachment from the supporting material, carrying bond stresses at the interface between the FRCM and the support.
In this background, it is evident that the mechanics of FRCM systems is particularly complex and affected by several phenomena. The failure mode of a FRCM material subjected to uniaxial tension cannot be defined uniquely, but depends on the attainment of the ultimate capacity of one the above-described mechanisms (i.e. tensile failure of the fabric, fabric-to-matrix slip, matrix-to-support interface failure) and consequently on the different mechanical and geometrical properties of the FRCM (e.g. properties and geometry of the fabric, mortar grade and composition, nature of the substrate).

On these basis, it is clear that the development of reliable design procedures and proper applications of these innovative strengthening systems requires a careful evaluation of the constitutive tensile behaviour of the FRCM systems and the shear bond behaviour between FRCM system and the support.

1.2 Procedures for the experimental characterization of FRCM composites

The need of assessing the constitutive behaviour of FRCM materials moved the interest of the technical and scientific community to the development of standardized test methods and acceptance criteria for defining experimentally the mechanical behaviour of FRCM materials.
Generally, all the technical standards suggest to assess the mechanical behaviour of FRCM materials through two types of tests:

- uniaxial tensile test;
- single lap or double lap shear bond test.

In particular, two tensile test set-ups are available and each provides different results. Tensile tests according to Italian Guidelines [8] are performed adopting the clamping-grip method , which provides the application of a compressive pressure in the gripping area of the specimen ends. This solution improves the shear stress transfer mechanism at the fibre-mortar interface, preventing fibres slippage [10] [11]. Differently, the American Standards [2] suggests to perform tensile test by adopting the clevis-grip method. In this case, the load is transferred from the testing machine to the mortar by shear adhesion. It is evident that the two methods led to different stress transfer mechanisms and consequently the trend of recorded response can be different.

The effectiveness of the FRCM systems relies not only in the fiber-matrix interaction but also in the composite-to-substrate bond strength. This last is evaluated by performing shear bond tests with the support. In spite the drafting of some general test set-up guidelines [8] [12] [2], the available technical documents are still generic and show some uncertainty. Italian Guidelines [8] provides a classification for shear bond test on concrete, tuff masonry elements, clay brick and natural stone masonry. However, standard procedures to perform shear bond tests on other types of masonry, such as on calcarenite, are still missing. Indeed, the calcarenite have physical and mechanical properties

different from tuff or other natural stone, establishing a different bond strength with the FRCM system. Due to it is very widespread as building material in the Mediterranean area, detailed recommendations also on the performance of bond test on calcarenite are needed.

The currently available test procedures are described in the following, examining their specialities and characteristics.

1.2.1 Characterization of the tensile behaviour

Uniaxial tensile tests are useful to characterize and compare various matrix-fiber combinations as well as to deduce the mechanical properties for design applications.

Several procedures were proposed in the literature examining their capability in providing a reliable tensile response FRCM system [10] [11] [13]. Generally, the test set-ups differ based on the test configuration, gripping method, displacement rate, measurement system, sample shape and size.

As discussed above, standards provide two different setups based on the grip methodology, namely the clamping and clevis grip method.

The clamping grip method recommended by Italian Guidelines [8] suggests inducing a compressive pressure at the specimen ends trough mechanical or hydraulic wedges in order to prevent any slippage or rotation of the specimen (Figure 1.1).

In this case, the specimens have a minimum free length equal to four times the width and the minimum width is at least four times the mesh size of the fibre grid. The specimens are equipped with metal tabs with a minimum length of 80 mm, glued at the ends to ensure an appropriate distribution of the clamping pressure and minimize any damage caused by possible local crushing.

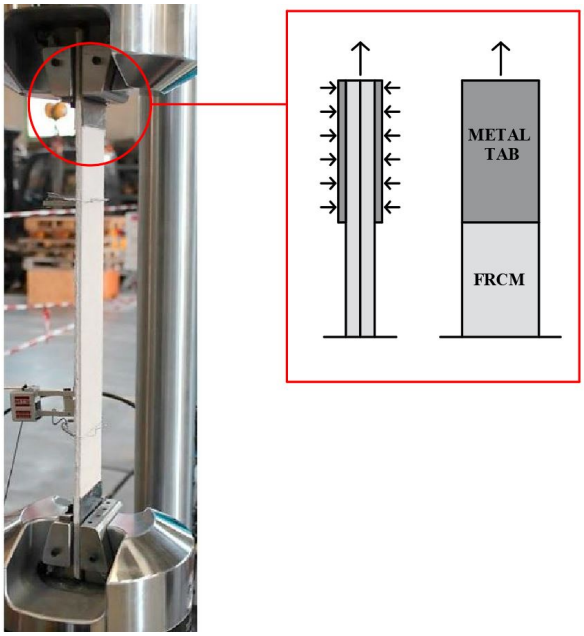

Figure 1.1: Tensile test set-up: clamping grip. (Bellini et al. 2019 [1])

The clevis grip method, as recommended by American standard ACI 549 [2] (Figure 1.2), involves the transfer of the tensile force through shear adhesion by using metallic plates bonded at the coupon's ends and connected by a transversal pin to the testing machine frame.

This test set-up allows a rotational degree of freedom in plane to the specimens in order to reduce possible parasitic bending moments, as well as the one recommended by RILEM TC 232-TDT [4] (Figure 1.3).

The tests are carried out on specimens with a length to width ratio of at least 5:1. The minimum width of the specimens is 60 mm and the minimum length is 500 mm, ensuring at the ends an anchorage length at least 125 mm. The thickness can vary depending on the textile layers but must not be less than 6 mm.

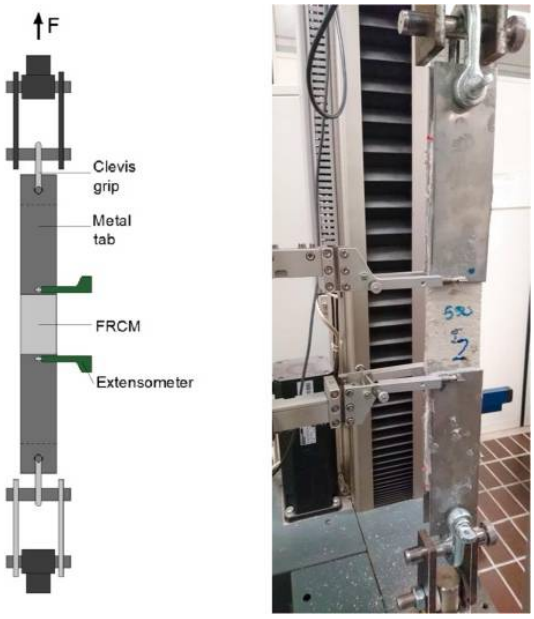

Figure 1.2: Tensile test set-up: clevis grip, according to ACI 549 [2]. (Donnini et al. 2019 [3])

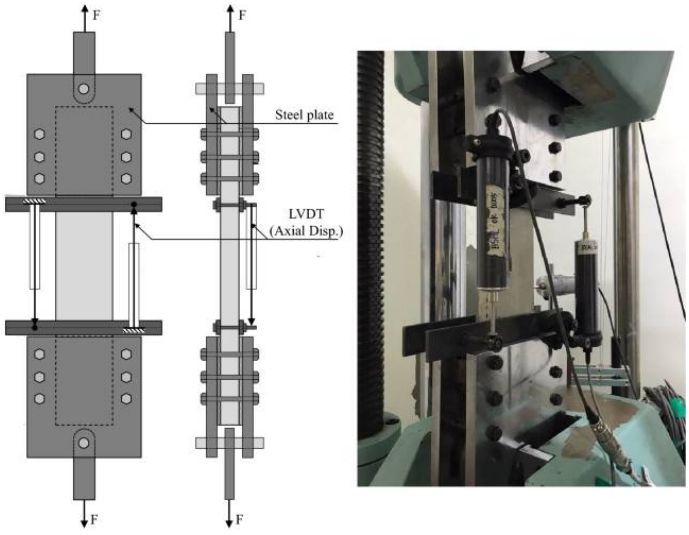

Figure 1.3: Tensile test set-up: clevis grip, according to RILEM TC 232-TDT [4]. (Kim et al. 2018 [5])

The typical stress-strain response obtained from tensile test assumes a tri-linear trend consisting in three consecutive stages, as shown in Figure 1.4(a). The first uncracked stage is characterized by a linear branch up to the first cracking load in the mortar layers. In the second stage the stiffness decreases significantly. The length and slope of this branch strictly depend on the adhesion properties established between fibre and matrix and the volume percentage of fibres activated for the load transfer. This phase is generally characterized by the opening and propagation of several cracks in the mortar layers. Finally, the third stage is mainly governed by fibre textile. For this reason, the slope of third branch often reflects the elastic modulus of the bare fibre textile. Moreover, during this phase no new crack appears.

With reference to grip method, when the clevis grips are used, a less evident second stage develops and the tensile curve assumes a more bi-linear trend, as shown in Figure 1.4(b). This circumstance is due to the load transfer through adhesion and shear stress, causing the slippage of the fibre within the matrix.

Results from tensile tests are used to determine the following mechanical properties, with the symbol meaning in the Figure 1.4:

- elastic modulus in the first stage, referred as E_1;
- ultimate stress and corresponding strain of FRCM system, referred as σ_u and ε_u respectively.

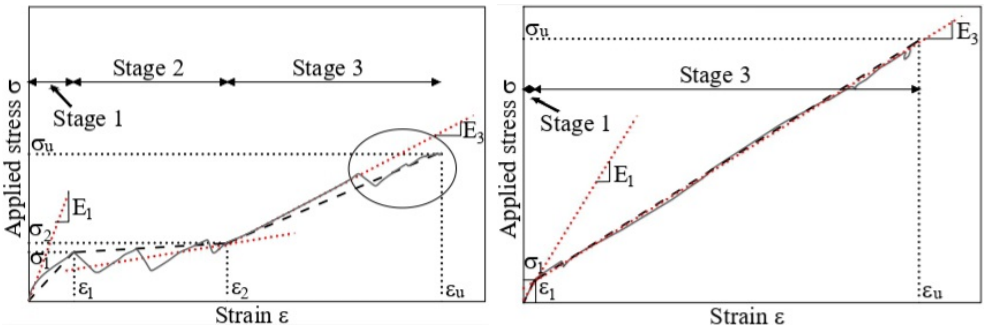

(a) Tri-linear stress-strain response **(b)** Bi-linear stress-strain response

Figure 1.4: Tensile behaviour of FRCM composites. (D'Antino and Papanicolaou 2017 [6])

Suitable monitoring tools are request in order to investigate the heterogeneous behaviour of the FRCM composites tested in tension. Generally, tradi-

tional measurement systems are used for the acquisition of displacement and local strains, such as displacement transducers and strain gauges. The reliability of displacement transducer measurements is strongly affected by the position of the transducers, which is determined by the cracking pattern, but this was unknown prior to the test [14]. Differently, strain gauges are able to measure only local values.

For these reasons, in some case the classic acquisition methods have proven insufficient to monitor FRCM materials during the tensile tests. Recently, innovative monitoring methods, such as the Digital Image Correlation (DIC) technique, have been combined with the use of traditional measurement systems. Numerous available studies have demonstrated the effectiveness of this technique [15] [11] [3] [16] in providing the global response and the evolution of the cracking pattern through a field analysis of the displacements or strains.

1.2.2 Characterization of the shear bond behaviour

The tensile tests are insufficient to properly characterize the mechanical behaviour of the FRCM systems. The use of FRCM materials, as strengthening system for structural elements, needs the assessment of the shear bond in order to take into account the different failure modes in function of the interaction between the support and the FRCM system. The adhesion properties at the matrix-substrate interface and the interaction between fibre and matrix play a foundamental role in the FRCM-to-substrate load transfer mechanism. The bond behaviour of FRCM-support was studied extensively using single and double shear bond test [17] [18] [19] [20] [21] [22]. Available experimental results demonstrated that the failure may occur both at the FRCM-substrate interface and within the thickness of the FRCM composite.

Recommendations of RILEM TC 250-CSM [7] identify the practice to perform shear bond tests. Samples consists in a prismatic substrate, as shown in Figure 1.5. The FRCM system is applied on one side of the prismatic support ensuring at least a bond width B of 40-100 mm and a bond length L of 250 mm to guarantee that the load transfer capacity from the FRCM system to the substrate is exploited as effectively as possible.

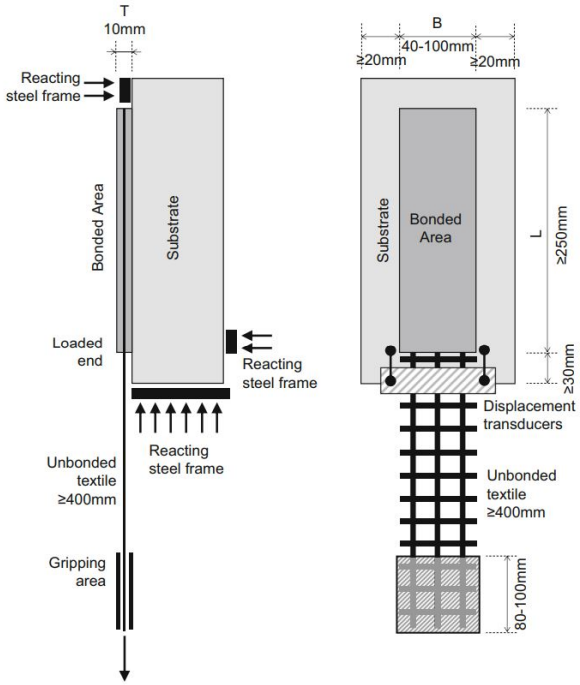

Figure 1.5: Recommended specimen's geometry from RILEM TC 250-CSM [7].

The typical stress-slip response obtained from shear bond test assumes the trend schematized in Figure 1.6.

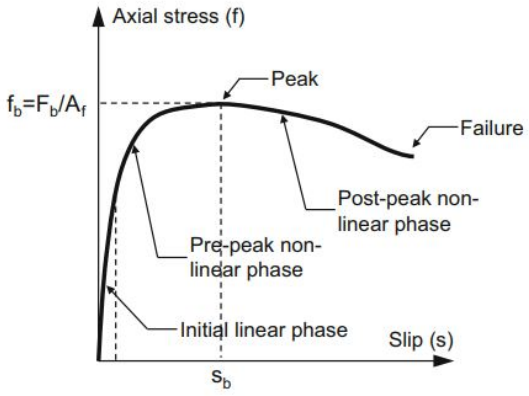

Figure 1.6: Schematic axial stress-slip relationship from RILEM TC 250-CSM [7].

The stress values are referred to the the cross-sectional area of the fibre grid A_f and the slip is the relative displacement between the textile and the substrate.

Generally, an initial linear phase is observed, followed by a non-linear trend up to the peak stress value. Then, a descending post-peak branch starts in which an increase in slip is associated with a decrease in stress up to failure, as shown in Figure 1.6.

As recommended by Italian Guidelines [8], results from shear bond tests combined with those of uniaxial tensile tests are useful to determine the following mechanical properties (Figure 1.7):

- conventional stress limit $\sigma_{lim,conv}$ which is the stress value related to the maximum load transferred from the strengthened element to the externally bonded FRCM system;
- conventional strain limit $\varepsilon_{lim,conv}$, calculated by dividing the $\sigma_{lim,conv}$ by the elastic modulus of fibre textile E_f;
- ultimate tensile stress $\sigma_{u,f}$ and corresponding strain $\varepsilon_{u,f}$ of fibre grid.

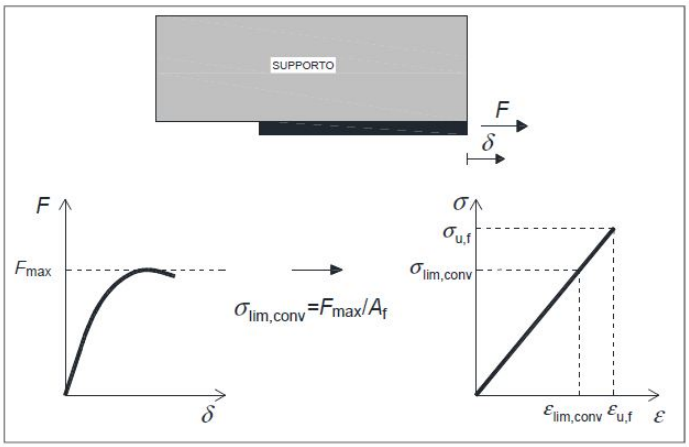

Figure 1.7: Determination of $\sigma_{lim,conv}$ and $\varepsilon_{lim,conv}$ according to Italian Guidelines [8]

being $\sigma_{u,f}$ and $\varepsilon_{u,f}$ the ultimate tensile stress and strain of dry fibres.

In conclusion, shear bond test provides information about the failure mode that governs the FRCM bonded to the substrate load transfer capacity. Recommendations of RILEM TC 250-CSM [7] classify the failure modes as shown in Figure 1.8:

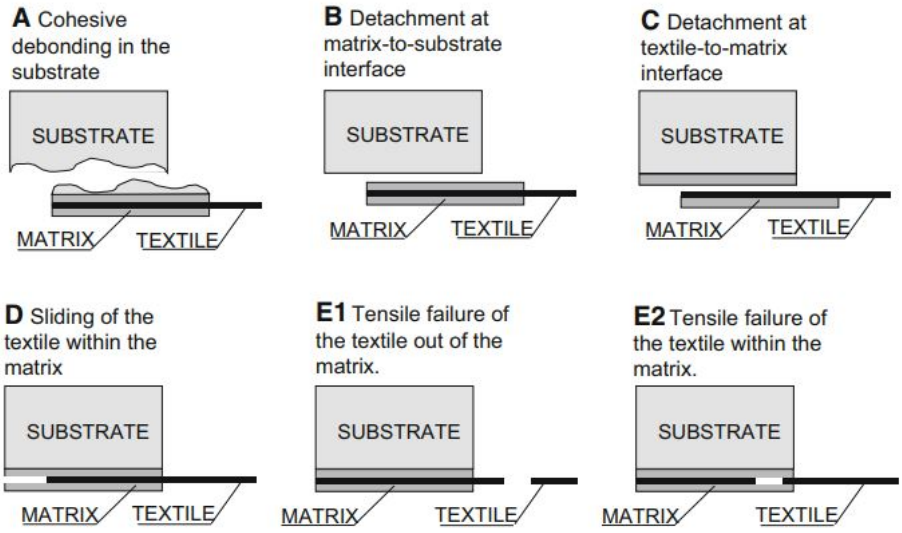

Figure 1.8: Classification of failure modes according to RILEM TC 250-CSM [7].

- (A) debonding at the matrix-support interface with the cohesive failure of the substrate;
- (B) debonding at the matrix-support interface;
- (C) debonding at the fibre-matrix interface;
- (D) fibre slippage within the matrix;
- (E1) tensile rupture of the un-bonded fibre textile;
- (E2) tensile failure of the fibre textile within the matrix layers.

Apart from this classification, combined failure modes may occur. Various testing factors can influence the repeatability of the results, such as specimen preparation, boundary conditions (e.g. clamping system) and measurement techniques, as highlighted by results from several experimental works [17] [23] [24].

1.3 Available experimental studies: an overview

Numerous experimental studies were carried out with the aim of investigating the different parameters involved in the tensile and shear bond behaviour of FRCM systems. The state of the art points out as the constitutive behaviour of FRCM materials depends on several parameters: the fibre nature and treatment [1], the mortar type, the volume percentage of fibre reinforcement [25], the nature of the support [26] and the test method [10] [22].

Several studies were carried out on the kind of fibre, such as basalt [15] [17] [27], glass [1] [11], carbon [1] [28] and PBO [29] [30] and the effect produced by fibre treatments or the use of adhesion promoter.

In general, it is observed that dry fibres have a poor chemical-physical compatibility with inorganic matrices. This can compromise the performance of the FRCM systems providing the slippage at the matrix-fibre interface, the debonding or the telescopic failure caused by the the slippage of among filaments in the yarns. The bond between the fibres and the matrix is essential to ensure the effectiveness of the reinforcement system. Available experimental studies have shown that the pre-impregnation of fibre yarns with epoxy resin or the use of adhesion promoter is an effective solution, to improve both the tensile strength of the fibre yarn and the adhesion with the mortar, avoiding the premature failure of the composite system [31]. These effects can be attributed to the ability of the epoxy resin and the adhesion promoter to penetrate between the dry filaments of the yarn, ensuring a more homogeneous impregnation of the fibres and compatibility with the mortar [1].

Also the volume percentage of fibre plays a fundamental role in the constitutive behaviour of the FRCM composites. It significantly affects the strength, the failure mode and the cracks pattern of the coupons. Experimental studies demonstrated, that numerous cracks develop in specimens with more multiple layers of fibre grid and that the second stage is concentrated in a shorter strain interval. The increment of reinforcing textile ratios in the FRCM composite not always produces a benefit, as shown in available experimental studies, it can reduce the bond strength between the textile and the matrix and promotes premature slippage of the fabric before reaching the tensile strength of the fibre [25].

Moreover, numerous experimental campaigns were carried out with the aim to evaluate the effectiveness of different test configurations (single or double shear bond test) , instrumentation (i.e. different clamping systems for unbonded textile were used) and measurement techniques in order to overcome

some issues in test set-up, such as the presence of an eccentric load. The latter can compromise the proper transfer of a pure shear stress state at the FRCM strengthening system applied on a support due to possible out-of-plane tensile stress generate by bending.

In general, a large scattering is observed due to numerous variables involved in the mechanical characterization of FRCM. Available literature highlights different failure modes, involving the textile-to-mortar or the mortar-to-substrate interface, or also the slippage of the fibre grid [22] [17] [32]. For these reason, further investigations are needed in order to improve the test procedures provide in the current FRCM qualification guidelines, reaching a high level of standardization and reducing experimental scattering.

1.4 Available analytical and numerical studies: an overview

As above mentioned, numerous experimental studies were proposed to investigate the key parameters affecting the mechanical characterization of FRCM composites. By contrast, fewer works were addressed to analytical or numerical approaches for modelling the constitutive behaviour of FRCM composites.

Among the recent studies, two general approaches are proposed: simplified analytical methods or detailed numerical models.

Simplified analytical formulations proposed in the past [27] [33] are revisited with aim to predict the typical tri-linear tensile behaviour of the composite systems. They are based on the well-know rules adopted for reinforced concrete members: Aveston-Cooper-Kelly (ACK) Model [34], model proposed by Minafò and La Mendola [33] and Tension Stiffening Model [35].

A literature review study [36] focused on the comparisons with an experimental database, highlighting that the three analytical models allow to estimate with enough accuracy the tensile behaviour of the FRCM systems but with several limitations. Indeed, the three models are unable to take into account the influence of the the complex mechanisms of interaction between fibre textile and mortar.

Other works are based on numerical approaches, based on 3D or 2D FE models [37] and non-linear micro-mechanical models [38]. An accurate response is obtained from the use of the multi-scale approach for modelling the bond behaviour between the FRCM system and the strengthening support [29] and the FRCM tensile behaviour [39] [37].

In these cases, each constituent material is modelled separately with the most suitable finite elements, often brick elements for mortar and shell ele-

ments for fibre. The interface between two materials in contact is modelled as a zero-thickness layer, assigning the corresponding contact properties to each interface level. Generally, a cohesive interface with damage between fibre and mortar is assumed and Concrete Damage Plasticity model for simulating the tensile behaviour of the mortar. The models provide quite good prediction of the global response and the local non-linear behaviour at the interface level, well simulating the crack pattern. However, these modelling approaches require long computational time including convergence issues. Moreover, these models also need the definition of variables that are often unknown and require to be experimentally calibrated or tentatively estimated, resulting in some unreliability.

More recent studies proposed also uniaxial models and numerical strategies to solve the governing equations of FRCM strips under different loading conditions. Grande and Milani (2020) [40] proposed a procedure to solve a system of differential equations derived by equilibrium considerations involving the main components of a FRCM system, i.e. fibre, mortar and fibre-mortar interface, where specific constitutive laws and boundary conditions, also accounting for the occurrence of damage, are introduced. This approach shows a certain reliability in predicting the experimental response emphasizing the important aspects concerning the local behavior of FRCM systems in presence of possible softening behaviour of both the mortar and the fibre-mortar interface.

Chapter 2

Experimental investigation

This chapter presents the details of an extensive experimental study performed on the characterization of different types of FRCM composites evaluating their effectiveness when applied on masonry support. In particular, Basalt-FRCM (BFRCM) and Glass-FRCM (GFRCM) characterized by a bi-directional fibre grid embedded inside two mortar types: a two-component fibre-reinforced cementitious mortar and a two-component fibre-reinforced natural hydraulic lime-based mortar.

The aim of the investigation is to compare the performance of different FRCM systems, evaluating the influence of mortar type (cement based or hydraulic lime based), fibre nature (basalt or glass) and test set-up.

Finally, a new proposal of set-up for shear bond test is presented, aiming to improve the experimental existing set-ups for bond characterization.

2.1 Material characterization

The mechanical properties of all materials adopted in the current experimental campaign are experimentally evaluated. The main physical and mechanical properties are presented in the following sections.

2.1.1 Fibres

Two fibre grids were adopted in the current experimental investigation, one of basalt an the other one of glass. In this section the main features are presented.

A coated bi-directional alkali-resistant basalt fibre grid (Figure 2.1(a)) is adopted as internal reinforcement for BFRCM composite systems. The textile have a mesh size of 6×6 mm, the longitudinal and transversal yarns are woven

and fixed at their intersection with nylon fibres. It is characterized by a weight of 250 g/m^2, density equal to 2.75 g/cm^3 and equivalent fibre thickness (i.e. the thickness of the fibre textile assumed as the fibres were uniformly distributed in the section) of t_f=0.039 mm. An Alkali Resistant (AR) dry glass fibre mesh (Figure 2.1(b)) is employed for GFRCM strengthening systems. The mesh grid is termowelded along the weft at the joint between longitudinal and transversal yarns, the cell size is 12×12 mm, the unit weight of 220 g/m^2, the density of 2.5 g/cm^3 and the equivalent fibre thickness equal to t_f=0.02 mm.

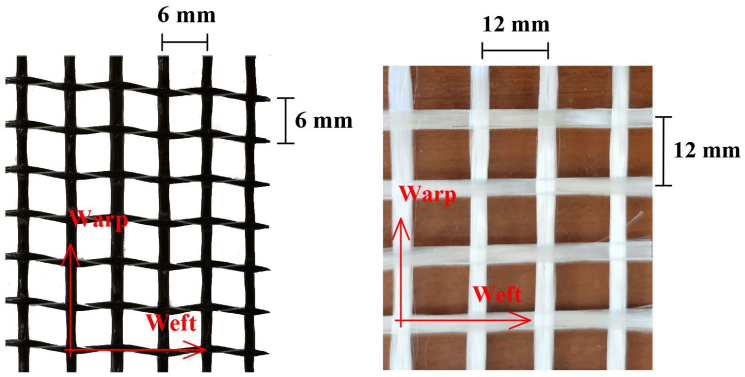

(a) basalt grid **(b)** glass grid

Figure 2.1: Fibre mesh.

Mechanical properties of basalt grid reported in technical data sheet are: tensile strength f_{fu}=60 kN/m, ultimate strain ϵ_{fu}=1.8% and elastic modulus E_f=89 GPa. The manufacturer data are summarized in Table 2.1.

Table 2.1: Mechanical properties of basalt fibre grid provided by the manufacturer.

Basalt fibre grid					
Unit weight	Density	Equivalent thickness	Tensile strength	Ultimate strain	Elastic modulus
[g/m^2]	[g/cm^3]	t_f [mm]	f_{fu} [kN/m]	ϵ_{fu} [%]	E_f [GPa]
250	2.75	0.039	60	1.8	89

The mechanical properties from data sheet, referred to glass fibre are: tensile strength f_{fu}=56 kN/m, ultimate strain ϵ_{fu}=2.0% and elastic modulus E_f=74 GPa. The manufacturer data are summarized in Table 2.2.

Table 2.2: Mechanical properties of glass fibre grid provided by the manufacturer.

Glass fibre grid					
Unit weight	Density	Equivalent thickness	Tensile strength	Ultimate strain	Elastic modulus
$[g/m^2]$	$[g/cm^3]$	t_f [mm]	f_{fu} [kN/m]	ϵ_{fu} [%]	E_f [GPa]
220	2.50	0.02	56	2.0	74

The mechanical properties of fibre grids were experimentally evaluated by performing uni-axial tensile tests on a total of eighteen coupons: i.e. nine samples of basalt fibre grid and nine samples of glass fibre grid. Specimens have dimensions of 50×400 mm, in accordance with Italian guidelines [8], as shown in Figures 2.2(a) and 2.2(b).

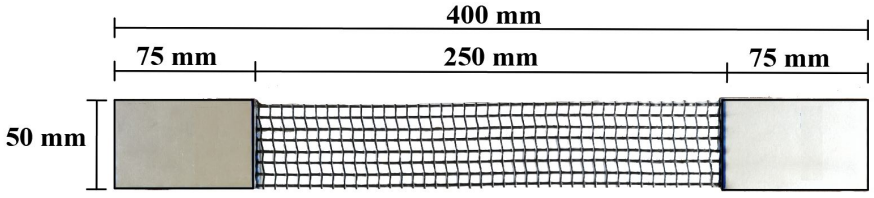

(a) basalt

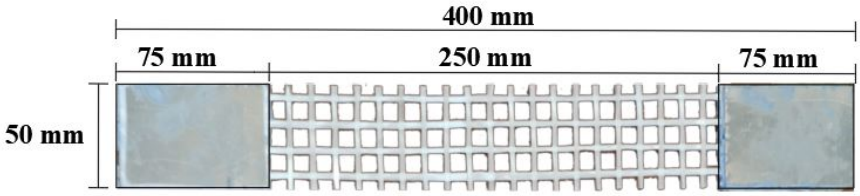

(b) glass

Figure 2.2: Geometry of fibre coupons.

Moreover, aluminium tabs, with thickness of 2 mm and bond length equal to 75 mm, were glued at the ends of fibre strips to promote a uniform load distribution between the yarns.

Monotonic tensile tests were performed under displacement control by a universal testing machine with force capacity equal to 600 kN, adopting a rate

equal to 0.2 mm/min in accordance with ISO 13934-1:2013 [41].

The testing apparatus is reported in Figure 2.3. Prior to carrying out the tensile tests on fibre coupons, the resolution of the test machine was evaluated by means of an external load cell with capacity of 10 kN. The check provided an uncertainty of about the 1% in the estimation of the load values.

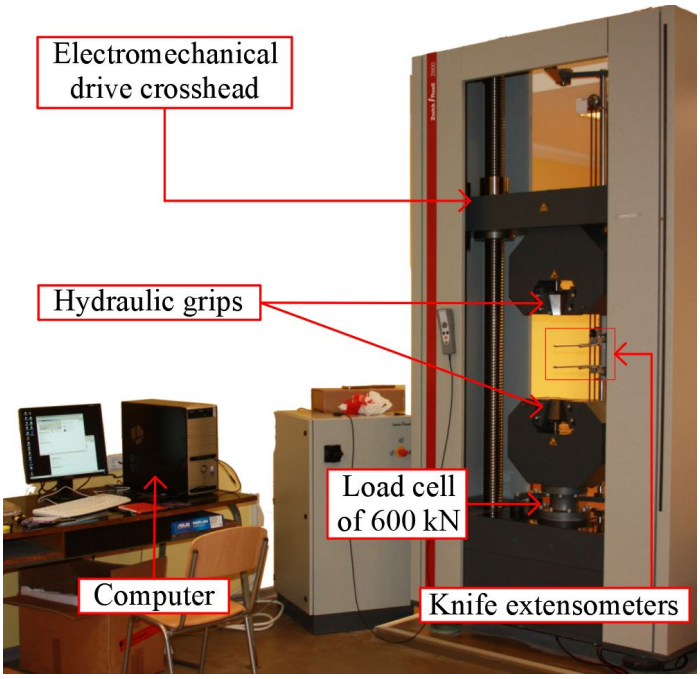

Figure 2.3: Testing apparatus adopted for tensile tests on fibre coupons.

Samples were clamped over a tab length equal to 50 mm, leaving out of the machine grips the remaining 25 mm, in order to minimize the stress concentration.

Testing machine provided the force-elongation relationship. Moreover, additional knife extensometers were settled in the middle part of the free length of samples for a gauge length equal to 80 mm, as shown in Figures 2.4(a) and 2.4(b), in order to achieve a more reliable evaluation of the strain measurements.

The knife extensometers are sensor arms directly in contact with the surface of the specimen, that allow to measure the strains through the evaluation of the change in travel distance of the sensor arms offering a resolution of 1/1000 mm.

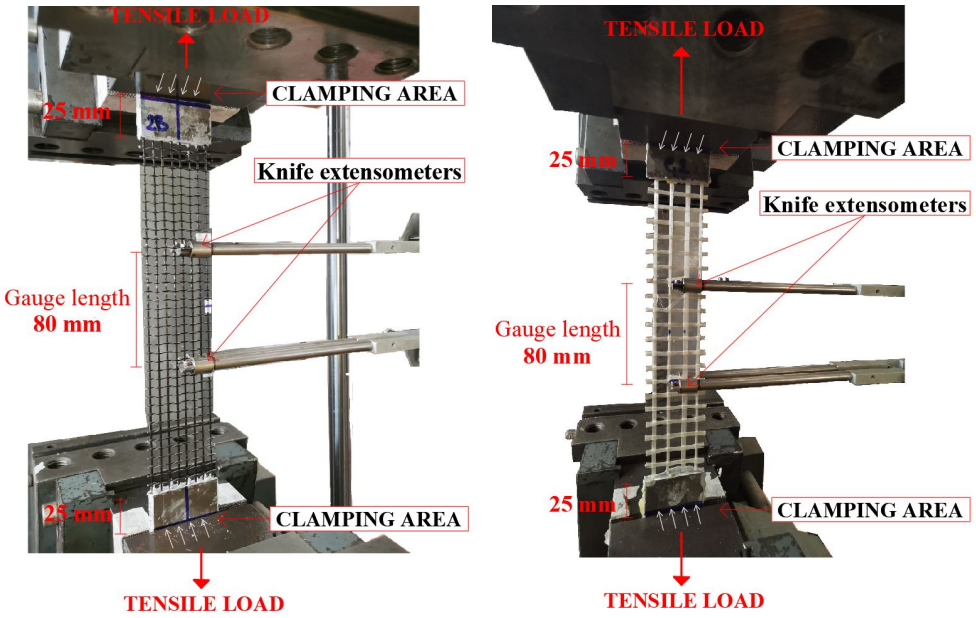

(a) basalt **(b)** glass

Figure 2.4: Tensile test set-up for fibre grid.

2.1.2 Mortar

Two bi-component premixed mortars were used as matrix for BFRCM and GFRCM systems.

The first one is an high-strength cement-based mortar (C) with short glass fibres, pozzolanic aggregates, admixtures and synthetic polymers in water dispersion according to a ready-mixed formula. The two components are mixed (i.e. the powder component and the liquid component) assuming a plastic-thixotropic consistency which allow to be applied by trowel or spray in layers up to 25 mm of thickness.

The second one is a pre-blended, fibre-reinforced, high-ductility hydraulic lime and Eco-Pozzolan based mortar (L), composed of special additives and synthetic polymers in water dispersion. When the two components (i.e. powder component and liquid component) are mixed, they form a mix which is easy to spread on the surface at a thickness of up to a maximum of 10 mm per layer.

According to the technical data sheets, cement-based mortar had flexural strength equal to $f_{m,f}$=8 MPa, compressive strength of $f_{m,c}$=25 MPa and

Young's modulus equal to E_m=10 GPa. Lime-based mortar had compressive strength of $f_{m,c}$=15 MPa and Young's modulus equal to E_m=8 GPa.

The two mortar types were experimentally characterized by deducing the main mechanical properties from three-point bending tests, Figure 2.6, on twelve 40×40×160 mm prisms and subsequently from compressive tests, Figure 2.7, on twenty-four pieces, after 28 days of curing in controlled environmental conditions of 20 ± 2 °C, as recommended in EN 1015-11 (2001) [42].

Moreover, samples of series C are cured in water for 5 days (Figure 2.5), after two days in the formwork.

Figure 2.5: Specimens of cement-based mortar (series C) cured in water for 5 days.

Two batches (referred in the following as batch *a* and batch *b*) for each mortar type (C and L) are considered. In details, batch C_a and C_b refer to matrices used for coupons of BFRCM and GFRCM with cement-based mortar, respectively, tested in tension adopting clamping grip method.

While, batch L_a and L_b refer to matrices used for specimens of BFRCM and GFRCM with lime-based mortar, respectively, tested in tension adopting clamping grip method.

Three point bending tests are performed with a universal testing machine equipped with a load cell with capacity of 5 kN (Figure 2.6(a)). Tests were carried out in displacement control mode, assuming a rate of 0.5 mm/min and imparting a pre-load of 5 N (with a rate of 0.1 mm/min).

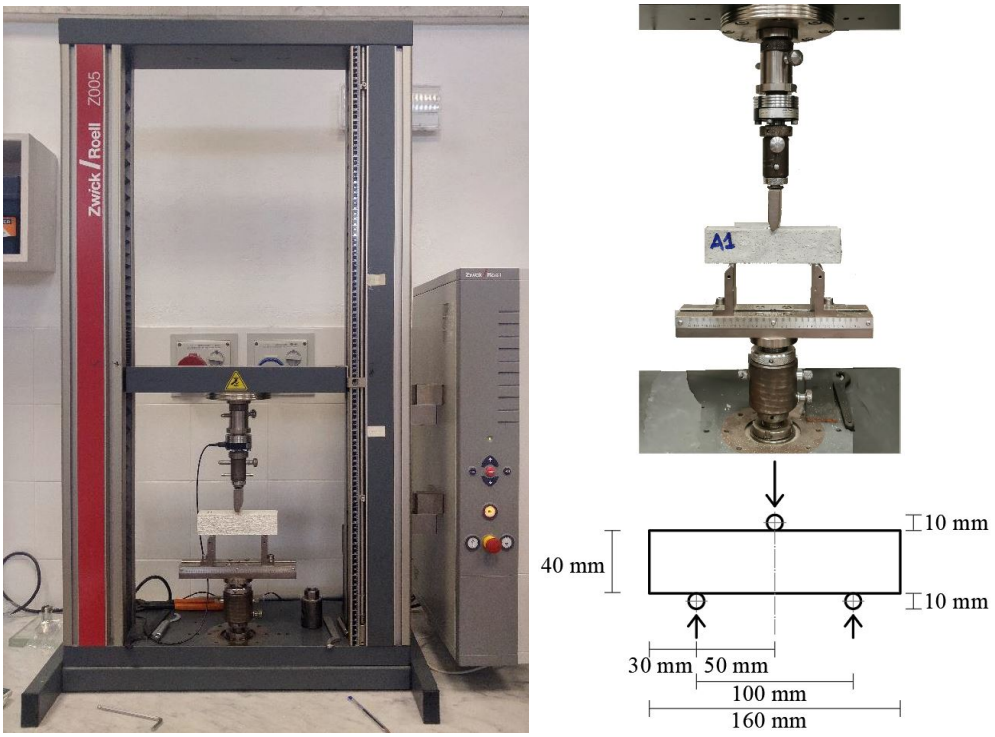

(a) testing machine **(b)** set-up configuration

Figure 2.6: Set-up for three point bending test on mortar prisms.

The displacement control mode was adopted also for compressive tests on mortar pieces, assuming a rate of 0.5 mm/min in order to evaluate also the post-peak softening branch of the experimental curves.

In particular, tests on lime-based mortar (L) are carried out with a testing machine equipped with a load cell with capacity of 50 kN (Figure 2.7(a)), while tests on cement-based mortar (C) are performed with a universal testing machine with force capacity equal to 600 kN, previously checking the resolution of the device with an external load cell with capacity of 10 kN.

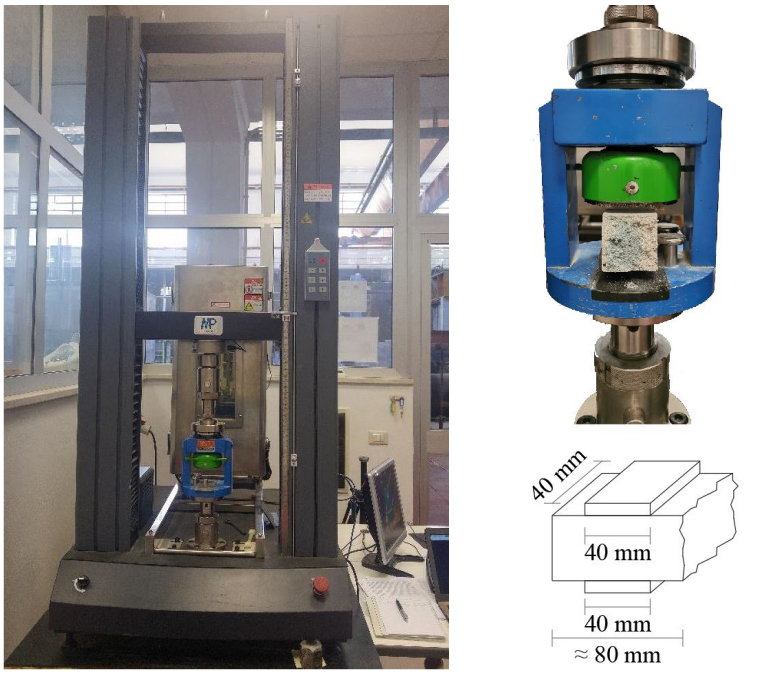

(a) testing machine **(b)** set-up configuration

Figure 2.7: Set-up for compressive test on mortar pieces.

2.1.3 Stone support

Calcarenite stone from Sabucina quarry (Sicily, Italy)[43] was employed as stone support for shear bond tests.

Calcarenite is a calcareous clastic sedimentary rock, formed by compaction and cementation of carbonate clasts of fine sand. It also contains a calcareous cementing material that binds the sand grains together and may contain a matrix of silt or clay size particles that occupy the spaces between the sand grains. Moreover, calcarenite contains shell fossils, varying in colour from reddish yellow to light yellow, and gives the material the characteristic appearance. It is a construction material widespread for historical buildings in the Mediterranean area, in Sicily.

Calcarenite stone, outcropping in the south-western area of Sicily, is characterized by high variability in their deformability, strength and permeability characteristics, as function of the zone. In particular, the value of the uniaxial

compressive strength ranges from 2.5 to 4.5 MPa for the Marsala calcarenite, and from 8 to 15 MPa for Palermo calcarenite [44].

In this experimental campaign, calcarenite from Sabucina are caracherized by the following mechanical properties provided by technical data sheet: unit weight of 18 kN/m^3, compressive strength equal to $f_{s,c}$=11 MPa and elastic modulus equal to E_s=10935 MPa.

Compressive strength and elastic modulus were verified with experimental tests previously carried out by the Research Unit of Palermo.

In particular, monotonic (UNI EN 1926 [45]) and cyclic compressive tests (UNI EN 14580 [20]) were performed on stone cubes and cylinders, respectively.

Experimental study of Minafò and La Mendola [33] provide a cubic compressive strength equal to 14.7 MPa and a cylindric compressive strength equal to 12.9 MPa and corresponding strain equal to 0.0039.

Moreover, cyclic tests provide an average elastic modulus in compression of 13249 MPa.

2.2 Tensile tests on BFRCM and GFRCM composites

The experimental campaign provides the tensile characterization of BFRCM and GFRCM composites, through two possible test set-up configurations. In particular, two gripping methods are considered: clamping and clevis grip method.

The experimental program involved tensile tests on eight groups of specimens. A total of nine samples were made up for each group, by varying the fibre reinforcement, the mortar type, the width and length of the coupons. Coupons of FRCM were named with the following notations XX_YY_n, where:

- XX indicates the fibre-mortar combination: BC stands for BFRCM with Cement-based mortar (Planitop HDM MAXI) [46], BL stands for BFRCM with hydraulic Lime-based mortar (Planitop HDM RESTAURO) [47], GC stands for GFRCM with Cement-based mortar (Planitop HDM MAXI) [46], GL stands for GFRCM with hydraulic Lime-based mortar (Planitop HDM RESTAURO) [47];

- YY indicates the gripping method for tensile test: TF and TH stands for tensile test performed with clamping method (F = Fixed grip) and clevis method (H = Hinge grip);

- n indicates the specimen number.

The FRCM systems are outlined in Table 2.3.

Table 2.3: FRCM tensile specimens.

FRCM system ID	**Number of coupons**	**Fibre type**	**Mortar type**	**Width** [mm]	**Length** [mm]
BC_TF_n	9	Basalt	Cement-based	50	400
BC_TH_n	9	Basalt	Cement-based	60	500
BL_TF_n	9	Basalt	Lime-based	50	400
BL_TH_n	9	Basalt	Lime-based	60	500
GC_TF_n	9	Glass	Cement-based	50	400
GC_TH_n	9	Glass	Cement-based	60	500
GL_TF_n	9	Glass	Lime-based	50	400
GL_TH_n	9	Glass	Lime-based	60	500

2.2.1 Specimen geometry and preparation

The experimental program for the tensile characterization of BFRCM and GFRCM systems consists of two test groups: 36 coupons tested adopting clamping grip method (9 samples for each group: BC_TF_n, BL_TF_n, GC_TF_n and GL_TF_n) and 36 coupons tested with clevis grip method (9 samples for each group: BC_TH_n, BL_TH_n, GC_TH_n and GL_TH_n groups).

Specimens consist of a single layer of basalt or glass fibre grid embedded between two layers of mortar (cement and lime-based) with equal thickness of t_m=5 mm.

Coupons were made one by one through the use of a steel formwork equipped with proper metal separator strips, as shown in Figure 2.8. In this way, any possible damage due to the cutting operations is avoided. Before casting, the surfaces were coated with a proper anti-adhesive oil, as shown in Figure 2.8, to ensure no damage when coupons are removed from the formwork.

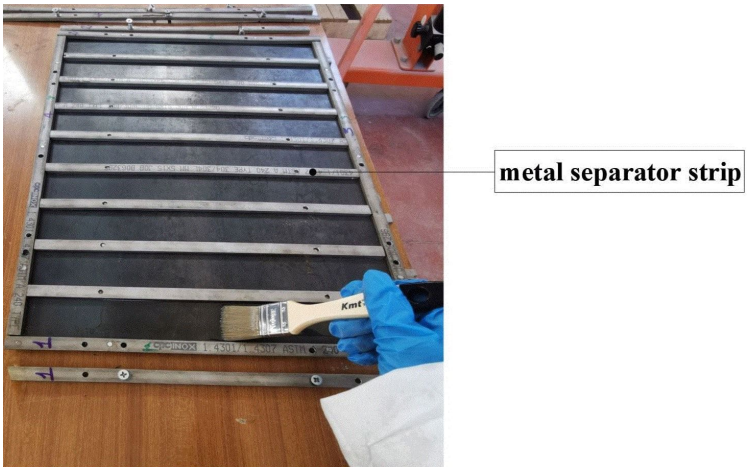

Figure 2.8: Formwork preparation for FRCM coupons.

The procedure for the fabrication of BFRCM coupons consists in three phases: a first layer of mortar is cast (Figure 2.9(a)), then basalt fibre strips are carefully settled on the mortar, ensuring fibres' alignment and planarity and finally the second layer of mortar is applied, as shown in Figure 2.9(b).

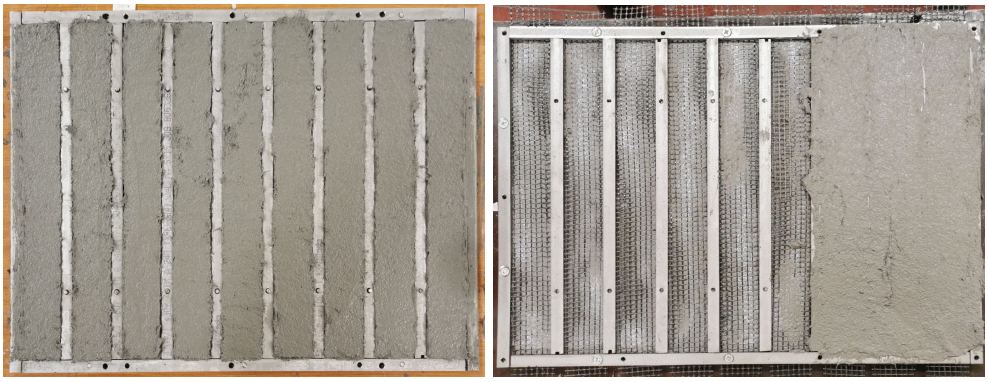

(a) first layer of mortar

(b) basalt fibre positioning and second layer of mortar

Figure 2.9: Procedures for the fabrication of BFRCM coupons.

In the case of GFRCM coupons the procedure of fabrication consists in four phases: the first layer of mortar is cast (Figure 2.10(a)), glass fibre strip

is pre-impregned with an adhesion promoter (Figure 2.10(b)), then it is settled on mortar, ensuring fibres' alignment and planarity (Figure 2.10(c)) and finally covered with a second layer of mortar (Figure 2.10(d)).

(a) first layer of mortar

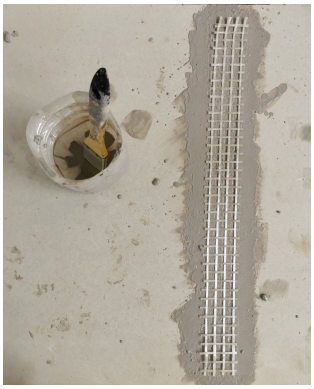

(b) adhesion promoter pre-impregnation

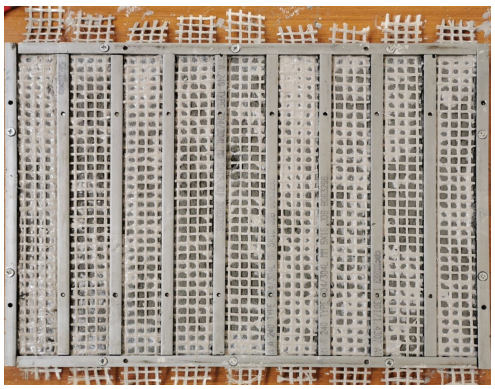

(c) glass fibre positioning

(d) second layer of mortar

Figure 2.10: Procedures for the fabrication of GFRCM coupons.

Test specimens were cured according to recommandations provided by American guidelines AC 434 [12].

The surface of samples in the formwork was covered to avoid the rapid evaporation of the water from the upper layer of mortar in contact with the air (Figures 2.11(a) and 2.11(c)). Then, samples remained in the formwork under controlled environmental conditions.

After 4 days, specimens were removed from the formwork and they have concluded the curing period in controlled standard laboratory atmospheric conditions for the remaining 24 days, with the exception of BFRCM and GFRCM coupons with cement-based mortar that before were put in water for 7 days, (Figures 2.11(b) and 2.11(d)).

(a) BFRCM coupons covering for 4 days

(b) curing in water for BFRCM with cement based mortar

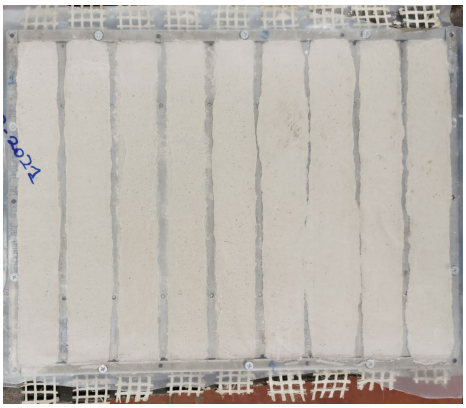

(c) GFRCM coupons covering for 4 days

(d) curing in water for GFRCM with cement based mortar

Figure 2.11: Curing of FRCM coupons.

The dimensions of the specimens tested adopting clamping grip method (BC_TF_n, BL_TF_n, GC_TF_n and GC_TF_n groups) were selected on the basis of indications contained in Italian guidelines [8]. These samples have the dimensions of 10×50×400 mm (see Figure 2.12).

Moreover, aluminium tabs with thickness of 2 mm and length of 100 mm were glued at the extremities of samples, by using a thin layer of epoxy adhesive (MapeWrap 31 [48]) ensuring the adhesion of the tabs to the FRCM strip from one hand and a reinforcing layer in the clamping area, in order to avoid any premature failure.

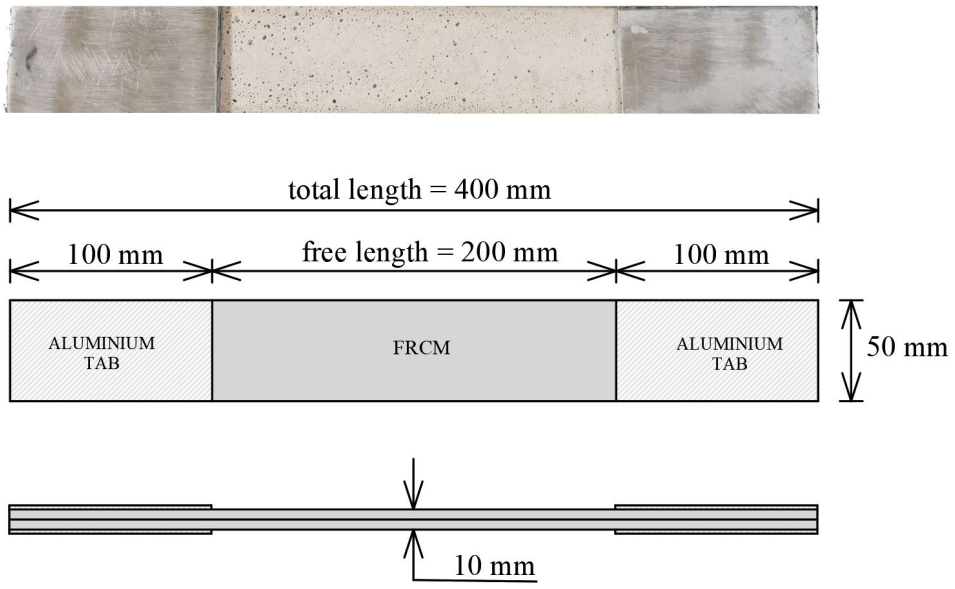

Figure 2.12: Geometry of FRCM sample equipped with aluminium tabs, for tensile tests with clamping grip method.

Samples of BC_TH_n, BL_TH_n, GC_TH_n and GL_TH_n groups were tested adopting clevis grip method, they have the dimensions of 10×60×500 mm, according to recommendations of RILEM TC 232 TDT [4]. In this case, the extremities of samples were clamped between two sufficiently stiff steel plates by bolts, for a length of 125 mm, as shown in Figure 2.13, allowing at least a rotational capacity in the plane of the specimen.

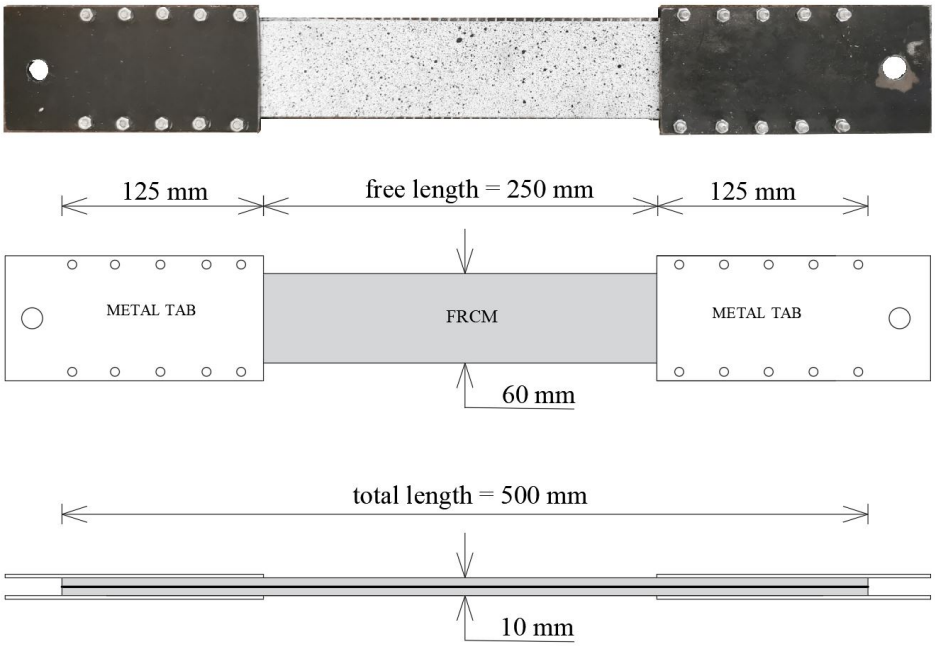

Figure 2.13: Geometry of FRCM sample equipped with steel plates by bolts, for tensile tests with clevis grip method.

2.2.2 Tensile test set-up: clamping and clevis grip method

Direct tensile tests on BFRCM and GFRCM composites were performed by a universal testing machine with force capacity equal to 600 kN. Tests were carried out in controlled displacement mode adopting a rate equal to 0.2 mm/min up to failure.

The testing machine provided the response in terms of load-global displacement curve.

In the case of clamping grip method, the specimen was clamped by hydraulic grips which transferred the tensile load to the FRCM strip, preventing any sliding and rotation during the test, Figure 2.14.

Moreover, aluminium tabs (2 mm of thickness and bond length equal to 100 mm) were glued to the surface of the specimen to better distribute the clamping pressure and to minimize the damage associated with possible local crushing of the mortar layer.

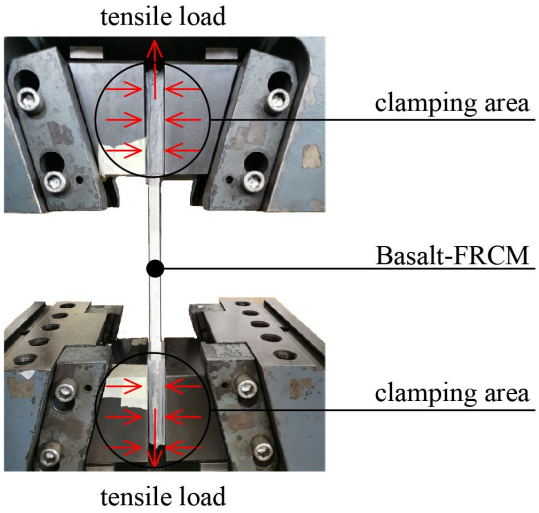

Figure 2.14: Set-up for tensile tests with clamping grip method.

The tensile load was transferred to specimens by friction when clevis grip method was adopted (Figure 2.15).

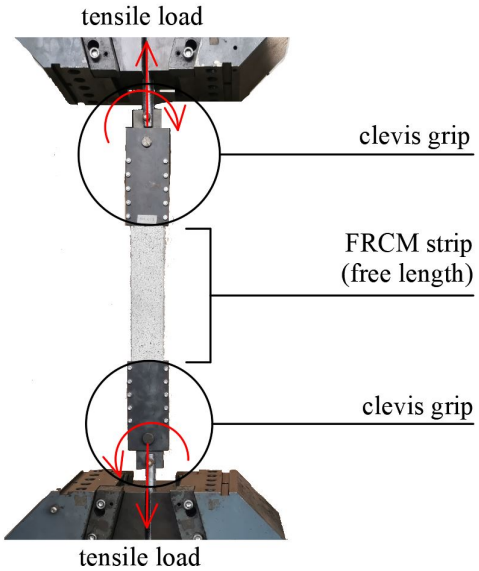

Figure 2.15: Set-up for tensile tests with clevis grip method.

Moreover, for specimens tested in tension adopting clevis grip methods, the Digital Image Correlation (DIC) technique was adopted in order to provide a contactless measurement of the strain value distribution on the mortar surface.

For the scope, one front side of the specimens was painted creating a high-contrast texture by using a white paint (Figure 2.16(a)) and a black speckle pattern (Figure 2.16(b)), as discussed in the following section.

(a) white paint

(b) black speckle pattern

Figure 2.16: High-contrast texture for FRCM coupons.

2.3 Double shear-bond tests

Aiming to evaluate the bond performances of FRCM strengthening the calcarenite masonry elements, two set-ups for double shear bond test are proposed.

The first set-up, referred as DSB1, is based to the one proposed by Accardi et al. [49] to study the bond behaviour between FRP and calcarenite stone (Figure 2.17(a)). The sample dimensions are designed in accordance with the minimum dimensions recommended by RILEM TC 250-CSM [4]. The second set-up differs from the first one (DSB1) in terms of size, it is referred as DSB2 (Figure 2.17(b)). In this way, the mechanical response of a longer and wider FRCM strip applied on calcarenite support is investigated.

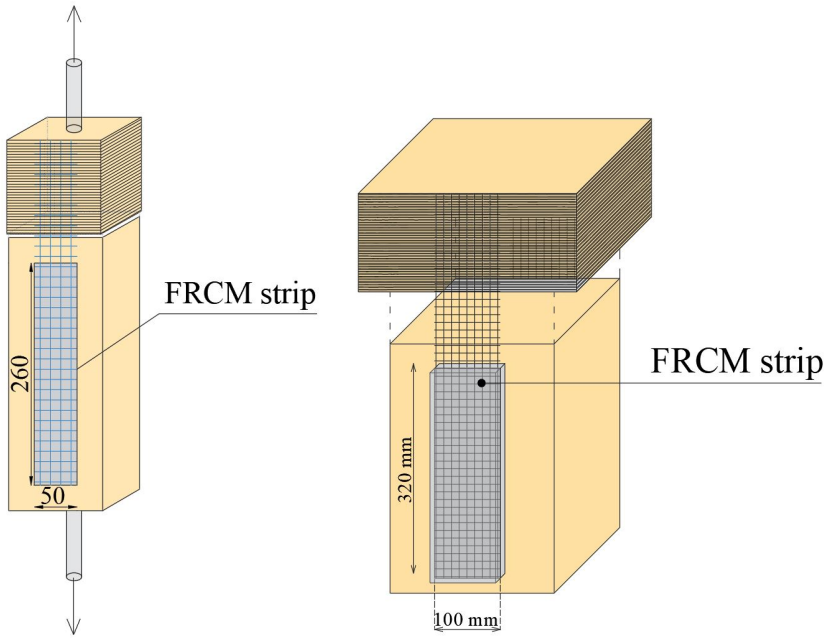

(a) DSB1 set-up **(b)** DSB2 set-up

Figure 2.17: Specimens for double shear bond tests.

In details, the experimental program involved double shear bond tests on six groups of specimens. Three specimens were produced for each group, by varying the fibre reinforcement, the mortar type, the width and bond length of the FRCM strip.

Specimens were named following the designation XX_(DSB1 or DSB2)_n. Where:

- XX indicates the fibre-mortar combination: BC stands for BFRCM with Cement-based mortar (Planitop HDM MAXI) [46], BL stands for BFRCM with hydraulic Lime-based mortar (Planitop HDM RESTAURO) [47], GC stands for GFRCM with Cement-based mortar (Planitop HDM MAXI) [46], GL stands for GFRCM with hydraulic Lime-based mortar (Planitop HDM RESTAURO) [47];
- DSB1 and DSB2 indicate the two proposed Double Shear Bond test set-up, respectively;
- n indicates the specimen number.

The specimens are outlined in Table 2.4.

Table 2.4: Specimens for double shear bond tests.

Specimen ID	Number of specimens	Fibre type	Mortar type	Bond width [mm]	Bond length [mm]
BC_DSB1_n	3	Basalt	C	50	260
BC_DSB2_n	3	Basalt	C	100	320
BL_DSB1_n	3	Basalt	L	50	260
BL_DSB2_n	3	Basalt	L	100	320
GC_DSB1_n	3	Glass	C	50	260
GL_DSB1_n	3	Glass	L	50	260

C = cement-based mortar; L = lime-based mortar

2.3.1 Geometry and preparation of specimens tested with set-up DSB1

The innovative aspects related to the first proposed set-up for Double Shear Bond (DSB1) test mainly concern the characteristics of the specimens. It is an easy and reliable set-up to study the bond behaviour of BFRCM and GFRCM composites applied on calcarenite support.

The proposed test set-up is an adaptation of another method, already validated for FRP materials, from the research unit of Palermo [49].

The experimental investigation allows to study the bond properties of different FRCM systems applied on calcarenite support observing the complex shear stress mechanisms that can develop at the fibre-to-mortar and FRCM-to-substrate interface and the failure modes as a function of the selected variables.

Specimens consist in two calcarenite blocks: the lower prismatic block with the bonded FRCM strips and the upper block wraps the un-bonded fibre strip. The lower prismatic block has dimensions of 110×110×320 mm, it is that in which the bond phenomena are evaluated, while the upper block is the anchorage of the two un-bonded fibre strips. The latter have specific dimensions of 110×120×110 mm and it is proper settled in order to compensate the thickness of 5 mm, corresponding to a layer of mortar, on each side of the sample ensuring the correct alignment of the un-bonded fibre strip.

In addiction, two steel bars were welded on steel plates and glued at the top and the bottom faces of the specimens providing a gripping system during the test. The two FRCM strips have dimensions of 10×50×260 mm and are located 30 mm away from the horizontal and vertical sides of support, as shown in Figure 2.18, in order to prevent any edge effects.

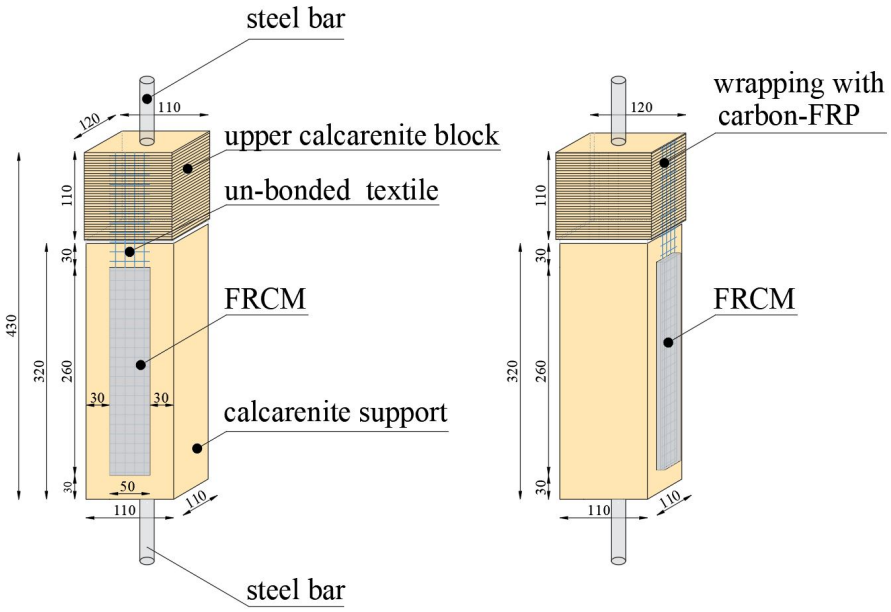

Figure 2.18: Geometry of specimen for shear bond test according to the proposed DSB1 set-up.

A formwork consisting of steel plates are used for manufacturing the composite on the two sides of the calcarenite support (double shear test) simultaneously and in order to control the thickness of the FRCM layers, as shown in Figure 2.19.

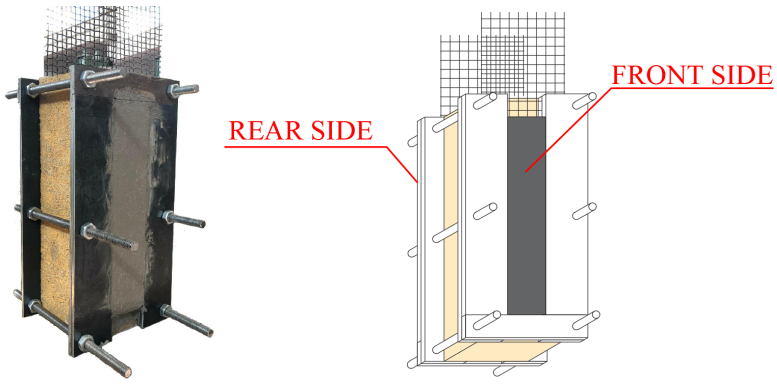

Figure 2.19: Formwork used for manufacturing the FRCM system on the two sides of the support simultaneously.

The samples were manufactured according to the following procedure, showed in Figure 2.20:

- after wetting the support in order to promote the adhesion of the FRCM system, the first layer of mortar was applied on the two sides of the calcarenite support by using a flat trowel, monitoring to have a constant thickness through the steel moulds (Figure 2.20(a));
- then, the fibre grid layers were placed (Figure 2.20(b)) taking care to ensure as well as possible the axiality of longitudinal yarns;
- finally, a top layer of mortar was applied as flat as possible on the two sides of the specimen (Figure 2.20(c)).

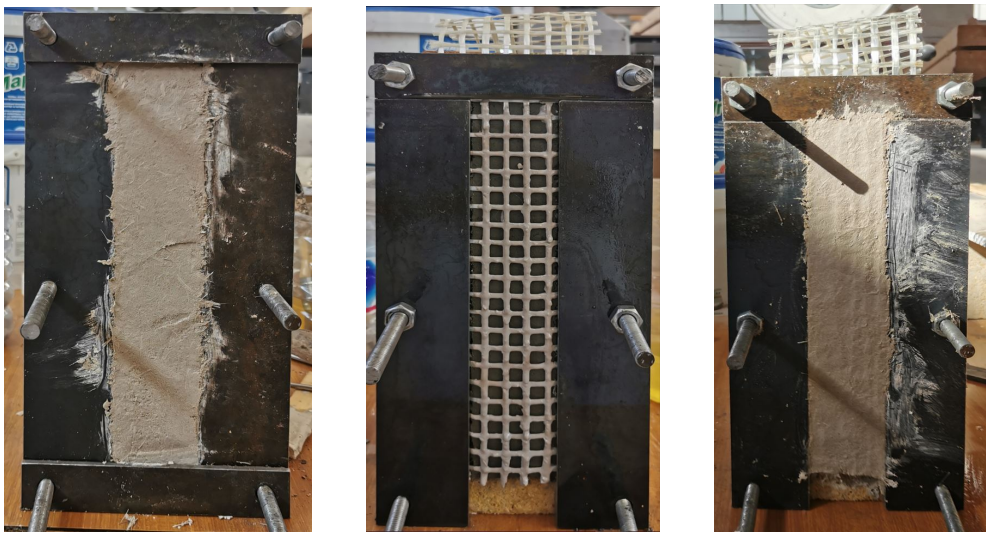

(a) first layer of mortar **(b)** textile layer **(c)** top layer of mortar

Figure 2.20: Procedure for fabrication of specimens for DSB1 set-up.

The procedure to wrap the un-bonded textile consists in four phases listed below and shown in Figure 2.21.

- Initially, the basalt grid is aligned with the upper calcarenite block avoiding any eccentricity. Subsequently, a primer layer is applied on calcarenite substrate [50] to ensure the bond of the carbon-FRP system, Figure 2.21(a);

- Then a thin layer of thixotropic epoxy resin [51] is applied on fibre strip, due to its pasty consistency it easy to apply, Figure 2.21(b);
- The un-bonded basalt textile is wrapped with a carbon strip impregnated with an epoxy resin with a medium viscosity [48], Figure 2.21(c);
- Finally, one more layer of thixotropic epoxy resin [51] is applied on carbon-FRP in order to seal the wrapping system, Figure 2.21(d).

(a) primer application **(b)** application of the matrix **(c)** wrapping with impregrened carbon strip **(d)** sealing the wrapping system

Figure 2.21: Wrapping system for specimen tested with DSB1 set-up.

Specimens were settled in a universal testing machine with capacity equal to 600 kN. Double shear bond tests were carried out in displacement control mode, adopting a rate of 0.2 mm/min up to failure. Tensile load was applied through the two steel bars settled at the centre of two steel plates, glued at the top and the bottom faces of the specimen. This system caused the direct shear on the two FRCM strips. Two digital absolute displacement indicators

were arranged on the two faces in order to measure the local fibre-to-support slip close to the loading ends, as shown in Figure 2.22.

Moreover, the DIC technique is performed in order to obtain more information about the local effects that can develop during the test. For this reason, the external mortar layer was painted, creating a high-contrast texture by using a white paint (Figure 2.23(a)) and a black speckle pattern (Figure 2.23(b)), as discussed in the following section.

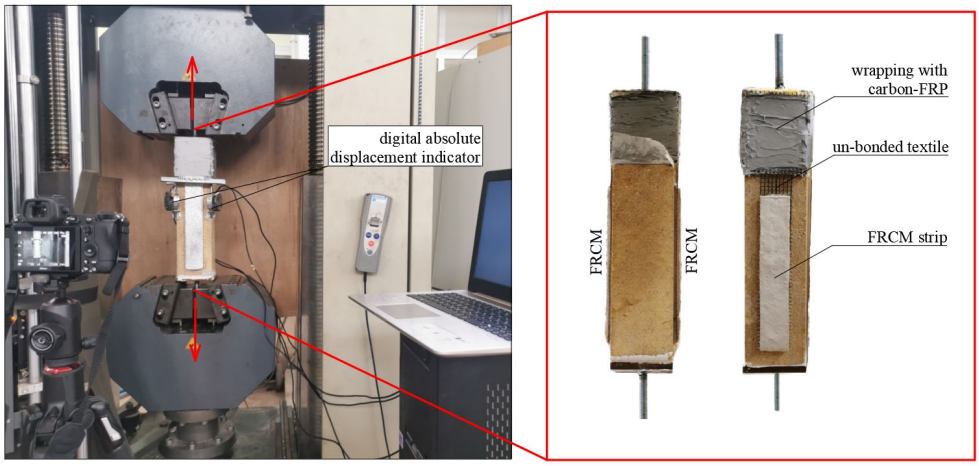

Figure 2.22: Double shear bond test set-up DSB1 for FRCM-to-calcarenite support.

(a) white paint **(b)** black speackle pattern

Figure 2.23: High-contrast texture for specimens tested with DSB1 set-up.

2.3.2 Geometry and preparation of specimens tested with set-up DSB2

It is reminded that several parameters can influence the shear bond behaviour of FRCM composites applied on masonry support. In the framework of the current experimental campaign, the role of the bond length and bond width is investigated for BFRCM composites with cement and lime-based mortar applied on calcarenite support. A larger area of the FRCM strip implies a larger size of the specimens, therefore the proposed DSB1 set-up is unsuitable because it was designed for smaller and handy samples.

In this section the DSB2 set-up is presented. It is a revisitation of the proposed DSB1 set-up on the basis of a larger size of the specimens. Specimens consist of two calcarenite elements: a lower block with the bonded BFRCM system and an upper block constraining the two un-bonded basalt fibre strips with a carbon-FRP wrapping system, as shown in Figure 2.24.

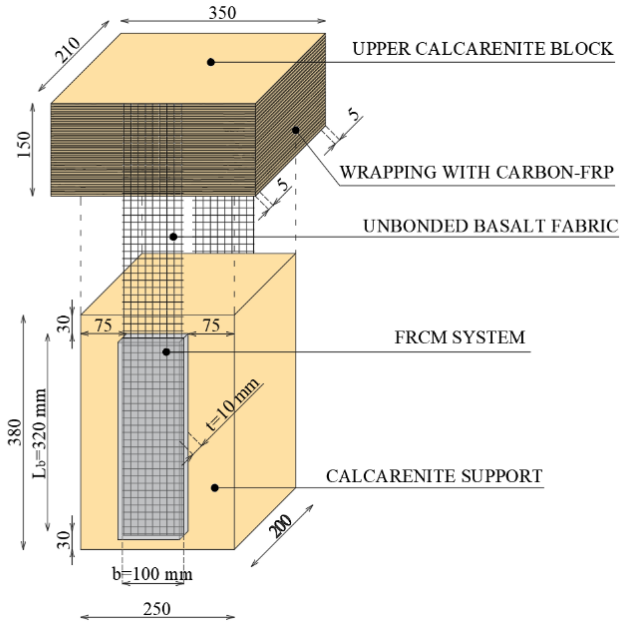

Figure 2.24: Geometry of specimen for shear bond test according to the proposed DSB2 set-up.

The lower prismatic block have dimensions of 200×250×380 mm, it is that in which the bond phenomena of the FRCM strengthening systems are evaluated,

while the upper block, with dimensions of 210×350×150 mm, is the anchorage of the two un-bonded fibre strips and transferred two balanced tensile forces to them during the test. The upper prism width is 5+5mm larger than the lower prism to account for the thickness of the mortar laid up on the lower prism and ensure the alignment and planarity of the un-bonded fibre grid, see Figure 2.24. The BFRCM strips bonded to the support have dimensions of 10×100×320 mm; they are located at 30 mm and 75 mm away from the horizontal and vertical sides of support, respectively, as shown in Figure 2.24, in order to prevent any effects of edges. The sample dimensions are designed in accordance with the existing regulations (RILEM TC 250-CSM [7] and AC 434 2013 [12]).

The manufacturing steps and the procedure to wrap the un-bonded textile strips are the same to that listed in the previous section 2.3.1 for samples tested with DSB1 set-up, as shown in Figures 2.25 and 2.26, respectively.

(a) impregnation of the support with water

(b) first layer of mortar

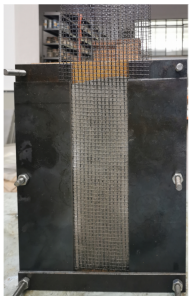

(c) textile layer

(d) top layer of mortar

Figure 2.25: Procedure for fabrication of specimens for double shear bond tests according to the proposed DSB2 set-up.

(a) primer application

(b) application of a layer of epoxy matrix

(c) wrapping with impregrened carbon strip

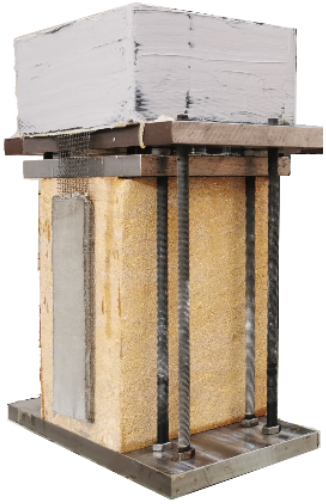

(d) sealing the wrapping system with a second layer of epoxy resin

Figure 2.26: Wrapping system.

The two blocks (upper and lower) of which the sample is composed, are constrained to a universal testing machine through two rigid steel frame, as

shown in Figure 2.27. Double shear bond tests were carried out adopting the displacement control mode with a rate of 0.2 mm/min up to failure. The load cell of testing machine recorded the total tensile load transferred to the two fibre strips. The system caused the direct shear on the two BFRCM strips. In addiction, two digital absolute displacement indicators were arranged on the two faces measuring the local fibre-to-support slip close the loading ends, as shown in Figure 2.27. Moreover, data from digital absolute displacement provided information about any phenomena related to possible eccentric loading.

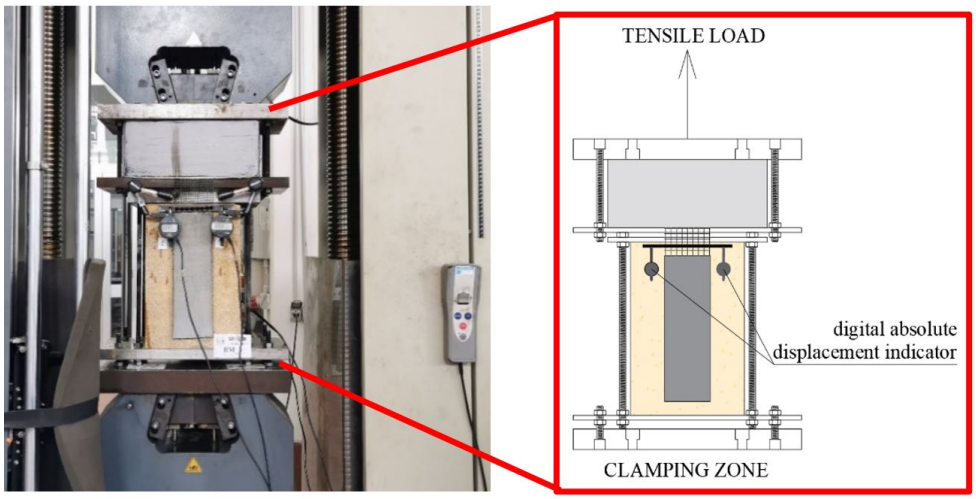

Figure 2.27: Double shear bond test set-up DSB2 for BFRCM-to-calcarenite support.

2.4 Measuring method with Digital Image Correlation (DIC)

The Digital Image Correlation (DIC) is an effective contacless technique widely used for 2D (two-dimensional) and 3D (three-dimensional) measurements of strain and full-field displacement in solid elements. In particular, it is a useful device for the study of crack propagation in full surface of any type of object.

The two-dimensional DIC technique developed by Sutton et al. [52] was employed in the current experimental investigation in order to have several advantages over conventional methods, providing more accurate measurements during the full test, as confirmed by several experimental studies available in the literature [16], [25], [53], [54].

2.4.1 Basic principles on the use of the DIC technique

Generally, the 2D DIC technique involves the typical set-up, as shown in Figure 2.28.

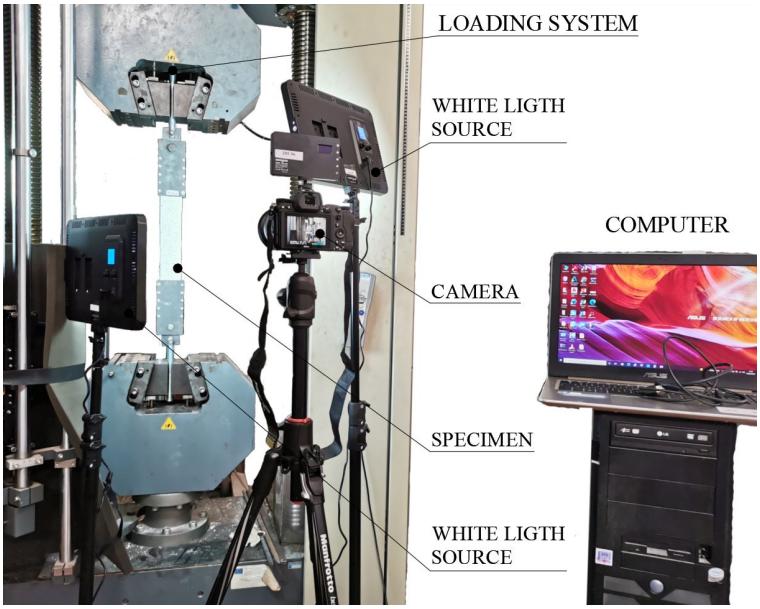

(a) real set-up

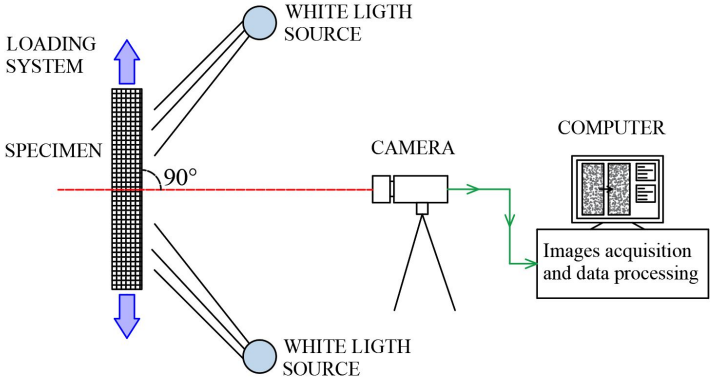

(b) schematized set-up

Figure 2.28: The 2D Digital Image Correlation test set-up.

In details, the DIC method comprises three main phases as discussed in [55]:

- preparation of the specimen surface,
- image acquisition during the test,
- post-processing of the acquired digital images to obtain the full-field of displacements and deformations.

The surface of the specimen is painted with a black and white speckle pattern, guaranteeing a random grey intensity distribution. This procedure is a basic requirement for the digitization of the images.

Then, the specimen is settled in a planar position respect to the digital camera, as shown in Figure 2.28(b). For an accurate displacement estimation, it is necessary to avoid any out-of-plane motion during the loading phases.

A digital camera with high-resolution is employed as digital image acquisition device. Moreover, in order to achieve a satisfying result, at least two white light sources are used to properly illuminate the sample during the test.

In conclusion, the acquired digital images are stored and then post-processed allowing the analysis of the full displacement and strain fields of the surface of the specimen.

The basic concept of the DIC is to compare two images of a component at different step of deformation. Displacement and strain fields are determined by correlating the position of a group of pixels (called subsets) within a selected "Region Of Interest" (ROI), in the reference (initial undeformed image) and current (subsequent deformed images) configurations, as shown in Figure 2.29. The subsets are small subsections of the reference image containing a set of coordinated points (red crosses in Figure 2.29). In this way, a subset provides a unique array of grey level pixel value that makes it identifiable compared to a single point with a single gray level pixel value. The choice of the subset size has a fundamental importance because significantly affect the DIC accuracy. In general, the subset size should be the smallest subset possible as a function of the granularity of the speckle pattern and suitable to describe large heterogeneous deformations.

The reference points referred to the undeformed image (ref) are mathematically correlated to the corresponding points in the deformed image (cur), see Figure 2.29. For this reason, in order to track the subset, the DIC technique demands a predefined criterion and a proper optimization algorithm. Available

studies from literature provides various criteria, including Cross Correlation (CC) criterion, Sum of Absolute Difference (SAD), Sum of Squared Difference (SSD), and Parametric Sum of Squared Difference (PSSD) [56].

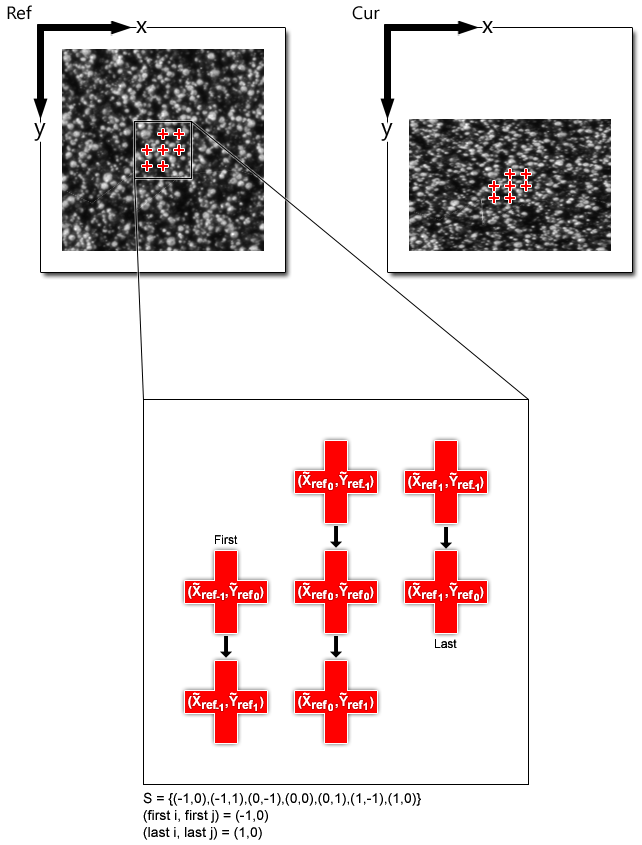

Figure 2.29: The subset's coordinated points in the reference (ref) and current (cur) image.

In detail, the displacement of a point of interest $P(x_0, y_0)$, centered respect to a square reference subset of N×N pixels, is evaluated by tracking its corresponding location in the deformed image, as shown in Figure 2.30. A proper criterion allows to evaluate the difference between the selected reference subset and the target subset. By sliding the reference subset in the searching area of the deformed image and computing the correlation coefficient at each location,

a correlation coefficient map is obtained as schematized in Figure 2.30. Subsequently, a certain optimization algorithm allows to complete the procedure by finding the peak of the correlation coefficient distribution.

In conclusion, the position of the reference subset center respect to the target subset center provides the displacement vector at the point P. Then, the same procedure is extended to the other pixels in order to obtain the full-field displacement.

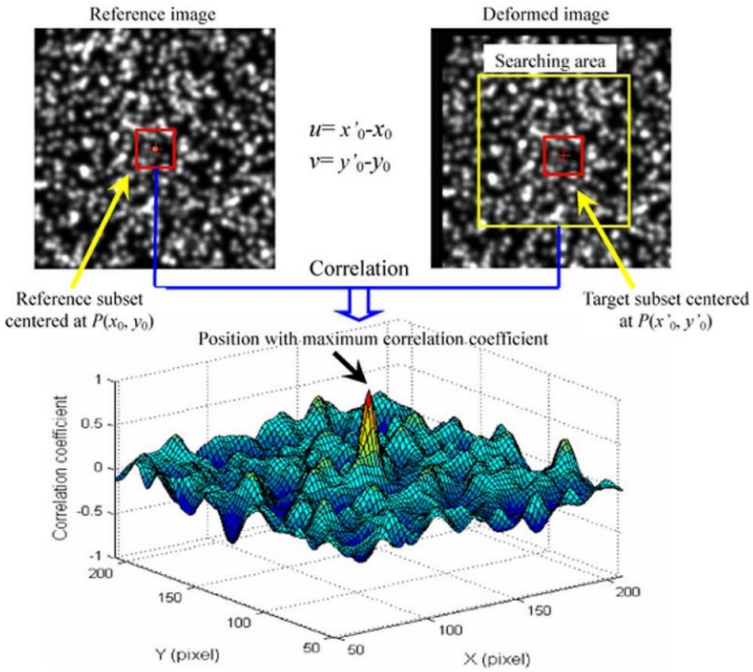

Figure 2.30: Tracking of the reference subset in the deformed image. The center position of the target subset is obtained by searching the peak of the correlation coefficient distribution (Pan et al. 2010 [9]).

2.4.2 Ncorr software for DIC analysis

As discussed in the previous section, the DIC technique is based on the use of image registration algorithms to track the relative displacements of material points between a reference image and a current image referred to a deformed configuration of an element.

In this study, the Ncorr software has been employed for DIC analysis. Ncorr

is an open source 2D digital image correlation MATLAB program [57] that combines numerous algorithms proposed in the literature [58], [59], [60], [61] and [62].

The work flow of the Ncorr program is set as follows:

- setting of the reference image,
- setting of current image(s),
- setting the Region Of Interest (ROI),
- setting DIC parameters,
- performing DIC analysis.

The Ncorr package is implemented in the MATLAB [63] environment. The compute intensive algorithms are written in programming language C ++ and optimized through the MEX interface. In subset-based DIC algorithms, the transformation of initial reference subset points to the current configuration is constrained to a linear, first order transformation.

The DIC algorithms find the extreme of a correlation function. In Ncorr, two different correlation criteria are used to find the initial guess (normalized cross correlation) and its subsequent refinement (nonlinear optimizer). The procedure provides to calculate the displacement data of a single material point located at the center of a reference subset.

Subsequently, in order to obtain the displacement values for all subsets, Ncorr uses the Reliability Guided (RGDIC) method [59].

It is worth to point out that the results obtained from the DIC analysis are in terms of pixel displacements which must be converted into displacement and strain values by using a DIC post-processing tool Ncorr_post software [64] that is an extension of 2D DIC MATLAB software Ncorr. It was developed at Czech Technical University in Prague and offers rather advanced functionalities such as the visualization of cracking development also for low strain levels and the possibility to place virtual extensometers over the whole detected surface of the specimen, in order to obtain loading stage-displacement diagrams.

Chapter 3

Experimental results

This chapter presents the results of the performed experimental campaign. Firstly, the experimental results concerning the mechanical characterization of all materials are reported.

Afterward, a comparative performance assessment of the tensile behaviour of different FRCM systems is presented, evaluating the influence of some specific parameters such as the fibre nature, mortar grade and test set-up.

Finally, particular attention is paid to the outcomes from shear bond tests of different FRCM systems applied on calcarenite masonry support, highlighting the efficacy of the two proposed test set-ups.

3.1 Characterization test results of constituent materials

In this section, all the results concerning the mechanical characterization of the constituent materials (fibre grid and mortar) are presented.

3.1.1 Tensile characterization of fibre grids

The mechanical properties of basalt and glass textile adopted for the FRCM systems were verified in laboratory by performing tensile tests on fibre mesh coupons, according to the recommendations contained in ISO 13934-1:2013 [41].

The specimens are renamed with the following nomenclature sp_(B or G)_n. Where: *sp* is for "specimen"; B and G indicate the nature of fibre, i.e. basalt of glass grid respectively; finally, *n* indicates the specimen number.

Results of tensile tests on basalt and glass fabric strips are here reported in terms of stress-global strain (solid line) and stress-local strain (dashed line)

curves, as shown in Figures 3.1(a) for basalt and 3.1(b), for glass. Moreover, the average trend between the results of each group is plotted in red.

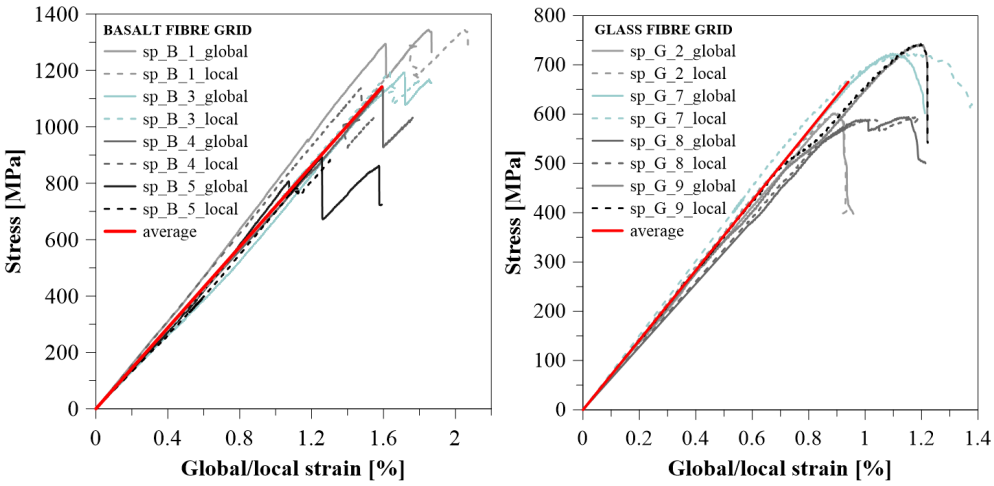

(a) Basalt **(b)** Glass

Figure 3.1: Stress-global/local strain curves of fibre textile.

The stress values are evaluated by dividing the load data acquired through the load cell by the testing machine for the cross-sectional area of the textile (A_f). This last is calculated by multiplying the strip width by the equivalent dry thickness of the fibre (t_f).

The global strains are obtained by dividing the global displacement of the machine cross-head by the total specimen length.

Differently, the local strains are calculated for the gauge length adopted through the knife extensometers placed in the middle of the coupon, i.e. 80 mm.

By comparing all the curves, it is worth to point out that the global and local strains have the same trend up to the peak stress approximately. However, in some case, problems of sliding and rotation of the aluminium tabs in the gripping area occurred during the test and different trends of local strains respect to the global values are observed. For this reason, these results are excluded and not reported in this thesis.

The tensile stress-strain curves of basalt textile (Figure 3.1(a)) show a linear trend and different load drops due to the progressive brittle failure of some roving in the strip width.

Experimental curves for glass textile (Figure 3.1(b)) present an initial ascending branch with a quasi-linear trend up to the peak. This last is followed by a limited softening branch, which highlights the brittle behaviour of the glass fibre mesh.

Generally, the failure mode observed for basalt fibre strips is the tensile rupture near the gripping area, as shown in Figure 3.2(a), which is probably due to an irregular stress distribution along the width consisting of eight yarns. While glass fibre strips often fail along the free length of the specimen, as shown in Figure 3.2(b).

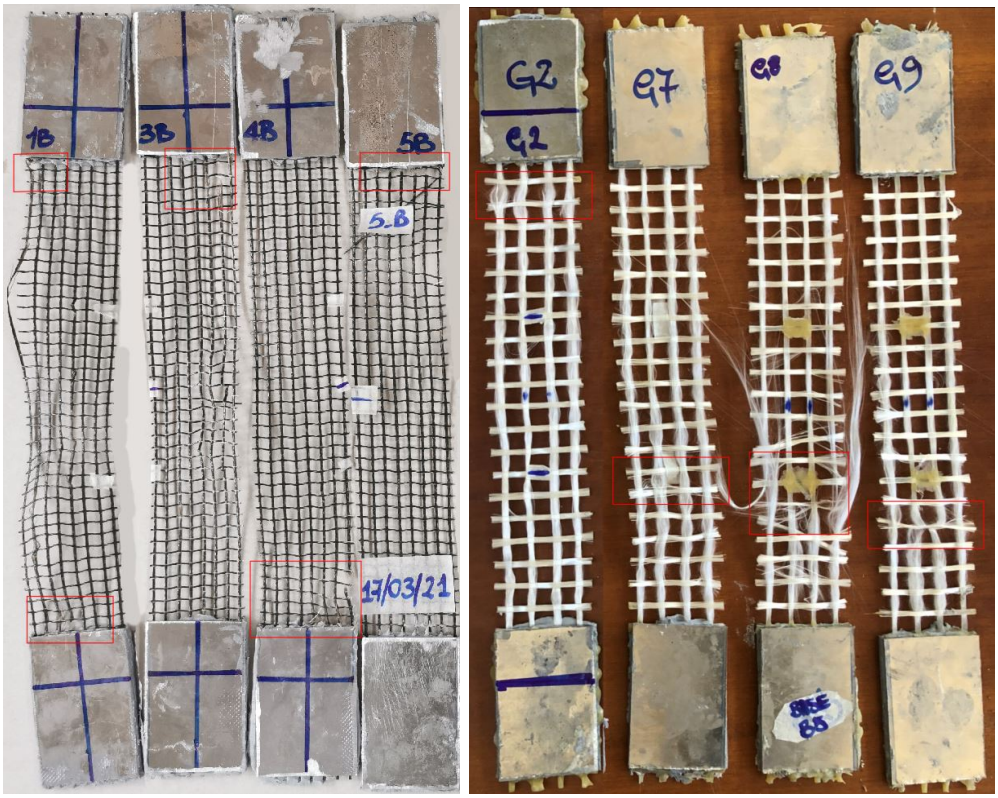

(a) Basalt **(b)** Glass

Figure 3.2: Fibre strips after failure.

The test method allows to deduce the main mechanical properties for basalt and glass fibre: average tensile strengths f_{fu} of 1142.2 MPa and 665.4 MPa,

corresponding local strains ϵ_{fu} of 1.61% and 1.09%, elastic moduli E_f of 71.8 GPa and 70.8 GPa, respectively. All the experimental results are summarized in Table 3.1 for the coupons of basalt textile and Table 3.2 for glass textile.

Table 3.1: Results of tensile tests on basalt fibre

Basalt fibre grid			
Sample ID	**Tensile strength** f_{fu} [MPa]	**Ultimate strain** ϵ_{fu} [%]	**Elastic modulus** E_f [GPa]
sp_B_1	1344.8	1.85	71.5
sp_B_3	1192.5	1.72	71.8
sp_B_4	1139.1	1.60	77.7
sp_B_5	892.6	1.26	66.2
Average	**1142.2**	**1.61**	**71.8**
COV	**(14.3** %)	**(13.6** %)	**(5.7** %)
DATA SHEET	1538.5	1.80	89

Table 3.2: Results of tensile tests on glass fibre

Glass fibre grid			
Sample ID	**Tensile strength** f_{fu} [MPa]	**Ultimate strain** ϵ_{fu} [%]	**Elastic modulus** E_f [GPa]
sp_G_1	601.6	0.96	72.1
sp_G_3	723.1	1.10	75.4
sp_G_4	594.5	1.15	65.1
sp_G_5	742.3	1.20	70.5
Average	**665.4**	**1.09**	**70.8**
COV	**(10.2** %)	**(10.9** %)	**(9.7** %)
DATA SHEET	1400.0	2.00	74

It should be noted that these results are significantly lower than the values provided by the manufacturer. The possible causes for this difference are probably related to the difficulty to guarantee a uniform load distribution among a larger number of longitudinal yarns, as also observed in several experimental studies available in the literature [65].

In detail, the average tensile strength, ultimate strain and elastic modulus of basalt fibre grid show reductions of the 25.8%, 10.6% and 19.3% with respect to the values provided by the manufacturer (i.e. tensile strength f_{fu}=60 kN/m, ultimate strain ϵ_{fu}=1.8% and elastic modulus E_f=89 GPa, Table 2.1).

The average tensile strength and ultimate strain for glass fibre grid are both about the 50% lower than the values provided by the manufacturer (i.e. tensile

strength f_{fu}=56 kN/m and ultimate strain ϵ_{fu}=2.0%, Table 2.2). While, the experimental average elastic modulus for glass fibre grid is 70.8 GPa, slightly lower (about 4.3%) than the value provided by the manufacturer (E_f=74 GPa, Table 2.2).

3.1.2 Mechanical characterization of mortar

The mechanical properties of the two mortar types adopted as matrix for the FRCM systems, one cement-based (C) and another one hydraulic lime-based (L), are experimentally verified from three-point bending tests on a total of 12 prisms and subsequent compressive tests on 24 pieces.

The values of flexural and compressive strength for cement-based mortar of batch C_a and batch C_b, are summarized in Tables 3.3, 3.4, respectively.

Experimental results provide an average flexural stength of $f_{m,f}$=6.60 MPa and $f_{m,f}$=6.20 MPa and compressive strength of $f_{m,c}$=40.80 MPa and $f_{m,c}$=36.11 MPa, for batch C_a and C_b, respectively.

The average strengths and the Coefficient Of Variation (COV) are calculated excluding the unreliable results and the highest and lowest value, according to the code prescription [42].

Table 3.3: Mechanical characteristics of cement-based mortar (C), batch C_a.

Sample ID	**Flexural strength** $f_{m,f}$ [MPa]	**Sample ID**	**Compressive strength** $f_{m,c}$ [MPa]
C_a1	6.04	C_a1A	40.30
		C_a1B	38.91
C_a2	6.56	C_a2A	41.89
		C_a2B	39.83
C_a3	7.42*	C_a3A	40.01
		C_a3B	42.17*
C_a4	6.63	C_a4A	42.09
		C_a4B	40.91
C_a5	7.18	C_a5A	41.56
		C_a5B	42.01
C_a6	4.94*	C_a6A	38.69*
		C_a6B	41.06
Average	6.60		40.80
COV	(6.1 %)		(2.4 %)

*values excluded from the calculation of the average strength

Table 3.4: Mechanical characteristics of cement-based mortar (C), batch C_b.

Sample ID	**Flexural strength** $f_{m,f}$ [MPa]	**Sample ID**	**Compressive strength** $f_{m,c}$ [MPa]
C_b1	4.91*	C_b1A	36.29
		C_b1B	40.46
C_b2	6.33	C_b2A	31.16
		C_b2B	34.18
C_b3	6.53	C_b3A	39.34
		C_b3B	34.25
C_b4	6.89*	C_b4A	41.10*
		C_b4B	39.50
C_b5	6.62	C_b5A	35.23
		C_b5B	27.56*
C_b6	5.33	C_b6A	34.62
		C_b6B	0.22*
Average	6.20		36.11
COV	(8.3 %)		(8.0 %)

*values excluded from the calculation of the average strength

Results from tree-point bending tests and subsequent compressive tests on samples of lime-based mortar are presented in Tables 3.5, 3.6, for batch L_a and batch L_b, respectively.

Table 3.5: Mechanical characteristics of lime-based mortar (L), batch L_a.

Sample ID	**Flexural strength** $f_{m,f}$ [MPa]	**Sample ID**	**Compressive strength** $f_{m,c}$ [MPa]
L_a1	8.17*	L_a1A	17.43
		L_a1B	18.09*
L_a2	5.15*	L_a2A	14.72
		L_a2B	13.48
L_a3	5.17	L_a3A	13.57
		L_a3B	13.29*
L_a4	7.13	L_a4A	17.66
		L_a4B	17.41
L_a5	6.23	L_a5A	16.79
		L_a5B	17.06
L_a6	6.54	L_a6A	-
		L_a6B	-
Average	6.27		16.01
COV	(11.3 %)		(10.5 %)

*values excluded from the calculation of the average strength

Experimental results provide an average flexural stength of $f_{m,f}$=6.27 MPa

and compressive strength of $f_{m,c}$=16.01 MPa for batch L_a.

Table 3.6: Mechanical characteristics of lime-based mortar (L), batch L_b.

Sample ID	**Flexural strength** $f_{m,f}$ [MPa]	**Sample ID**	**Compressive strength** $f_{m,c}$ [MPa]
L_b1	4.19	L_b1A	17.28
		L_b1B	18.62
L_b2	5.06*	L_b2A	18.64
		L_b2B	22.32*
L_b3	3.81	L_b3A	17.90
		L_b3B	18.88
L_b4	3.45*	L_b4A	9.55*
		L_b4B	-
L_b5	4.48	L_b5A	12.29*
		L_b5B	-
L_b6	4.62	L_b6A	10.90*
		L_b6B	-
Average	4.27		18.26
COV	(7.3 %)		(3.2 %)

*values excluded from the calculation of the average strength

Experimental results provide an average flexural strength of $f_{m,f}$=4.27 MPa and compressive strength of $f_{m,c}$=16.36 MPa, for batch L_b. In this case, some results were excluded from the calculation of the average compressive strength because the analysis of the specimens after the test showed a failure mode different from the typical "hourglass shape" generally observed for the other samples (Figure 3.3(b)). It can be mainly attributed to the presence of some intrinsic defects in the specimen tested in compression.

Differently, the prisms tested according to three-point bending setup show always the typical failure mode characterized by the propagation of the crack from the extrados (tensile region) toward the intados (compressive region) of the prism (Figure 3.3(b)).

In general, a good uniformity of the average results referred to samples of cement-based mortar, batch C_a and C_b, is observed. Differently, a scatter of about 32% is observed between the average flexural strength of lime-based mortar samples of batch L_a ($f_{m,f}$=4.27 MPa) and L_b ($f_{m,f}$=4.27 MPa). The two batches are prepared at different times, so the slight difference can be attributed to a small variability in the mixture of the two components as well as different environmental conditions.

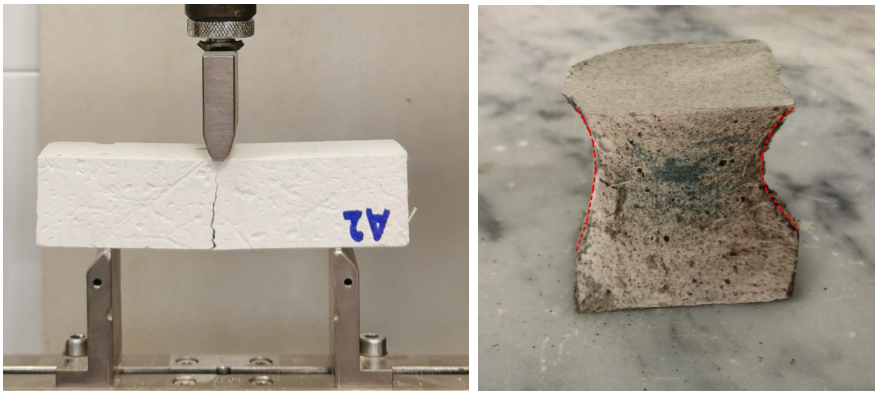

(a) failure after three point bending test **(b)** failure after compressive test

Figure 3.3: Mortar specimens after test.

3.2 Tensile test results of BFRCM and GFRCM composites

In this section, the outcomes of monotonic tensile tests on FRCM composites are presented.

The results are analyzed in terms of load-strain and stress-strain curves, exploring the role of the fibre nature, mortar grade and gripping method on the tensile behaviour of the eight series of specimens.

Finally, the results from DIC analysis for coupons tested with clevis grip method are presented and discussed.

3.2.1 Results from clamping grip method

The results of tensile tests carried out with the clamping grip method are divided in four groups, one for each FRCM system.

First, the results of the tests are analyzed in terms of load-strain curves, exploring the stages that characterize the tensile behaviour.

Then the post-treatment of the experimental data allows the definition of the stress values (σ_I, σ_{II} and σ_{III}) and corresponding strains (ε_I, ε_{II} and ε_{III}), evaluated at the end of each stage of the tensile stress-strain curves (i.e. un-cracked, cracks development and cracked stage) according to the idealized tri-linear trend suggested in the Italian Guidelines [8], see Figure 3.4.

More in detail, the stresses are calculated by dividing the load values acquired by the load cell of the testing machine by the cross-sectional area of plain

textile (A_f), as suggested by Italian [8] and American [12] guidelines. In order to ensure consistency with the procedure adopted for the textile characterization, the area of the internal reinforcement (A_f) was calculated by multiplying the FRCM width (b) by the equivalent dry thickness of the fibre (t_f).

While, the strain values are obtained by dividing the global displacement of the machine cross-head by the total specimen length.

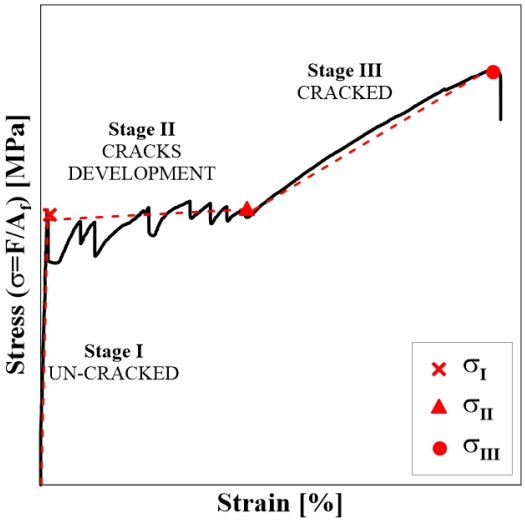

Figure 3.4: Typical tensile behaviour of FRCM composites (Italian Guidelines [8]).

Figures 3.5 show the results in terms of load-strain curves for BFRCM and GFRCM composites with cement-based mortar (Figure 3.5(a) and Figure 3.5(c)) and lime-based mortar (Figure 3.5(b) and Figure 3.5(d)).

These outcomes show that the experimental curves for specimens of BFRCM and GFRCM with cement-based mortar (group BC_TF and GC_TF) do not follow the typical tri-linear trend generally observed for FRCM composites tested in tension. In these cases, see Figure 3.5(a) and Figure 3.5(c), the curves are characterized by a first linear branch (Stage I) that strictly depends on the strength and stiffness of cement-based mortar.

A very limited second phase develops after the first peak load and a consequently less ductility. In detail, Stage II cannot be distinguished from Stage III, because the FRCM system quickly reaches the failure. It is due to the high-strength matrix from one hand and the good fibre-matrix bond capacity from the other. Moreover, in some case the GFRCM specimens show a post-peak

softening branch, which highlighted the gradual telescopic rupture of the yarns.

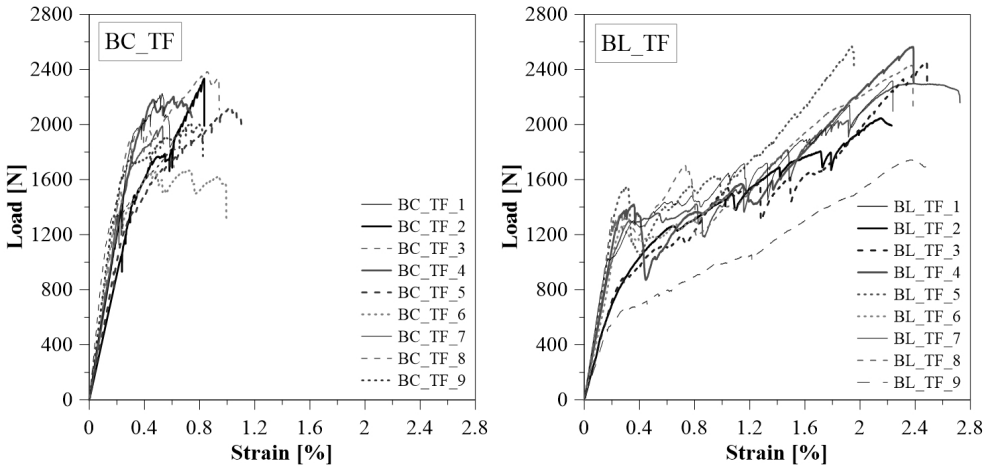

(a) BFRCM with cement-based mortar

(b) BFRCM with lime-based mortar

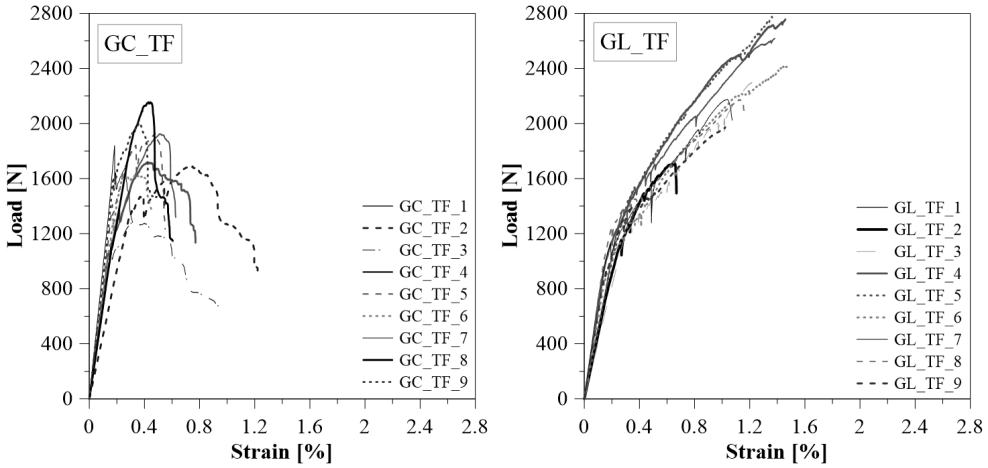

(c) GFRCM with cement-based mortar

(d) GFRCM with lime-based mortar

Figure 3.5: Load-strain curves of BFRCM composite coupons, tested with clamping grip method.

Experimentally, it is observed that when BFRCM and GFRCM with cement-based mortar reach the first cracking load, the fibre reinforcement has almost reached its maximum strength and the FRCM system fails for much lower

strain values, about the 40 % and 35 % of the ultimate elongation of the bare basalt and glass grid, respectively. It is a consequence of an under-reinforced cross-section of the FRCM composite system.

Generally, the observed failure mode for specimens of group BC_TF consists in fibre rupture in the middle length of the specimens or near the gripping area, as shown in Figure 3.6.

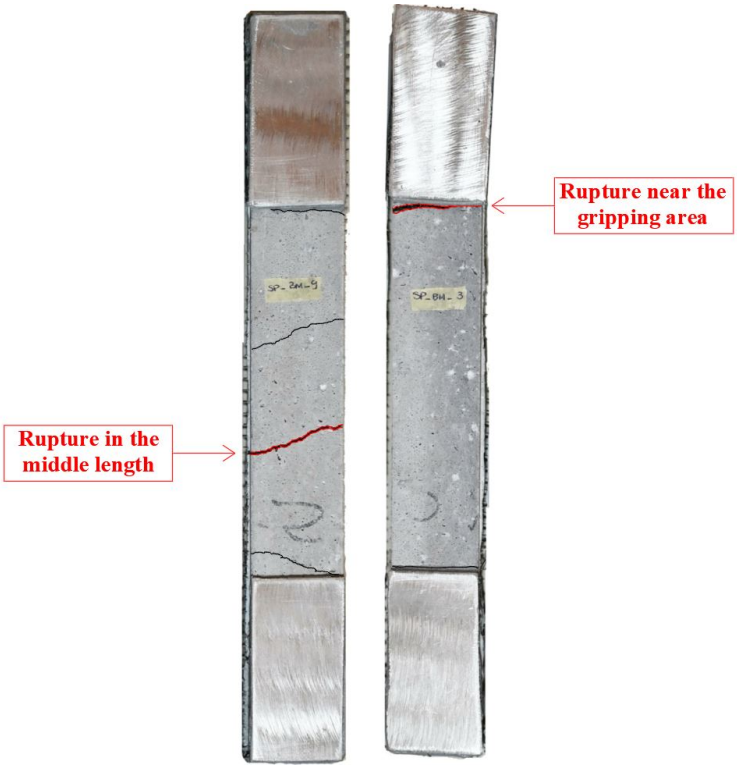

Figure 3.6: Specimens of group BC_TF after testing.

In details, the first cracks appear at the extremities of the FRCM strips, close to the gripping area; so that the tensile load is entirely applied at the fibre ends when the first cracking load is achieved. Then the load is transferred through the the coating eternal layer of fibre grid by chemical adhesion to the mortar layers. However, few cracks develop along the length of the specimen due to the under-reinforced FRCM cross-section. This last not allows the exploitation of the constitutive law of fibre-mortar interface due to the fibre rupture occurs.

Differently, the failure close close to the gripping area is generally characterized by the formation of only one crack. It is woth point out that this failure mode did not affect the performance of specimens tested in tension. Indeed, the maximum loads associated with this failure mode are similar to those reached when the main crack develops in the middle of the specimen.

For the same remarks, the main failure mode observed for specimens of group GC_TF consists in fibre rupture near the gripping area with the formation of few cracks, as shown in Figure 3.7.

Figure 3.7: Specimens of group GC_TF after testing.

The typical tri-linear behaviour is observed for the coupons of group BL_TF (Figure 3.5(b)). The Stage I of the curves is mainly governed by lime-based mortar stiffness up to reach the first cracking load.

Unlike the previous case, i.e. BC_TF (Figure 3.5(a)), the development

of Stage II and Stage III is observed. Several cracks simultaneously with the activation of the interface stress-transfer occur during the Stage II. This last is characterized by several load drops corresponding to crack opening. When the crack stabilization is achieved, the Stage III starts, and the the main contribute to load bearing is given by basalt fibre reinforcement.

Moreover, a different failure mode is observed for BFRCM systems with hydraulic lime-based mortar. In particular, the formation of several cracks in the mortar layers and the sliding of fibre within the mortar layers are observed.

Finally, the composite system fails due to tensile fibre rupture near the gripping area and in some case in the middle of the specimens, as shown in Figure 3.8.

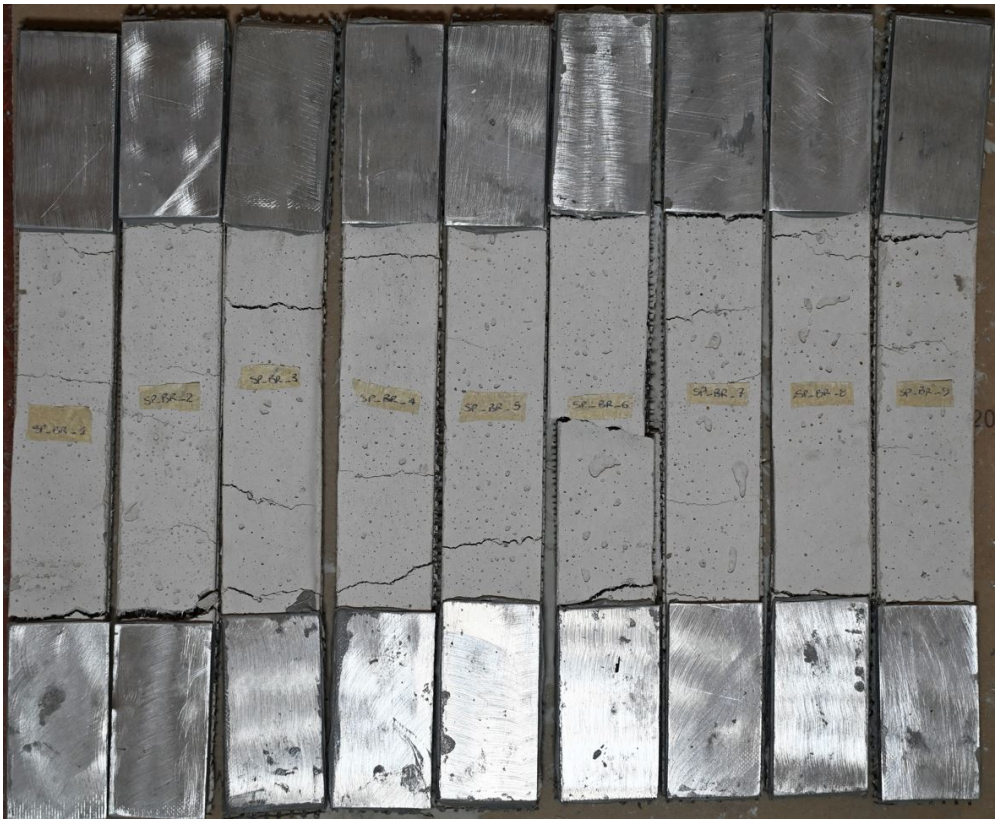

Figure 3.8: Specimens of group BL_TF after testing.

In one case (coupon BL_TF_6) the delamination at the fibre-mortar interface occurs, as shown in Figure 3.9.

Figure 3.9: Failure mode of specimens BL_TF_6.

When the hydraulic lime-based mortar is employed as matrix, the constitutive tensile behaviour of GFRCM is mainly characterized by a bi-linear trend (Figure 3.5(d)). Where, the first un-cracked stage (Stage I) is mainly governed by mortar strength and stiffness. While, Stage II cannot be distinguished from Stage III.

When the first cracking load is achieved, an almost linear branch develops, assuming the slope of the axial stiffness of bare glass fibre. The gradual development and widening of cracks is observed and during this phase the interaction between fibre and mortar is never lost.

The samples are characterized by the development of several cracks in the free length up to a maximum load value much higher than the tensile strength of the bare glass textile. This is probably due to the use of the adhesion promoter, which allows the fabric to develop a strong interaction with the matrix.

The failure observed is the tensile fibre rupture near the gripping area, as shown in the Figure 3.10.

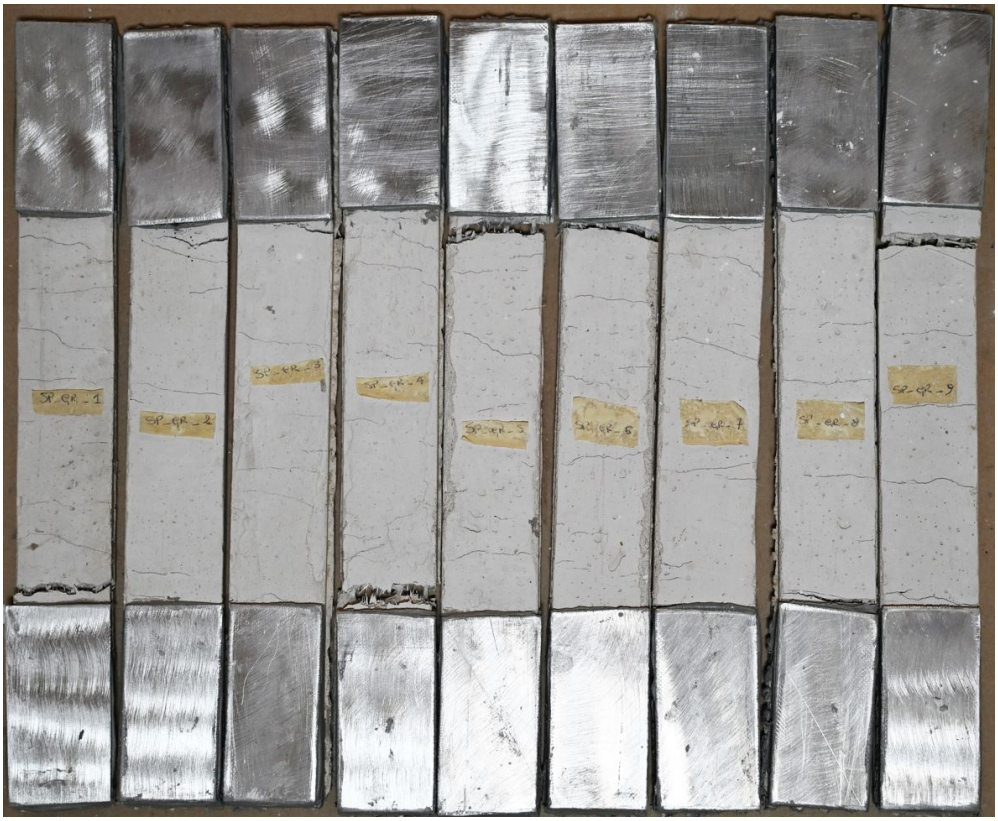

Figure 3.10: Specimens of group GL_TF after testing.

The experimental results for the four groups of specimens are reported below in terms of stress-strain curves (Figures 3.11), being the stress values calculated by dividing the recorded load by the cross-sectional area of the bare textile (F/A_f), as suggest by the American Code AC434 [12].

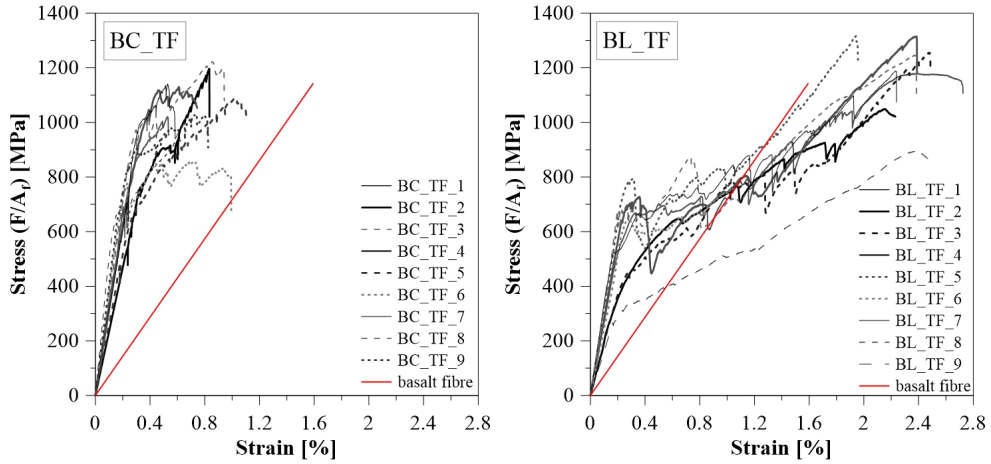

(a) BFRCM with cement-based mortar **(b)** BFRCM with lime-based mortar

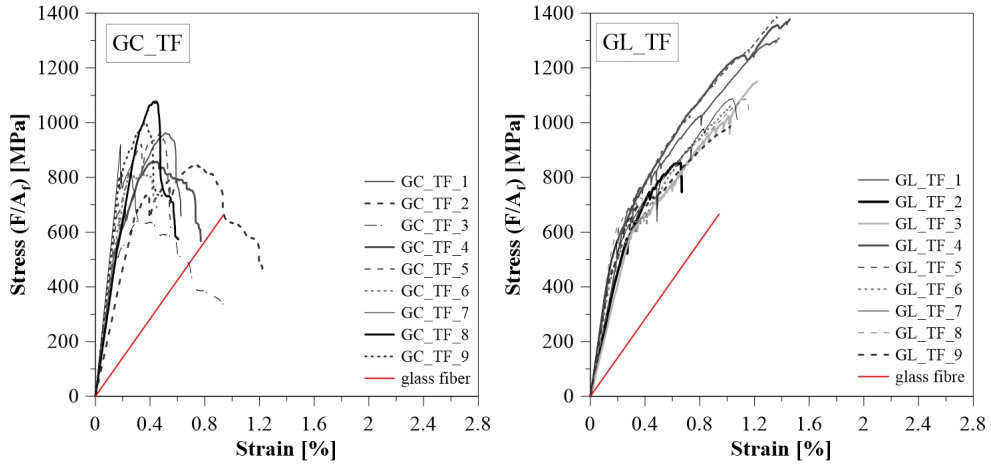

(c) GFRCM with cement-based mortar **(d)** GFRCM with lime-based mortar

Figure 3.11: Stress-strain curves of BFRCM and GFRCM composites: tensile tests with clamping grip method.

Tables 3.7, 3.8, 3.9 and 3.10 list the main experimental results for the four groups of specimens BC_TF, BL_TF, GC_TF and GL_TF.

Data are in terms of peak stresses (σ_I, σ_{II} and σ_{III}) and corresponding strains (ε_I, ε_{II} and ε_{III}), evaluated at the end of each stage of the stress-strain

curves according to Figure 3.4. The ratio between stage III peak stress (σ_{III}) and grid strength (f_{fu}) is also provided (normalised composite peak stress).

The average strengths and the Coefficient Of Variation (COV) are calculated excluding some results due to some inconsistencies. Despite, the results from identical specimens are compared, some differences were observed. In general, not all curves follow the same trend, but in some cases (e.g. specimens of group BC_TF and GC_TF) the second and the third phase are absent and the first branch extends directly up to the failure. This can be attributed to some drawbacks in the performance in tension of the FRCM strip, significantly affected by the possible misalignment of the reinforcement layer and the unexpected slippage in the gripping area.

Additionally, a certain scatter is also observed in the first cracking stress (σ_I) and the slope corresponding to the first un-cracked phase (e.g. specimens of group BL_TF and GL_TF). These latter may be attributed to manufacturing defects but also to the variability in the mortar properties (e.g. tensile properties, thicknesses and widths may vary significantly).

Considering the average values of load at the end of Stage I (F_{cr} first cracking load) for each sets of specimens, the corresponding stress in the mortar (σ_I) is evaluated by dividing the load by the homogenized cross-section of the composite systems, in which the area of the textile is amplified by the ratio between the tensile elastic modulus of the two materials (fibre and matrix).

The obtained stress values at the transition point are always lower compared to the experimental flexural strength of the mortar ($f_{m,f}$): the average values of 2.97 MPa and 2.78 MPa are found for specimens of series BC_TF and GC_TF respectively, with reductions of 54% and 57% with respect to the flexural strength of the cement-based mortar (average value $f_{m,f}$=6.40 MPa). Moreover, average values of 2.39 MPa, and 2.38 MPa are found for specimens of series BL_TF and GL_TF respectively, with a reductions of 55% with respect to the flexural strength of the lime-based mortar (average value $f_{m,f}$=5.30 MPa).

The values of the tensile strength σ_{III} for specimens of series BC_TF and BL_TF are comparable to the tensile strength of the basalt grid (f_{fu}=1142.2 MPa), as shown in Figures 3.11(a) and 3.11(b). The corresponding ratios between the maximum strength in composite coupons and the average experimental strength of dry fibres (σ_{III}/f_{fu}) are listed in Tables 3.7 and 3.8, respectively. About curves of specimens of group BL_TF (Figure 3.11(b)), the axial stiffness of the composite material at Stage III decrease with respect to the theoretical

value based on the axial stiffness of the bare basalt grid due to the rupture of some fibre yarns during the previous Stage II.

It is worth pointing out that the average maximum stress values for specimens of group GC_TF (σ_{III}=921.0 MPa) and GL_TF (σ_{III}=1229.8 MPa) are about the 38% and 85% greater than the maximum strength of bare glass textile (f_{fu}=665.4 MPa), respectively. All the results are listed in Table 3.9 and 3.10.

Table 3.7: Results of BFRCM coupons with cement-based mortar (BC_TF group) in Stage I, II and III

Sample ID	σ_I [MPa]	ε_I [%]	σ_{II} [MPa]	ε_{II} [%]	σ_{III} [MPa]	ε_{III} [%]	σ_{III}/f_{fu} [-]
BC_TF_1	691.1	0.20	-	-	1020.3	0.53	0.89
BC_TF_2	762.5*	0.33*	-	-	1196.8*	0.83*	1.05*
BC_TF_3	678.2*	0.17*	-	-	941.8*	0.60*	0.82*
BC_TF_4	1042.4	0.39	-	-	1129.5	0.61	0.99
BC_TF_5	450.3*	0.18*	-	-	1091.3*	1.03*	0.96*
BC_TF_6	760.2*	0.23*	-	-	854.6*	0.72*	0.75*
BC_TF_7	573.0	0.19	-	-	1141.4	0.53	1.00
BC_TF_8	965.3	0.30	-	-	1221.7	0.85	1.07
BC_TF_9	648.5	0.16	-	-	1027.0	0.73	0.90
Average	**784.1**	**0.25**	**-**	**-**	**1108.0**	**0.65**	**0.97**
COV	**(23.6 %)**	**(33.2 %)**	**-**	**-**	**(6.8 %)**	**(19.0 %)**	**-**

*values excluded from the calculation of the average and COV

Table 3.8: Results of BFRCM coupons with lime-based mortar (BL_TF group) in Stage I, II and III

Sample ID	σ_I [MPa]	ε_I [%]	σ_{II} [MPa]	ε_{II} [%]	σ_{III} [MPa]	ε_{III} [%]	σ_{III}/f_{fu} [-]
BL_TF_1	659.6	0.35	-	-	1178.8	2.39	1.03
BL_TF_2	641.4*	0.66*	-	-	1049.0*	2.15*	0.92*
BL_TF_3	451.6*	0.28*	834.4*	1.69*	1255.2*	2.22*	1.10*
BL_TF_4	684.3	0.29	782.2	1.37	1314.9	2.39	1.15
BL_TF_5	791.4*	0.31*	764.6*	1.01*	1316.21*	1.94*	1.15*
BL_TF_6	650.4	0.28	647.7	1.18	1153.4	2.20	1.01
BL_TF_7	522.6	0.20	-	-	1188.6	2.23	1.04
BL_TF_8	650.1	0.21	710.5	1.10	1246.4	2.37	1.09
BL_TF_9	337.9*	0.29*	518.5*	1.22*	896.1*	2.41*	0.78*
Average	**633.4**	**0.27**	**713.5**	**1.21**	**1216.4**	**2.32**	**1.06**
COV	**(9.0%)**	**(21.1%)**	**(7.7%)**	**(9.5%)**	**(4.8%)**	**(3.5%)**	**-**

*values excluded from the calculation of the average and COV

Table 3.9: Results of GFRCM coupons with cement-based mortar (GC_TF group) in Stage I, II and III

Sample ID	σ_I [MPa]	ε_I [%]	σ_{II} [MPa]	ε_{II} [%]	σ_{III} [MPa]	ε_{III} [%]	σ_{III}/f_{fu} [-]
GC_TF_1	533.6	0.14	-	-	962.6	0.51	1.45
GC_TF_2	673.8*	0.32*	-	-	845.7*	0.73*	1.27*
GC_TF_3	577.7*	0.16*	-	-	643.7*	0.32*	0.97*
GC_TF_4	678.9	0.22	-	-	858.3	0.42	1.29
GC_TF_5	700.1	0.17	-	-	964.0	0.48	1.45
GC_TF_6	644.9	0.18	-	-	821.4	0.26	1.23
GC_TF_7	907.4	0.18	-	-	919.9	0.18	1.38
GC_TF_8	542.2*	0.16*	-	-	1077.5*	0.43*	1.62*
GC_TF_9	804.4	0.17	-	-	1000.0	0.37	1.50
Average	**711.5**	**0.18**	**-**	**-**	**921.0**	**0.37**	**1.38**
COV	**(16.7 %)**	**(12.2 %)**	**-**	**-**	**(6.8 %)**	**(31.5 %)**	**-**

*values excluded from the calculation of the average and COV

Table 3.10: Results of GFRCM coupons with lime-based mortar (GL_TF group) in Stage I, II and III

Sample ID	σ_I [MPa]	ε_I [%]	σ_{II} [MPa]	ε_{II} [%]	σ_{III} [MPa]	ε_{III} [%]	σ_{III}/f_{fu} [-]
GL_TF_1	682.2	0.29	-	-	1308.9	1.38	1.97
GL_TF_2	572.4*	0.27*	-	-	855.7*	0.65*	1.29*
GL_TF_3	589.3	0.30	-	-	1150.8	1.22	1.73
GL_TF_4	601.2	0.22	-	-	1378.1	1.46	2.07
GL_TF_5	756.1	0.37	-	-	1387.5	1.36	2.09
GL_TF_6	504.9	0.20	-	-	1208.6	1.45	1.82
GL_TF_7	553.4	0.18	-	-	1087.8	1.04	1.63
GL_TF_8	616.9	0.21	-	-	1086.6	1.13	1.63
GL_TF_9	436.5*	0.15*	-	-	986.8*	1.02*	1.48*
Average	**614.9**	**0.25**	**-**	**-**	**1229.8**	**1.29**	**1.85**
COV	**(12.5 %)**	**(24.9 %)**	**-**	**-**	**(9.7 %)**	**(11.8 %)**	**-**

*values excluded from the calculation of the average and COV

Comparing the results, it is evident that the four sets of composite samples show very different behaviour. In detail, BFRCM and GFRCM with cement-based mortar show a brittle behaviour. It is due to the FRCM systems with an high-strength matrix (i.e. cement-based mortar) are unable to exploit the maximum elongation of the fibre textile, therefore coupons reach the failure for low values of strain, ε_{III}=0.65% and ε_{III}=0.37% for specimens of group BC_TF and GC_TF, respectively. Differently, BFRCM and GFRCM with lime-based

mortar show a more ductile behaviour. Figure 3.11 is very effective in showing how the composites are affected by the different components (i.e. cement or lime-based mortar, basalt or glass fibre). In particular, the composite strength of BFRCM coupons is comparable with the basalt grid strength. While, the peak stress values (σ_{III}) of GFRCM coupons are greater than the grid strength, probably due to the effect of the adhesion promoter for glass grid.

3.2.2 Results from clevis grip method

As in the previous section 3.2.1, the results of tensile tests on BFRCM and GFRCM composites adopting clevis grip method are presented in terms of load-strain curves and stress-strain curves. Moreover, the outcomes in terms of peak stresses and corresponding strains evaluated at the end of each stage of the tensile stress-strain curves are listed in tabular form, for a more convenient comparison between the four series of FRCM systems.

The results in terms of load-strain curves for BFRCM and GFRCM composites with cement-based and lime-based mortar are presented in Figures 3.12.

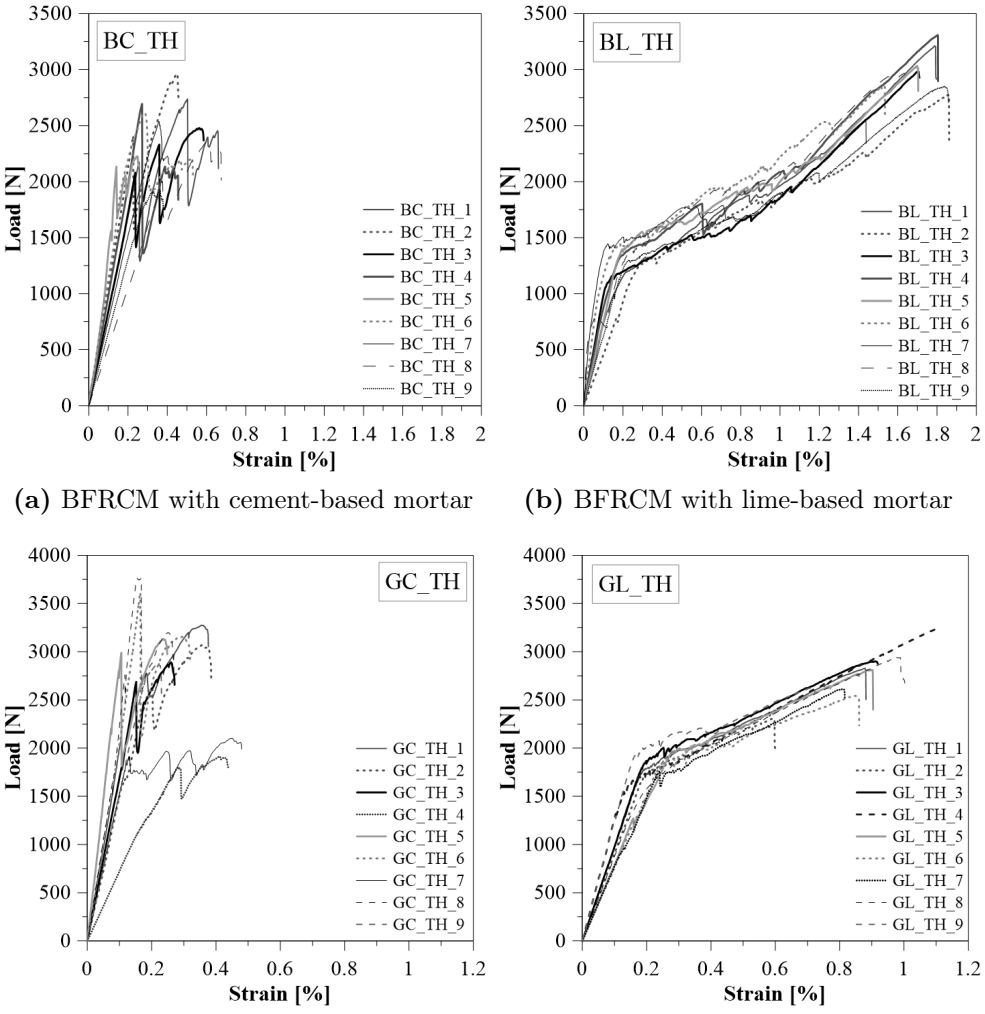

(a) BFRCM with cement-based mortar **(b)** BFRCM with lime-based mortar

(c) GFRCM with cement-based mortar **(d)** GFRCM with lime-based mortar

Figure 3.12: Load-strain curves of BFRCM and GFRCM composite coupons, tested with clevis grip method.

It should be observed that the mechanical response of BFRCM and GFRCM samples with cement-based mortar (Figure 3.12(a) and 3.12(c)) shows a tensile behaviour different from the idealized tri-linear curve.

All specimens presented an initial linear response up to the first cracking load (F_{cr}), followed by a limited second branch up to the coupon failure, due

to the brittle fibre rupture.

It is worth observing that in some case, sliding in the gripping area provides a certain scatter in the slope of the first branch, see Figures 3.12(a) and 3.12(c). The first linear stage is clearly recognizable from a sudden load drop, caused by the opening of a first crack in the mortar. Moreover, in some case the Stage I is followed by the failure or a limited post-peak phase, which suggests a good adhesion between the two materials in contact and a lower fibre exploitation ratio. When the crack opens up a significant load drop is observed, as shown in Figure 3.13 for specimens BC_TH_1 and BC_TH_3. Indeed, the number of load drops strictly depends on the number of cracks (Figure 3.13(b)).

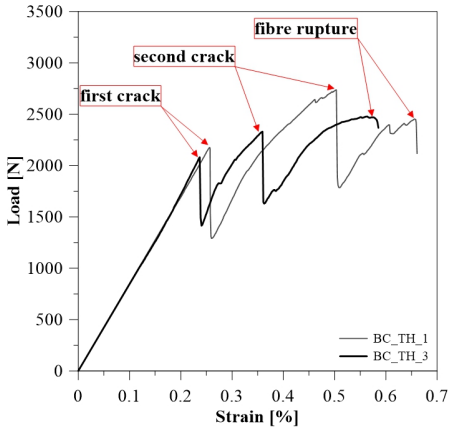

(a) Load-strain response

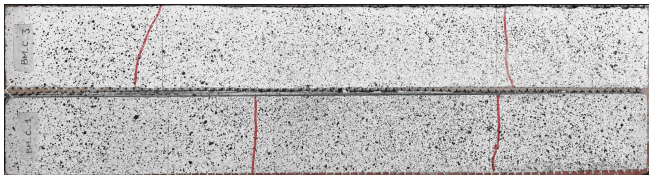

(b) Specimens after testing

Figure 3.13: Mechanical response of BFRCM with cement-based mortar.

Generally, specimens of series BC_TH fail after the formation of a single crak. The formation of two cracks is observed only in three coupons (BC_TH_1, BC_TH_3 and BC_TH_8). The main failure mode consists in fibre rupture close the gripping area, as shown in Figure 3.14, where the first crack in the mortar layer opens up due to the shear stress concentration.

Only in two coupons, i.e. BC_TH_6 and BC_TH_7, the failure occurs in the middle of the specimen length. It is probably due to an initial curvature presenting in the composite strip assumed during the curing period in water.

Figure 3.14: Specimens of group BC_TH after testing.

Differently, for specimens of group GC_TH, the telescopic rupture of the glass fibre yarns (Figure 3.15) after the formation of a single crack close the griping area is observed, as shown in Figure 3.16.

Figure 3.15: Telescopic rupture of glass fibre yarns.

Figure 3.16: Specimens of group GC_TH after testing.

An almost bi-linear trend is observed for the FRCM coupons with lime-based mortar, i.e. group BL_TH and GL_TH, as shown in Figures 3.12(b) and 3.12(d).

The second stage has almost the same slope of the third stage due to the slippage of the fibre caused by the clevis grip system.

The un-cracked stage is mainly governed by the tensile strength of the lime-based mortar, here the slope of the linear branch is subjected to variations due to some sliding of the coupons in the gripping area.

The Stage II of curves related to samples of group BL_TH (Figure 3.12(b)), is characterized by the development of several cracks with the slippage of the basalt textile within the embedding matrix. At the end of the Stage II, the delamination at the fibre-mortar interface occurs (Figure 3.17) and the Stage III assumes the slope of the basalt fibre reinforcement up to reach the failure. Specimens after testing are shown in Figure 3.18.

Figure 3.17: Delamination at the fibre-mortar interface for coupons of group BL_TH.

Figure 3.18: Specimens of group BL_TH after testing.

The Stage II of curves related to samples of group GL_TH (Figure 3.12(d)), is characterized by small load drops corresponding to the development and opening of multiple cracks. The Stage III assumes a linear behaviour where the main contribute is given by the glass textile. A good adhesion is established between the glass grid and the lime-based mortar probably due to the presence of the adhesion promoter. Coupons after testing denote several cracks and the brittle fibre rupture (Figure 3.19).

Figure 3.19: Specimens of group GL_TH after testing.

The experimental results are reported in terms of stress-strain curves and compared with the average linear behaviour of the bare fibre grid (red line in Figures 3.20) in order to evaluate the FRCM behaviour as a function of fibre-mortar combination, when clevis grip method is adopted for tensile tests.

The stress values are calculated by dividing the recorded load by the cross-sectional area of the bare textile A_f, as suggest by the American Code AC434 [12].

The experimental data in terms of stress values (σ_I, σ_{II} and σ_{III}) and corresponding strains (ε_I, ε_{II} and ε_{III}), evaluated at the end of each stage of the tensile stress-strain curves (i.e. un-cracked, crack development and cracked stage), are summarized in Tables 3.11, 3.13, 3.12 and 3.14.

The comparison between the average stress values in the mortar at the end of Stage I and the flexural strength of the mortar, highlights that: the average values of 3.87 MPa and 4.28 MPa of specimens of series BC_TH and GC_TH respectively, are lower of 40% and 33% with respect to the flexural strength of the cement-based mortar (average value $f_{m,f}$=6.40 MPa); average values of 2.00 MPa, and 2.73 MPa are found for specimens of series BL_TH and GL_TH respectively, with a reductions of 62% and 49% with respect to the

flexural strength of the lime-based mortar (average value $f_{m,f}$=5.30 MPa).

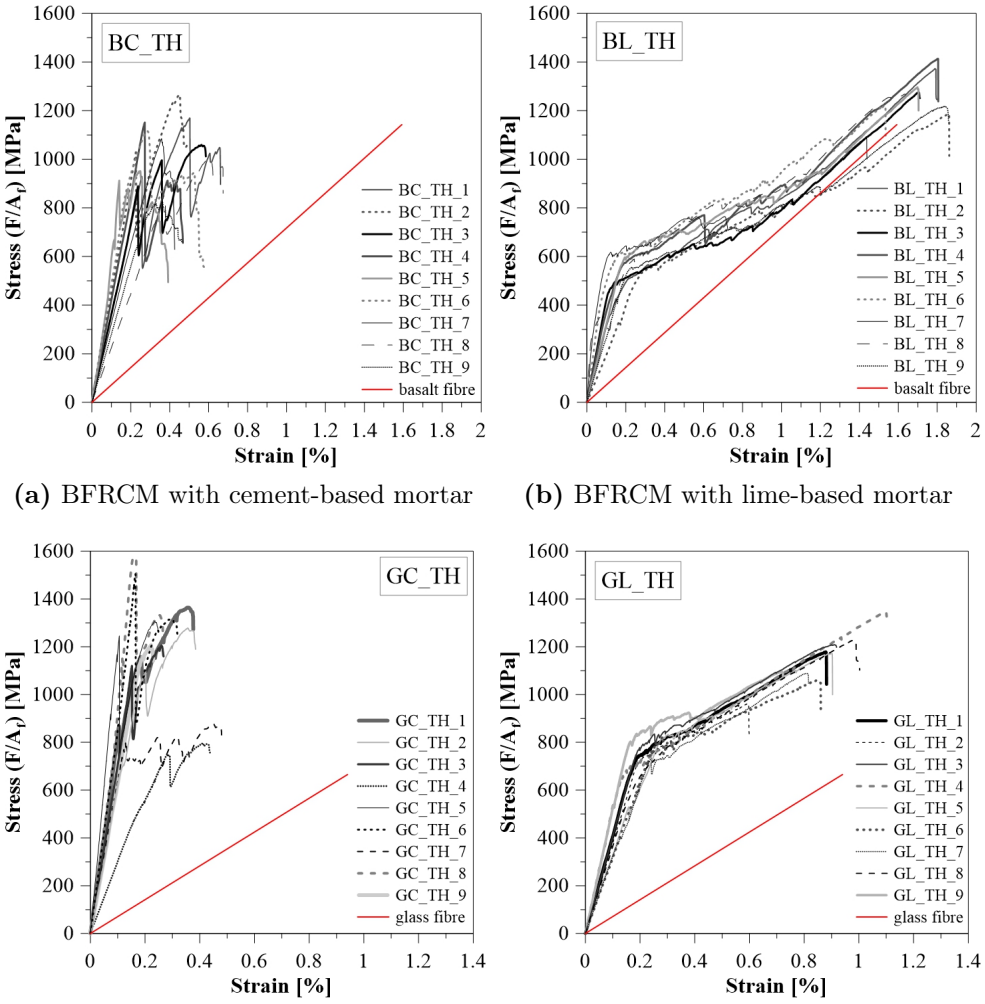

(a) BFRCM with cement-based mortar **(b)** BFRCM with lime-based mortar

(c) GFRCM with cement-based mortar **(d)** GFRCM with lime-based mortar

Figure 3.20: Stress-strain curves of BFRCM and GFRCM composites: tensile tests with clevis grip method.

As discussed above, both for BFRCM and GFRCM with cement-based mortar (BC_TH and GC_TH group), the high-strength matrix and good matrix-fibre bond capacity provide the absence of the Stage II and a very limited Stage

III, in some cases even absent (see Figures 3.20(a) and 3.20(c)).

Consequently, these two groups of specimens achieve a very low average ultimate strain ε_{III} equal to 0.35 % and 0.29 %, with reductions of 78 % and 74 % respect to the maximum elongation of the basalt (ε_u=1.61 %) and glass (ε_u=1.09 %) textile, respectively. All the results are in Tables 3.11 and 3.12.

Table 3.11: Results of BFRCM coupons with cement-based mortar (BC_TH group) in Stage I, II and III

Sample ID	σ_I [MPa]	ε_I [%]	σ_{II} [MPa]	ε_{II} [%]	σ_{III} [MPa]	ε_{III} [%]	σ_{III}/f_{fu} [-]
BC_TH_1	925.3	0.21	-	-	1170.0	0.40	1.02
BC_TH_2	1015.9	0.18	-	-	1266.1	0.36	1.11
BC_TH_3	889.4	0.19	-	-	1059.1	0.45	0.93
BC_TH_4	1151.3	0.22	-	-	1151.3	0.22	1.01
BC_TH_5	912.3*	0.11*	-	-	951.8*	0.20*	0.83*
BC_TH_6	1116.6*	0.23*	-	-	1116.6*	0.23*	0.98*
BC_TH_7	1085.1*	0.29*	-	-	1085.1*	0.29*	0.95*
BC_TH_8	847.5*	0.30*	-	-	1004.6*	0.48*	0.88*
BC_TH_9	809.35*	0.26*	-	-	825.4*	0.29*	0.72*
Average	**995.4**	**0.20**	**-**	**-**	**1161.6**	**0.36**	**1.01**
COV	**(10.2 %)**	**(7.6 %)**	**-**	**-**	**(6.3 %)**	**(24.4 %)**	**-**

*values excluded from the calculation of the average and COV

Table 3.12: Results of GFRCM coupons with cement-based mortar (GC_TH group) in Stage I, II and III

Sample ID	σ_I [MPa]	ε_I [%]	σ_{II} [MPa]	ε_{II} [%]	σ_{III} [MPa]	ε_{III} [%]	σ_{III}/f_{fu} [-]
GC_TH_1	867.3	0.10	-	-	1364.3	0.35	2.05
GC_TH_2	1074.7	0.20	-	-	1278.5	0.36	1.92
GC_TH_3	1119.9	0.15	-	-	1204.4	0.26	1.81
GC_TH_4	745.0*	0.29*	-	-	796.1*	0.41*	1.20*
GC_TH_5	1232.4	0.10	-	-	1305.2	0.23	1.96
GC_TH_6	1505.3*	0.16*	-	-	1505.3*	0.16*	2.26*
GC_TH_7	797.5*	0.13*	-	-	876.8*	0.44*	1.32*
GC_TH_8	1563.3*	0.17*	-	-	1568.3*	0.17*	2.36*
GC_TH_9	1206.7	0.22	-	-	1206.7	0.22	1.81
Average	**1100.2**	**0.16**	**-**	**-**	**1271.8**	**0.29**	**1.91**
COV	**(11.8 %)**	**(30.9 %)**	**-**	**-**	**(4.8 %)**	**(20.5 %)**	**-**

*values excluded from the calculation of the average and COV

In any way, the fibre strength is exploited in both the cases. In regard

to maximum stress values σ_{III} for specimens of group BC_TH, the average value (1161.66 MPa) is quite close to basalt fibre strength (f_{fu}=1142.2 MPa). For specimens of group GC_TH, there is a marked increment (+91 %) of the average maximum stress σ_{III}=1271.8 MPa, respect to glass fibre strength (f_{fu}=665.4 MPa).

Observing the curves for the FRCM coupons with lime-based mortar (Figures 3.20(b) and 3.20(d)), a different mechanical response is remarked respect to the FRCM coupons with cement-based mortar. The main results are listed in Tables 3.13 and 3.14.

In regard to Stage I for series BL_TH and GL_TH, the average strain values (ε_I=0.19 % and ε_I=0.20 %, respectively) are quite similar. However, the peak stress of series GL_TH (σ_I=706.2 MPa) is about the 25 % greater than the first peak of series BL_TH (σ_I=530.7 MPa).

For Stage II, the average stress values (σ_{II}=892.7 MPa and σ_{II}=878.3 MPa, respectively) are still close, but there is a marked reduction of the average maximum strain ε_{II} from 1.13 % to 0.43 % for series BL_TH and GL_TH, respectively.

Finally, the curves (Figures 3.20(b) and 3.20(d)) show that the fibre strength is exploited. The ratio between the tensile strength in composite coupons and the average experimental strength of dry basalt and glass fibres σ_{III}/f_{fu} are 1.11 and 1.70, respectively.

Table 3.13: Results of BFRCM coupons with lime-based mortar (BL_TH group) in Stage I, II and III

Sample ID	σ_I [MPa]	ε_I [%]	σ_{II} [MPa]	ε_{II} [%]	σ_{III} [MPa]	ε_{III} [%]	σ_{III}/f_{fu} [-]
BL_TH_1	514.6	0.23	822.7	0.97	1372.5	1.79	1.20
BL_TH_2	509.2*	0.26*	955.6*	1.45*	1184.9*	1.86*	1.04*
BL_TH_3	484.0	0.15	814.8	1.06	1274.4	1.71	1.12
BL_TH_4	577.8	0.20	915.9	1.12	1413.7	1.80	1.24
BL_TH_5	596.5	0.21	938.2	1.21	1296.4	1.70	1.14
BL_TH_6	608.4	0.22	1034.8	1.27	1220.9	1.53	1.07
BL_TH_7	602.0	0.13	819.1	1.06	1086.9	1.44	0.95
BL_TH_8	307.5	0.10	938.2	1.12	1268.2	1.63	1.11
BL_TH_9	554.6	0.26	857.2	1.20	1217.7	1.84	1.07
Average	**530.7**	**0.19**	**892.7**	**1.13**	**1268.8**	**1.68**	**1.11**
COV	**(17.7%)**	**(27.2%)**	**(8.2%)**	**(8.0%)**	**(7.4%)**	**(7.8%)**	**-**

*values excluded from the calculation of the average and COV

Table 3.14: Results of GFRCM coupons with lime-based mortar (GL_TH group) in Stage I, II and III

Sample ID	σ_I [MPa]	ε_I [%]	σ_{II} [MPa]	ε_{II} [%]	σ_{III} [MPa]	ε_{III} [%]	σ_{III}/f_{fu} [-]
GL_TH_1	742.4	0.20	852.7	0.38	1178.4	0.88	1.77
GL_TH_2	709.7	0.19	793.4	0.33	962.7	0.59	1.45
GL_TH_3	766.0	0.20	935.8	0.47	1208.4	0.91	1.82
GL_TH_4	659.1*	0.14*	808.1*	0.34*	1346.3*	1.10*	2.02
GL_TH_5	493.9	0.16	915.4	0.48	1171.7	0.90	1.76
GL_TH_6	786.8	0.26	847.4	0.47	1059.3	0.85	1.59
GL_TH_7	724.7*	0.24*	807.2*	0.39*	1088.6*	0.81*	1.64*
GL_TH_8	647.5	0.20	-	-	1226.5	0.98	1.84
GL_TH_9	797.3	0.17	925.3	0.44	1095.1	0.72	1.65
Average	**706.2**	**0.20**	**878.3**	**0.43**	**1128.9**	**0.83**	**1.70**
COV	**(14.0%)**	**(15.5%)**	**(5.8%)**	**(12.6%)**	**(7.8%)**	**(14.7%)**	**-**

*values excluded from the calculation of the average and COV

Further information about crack pattern evolution and the strain distribution for coupons tested adopting clevis grip method are presented in the following section.

3.2.3 Results from analysis with virtual extensometers (DIC)

DIC technique is used as measurement system for specimens tested with clevis grip method (Figure 3.21). It provides additional information on local stress distribution and damage pattern (crack location).

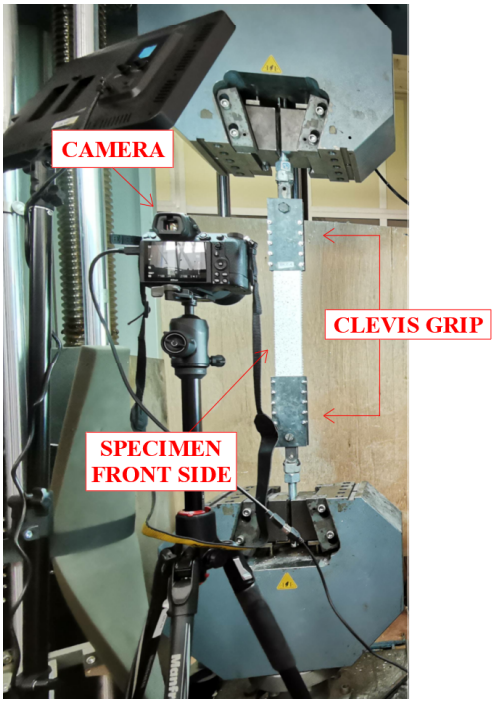

Figure 3.21: Set-up for tensile test on specimens tested with clevis grip method.

The virtual extensometers are placed in the front side of each specimen, in accordance with the observed crack pattern.

In general, for specimens of group BC_TH and GC_TH, characterized by the formation of one or maximum two cracks, the strain values are evaluated respect to the total investigable length equal to 250 mm. Two virtual extensometers are positioned at the extremities of the specimen surface and one at the central axis of the sample, as shown in Figure 3.22(a). The comparison between the outcomes of these measurements (Figure 3.22) is useful to check the uniformity of the load distribution along the face of the tested specimens and to confirm the absence of load eccentricities.

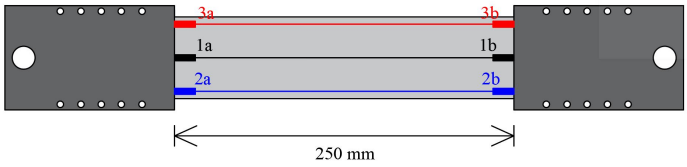

(a) Extensometers position

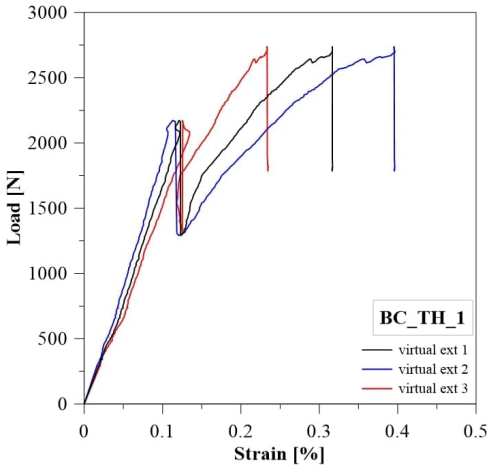

(b) Load-strain curves obtained for specimen BC_TH_1

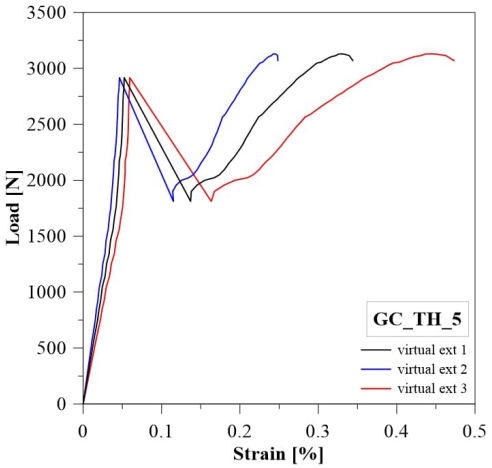

(c) Load-strain curves obtained for specimen GC_TH_5

Figure 3.22: Variability of strain values from DIC analysis obtained changing the position of the virtual extensometer for specimens with few cracks.

The correlation of the curves for the three virtual extensometers, highlights a scatter between the strains at peak stress ranges from 4.3% and 21% for BC_TH_1 (Figure 3.22(b)) and from 10.2% and 24.2% for GC_TH_5 (Figure 3.22(c)). The difference in the results of the three extensometers, for the selected specimens, evidences a not really uniform load distribution over the cross-section of specimen, especially after the formation of the first crack. This is probably due to the slipping in the gripping area during the loading phase and the consequent rotation in plain of the specimens after the formation of the first crack, causing the eccentric load transfer.

For samples characterized by the development of many cracks in the middle part, i.e. specimens of group BL_TH and GL_TH, a fourth virtual extensometer 80 mm long is selected, in accordance with the expected failure in the middle part of the coupons, see Figure 3.23(a).

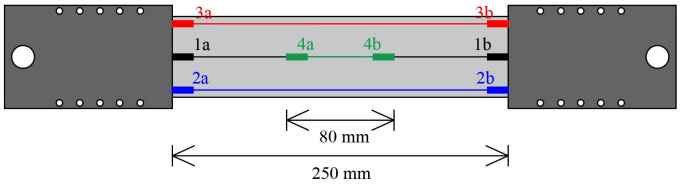

(a) Extensometers position

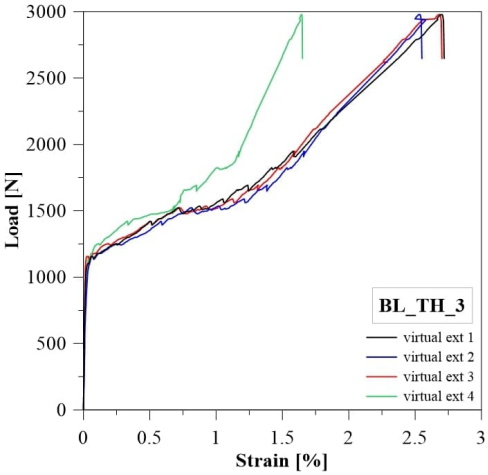

(b) Load-strain curves obtained for specimen BL_TH_3

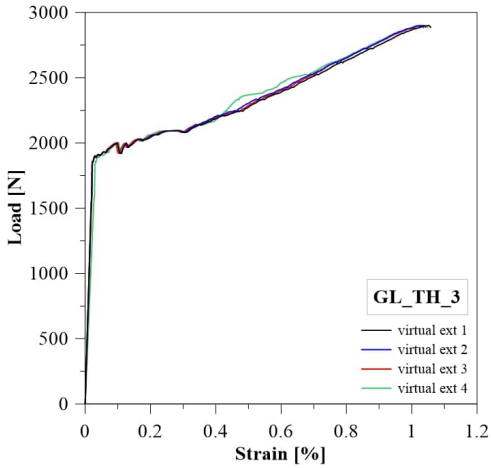

(c) Load-strain curves obtained for specimen GL_TH_3

Figure 3.23: Variability of strain values from DIC analysis obtained changing the position of the virtual extensometer for specimens with numerous cracks.

The curves in Figure 3.23(b) indicate that the results of the correlation for the three virtual extensometers positioned along the total length of the sample BL_TH_3 are not scattered.

However, a significant difference in the trend can be observed when comparing them with the fourth extensometer positioned in the middle part in a length of 80 mm. This is because the reference points of the three virtual extensometers with length of 250 mm are located near a section where a crack appears (Figure 3.24(a)), providing an apparent lower stiffness of the post-first-crack stages, i.e. Stage II and Stage III.

It is a good practice monitoring the samples, positioning the virtual extensometers far from the sections where cracks are expected to develop (Figure 3.24(b)).

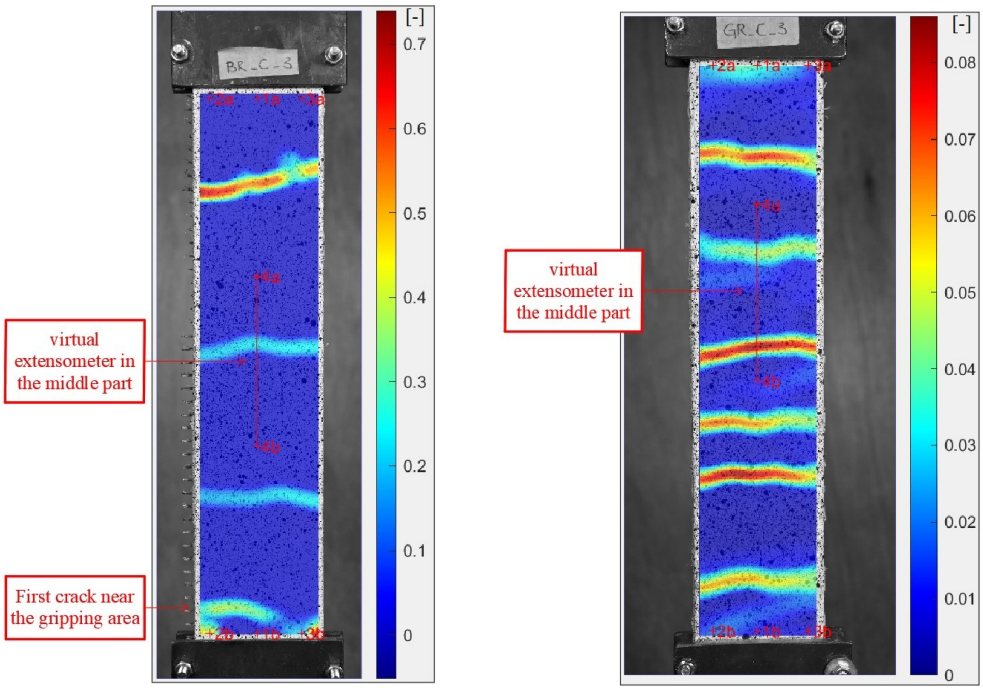

(a) specimen BL_TH_3 **(b)** specimen GL_TH_3

Figure 3.24: Strain contours with the virtual extensometers exported from Ncorr.

Considering the readings of the four extensometers positioned in specimen GL_TH_3 (Figure 3.23(c)), the scatter between the strains at peak stress is between the 1% and 4%. This result confirms the absence of important unexpected bending effects in the plane of the specimens.

3.2.4 Load-strain curves from DIC analysis

As it is shown in the previous section, a certain scatter is observed in the readings of virtual extensometers positioned on the surface of the samples of group BC_TH and GC_TH. It is probably due to the presence of defects in the performance of the test set-up.

Differently, in the case of specimens of group BL_TH and GL_TH the measurements from virtual extensometers positioned on the surface highlighting the absence of significant defects in the specimens or in the test set-up.

For this reason, in the following the load-strain curves for specimens of

group BL_TH and GL_TH are analyzed with reference to the measurement recorded by the virtual extensometer selected in the middle part of the front side of each specimen.

The characteristic tensile behaviour of the FRCM systems is shown for one sample BL_TH_3 in Figure 3.25 with the indication of the three typical stages and the points of the curve corresponding to the opening of new cracks in the mortar during the second stage.

Moreover, the evolution of the strain pattern obtained through the use of the DIC technique is shown in Figure 3.26.

For each specific point of the load-strain curve (indicate with a letter "a", "b", "c", "d", "e" and "f"), shown in Figure 3.25, is reported the corresponding image exported from Ncorr (Figure 3.26).

The first un-cracked stage (Stage I) is characterized by a linear branch up to the first point "a" (P_I, ε) of the curve (Figure 3.25), corresponding to the opening of the first crack in the mortar (Figure 3.26(a)). During this stage, the mortar provides the most contribution to both load bearing capacity and stiffness.

In this stage, the tensile elastic modulus E_I can be estimated referring to the fiber cross-section.

The occurrence of the first crack in the mortar identify the beginning of the second stage (Stage II), characterized by the formation of several cracks in the mortar, close to the gripping area (Figure 3.26(b)) and along the total length of the specimen (Figure 3.26(d)) up to achieve the crack saturation (Figure 3.26(e)), corresponding to point "e" of the curve (Figure 3.25). Generally, this stage is characterized by several load drops due to the fracture energy that is released after the crack opening and a stiffness E_{II}. The latter is calculated through a proper linear interpolation.

In the last stage (Stage III) additional imposed global displacement causes the widening of existing cracks (Figure 3.26(f)), during this stage new cracks are not developed generally. The curve assumes a more regular trend and the stiffness increases.

Moreover, the load bearing capacity P_{III} and the tensile stiffness E_{III} mainly depend on the strength and stiffness of fabric alone.

In some case, the un-cracked mortar between the cracks may still provide a contribution in the redistribution of the tensile load due to the residual interlooking at the fibre-mortar interface.

This stage ends when the fibre rupture occurs (Figure 3.26(f)), corresponding to the point "f" of the curve (Figure 3.25).

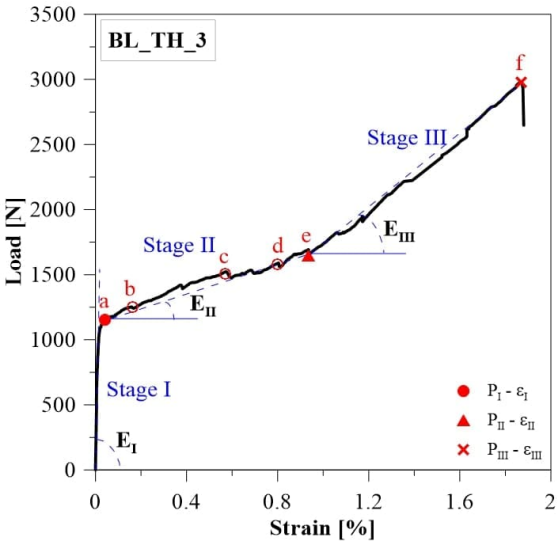

Figure 3.25: Load-strain curve of specimen BL_TH_3 with the indication of different stages and characteristic points.

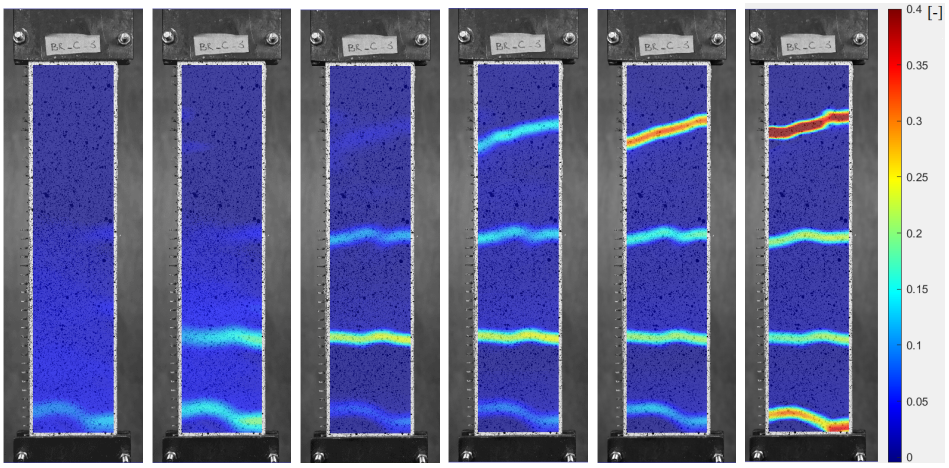

Figure 3.26: Strain pattern evolution for specimen BL_TH_3 exported from Ncorr.

The tensile load-strain curves obtained from DIC analysis, considering the measurements provide by the virtual extensometer 80 mm long and settled in

the middle part of the specimen surface, for samples of group BL_TH and GL_TH are reported in Figures 3.27(a) and 3.27(b), respectively.

The comparison between the two considered composite systems, i.e. BFRCM (group BL_TH) and GFRCM (group GL_TH) with lime-based mortar, point out a significant difference in the trend of the experimental curves (Figure 3.27).

The curves referred to BFRCM (Figure 3.27(a)) shows a trend uneven after the first crack opening (P_I) characterized by several load drops. While a more smooth trend is observed for GFRCM (Figure 3.27(b)). The mismatch between the tensile behaviour of these two FRCM systems derives from the established fibre-mortar interaction. The lime-based mortar establishes a poor chemical bond with the coated basalt textile, for this reason the mortar-to-fibre stress transfer capacity is low and provides the slippage of the fibre textile followed by the detachment of the mortar layer. Differently, the glass dry textile establishes a good fibre-to-mortar interlocking due to the use of the adhesion promoter that ensure the impregnation of the external wires of the yarn. In this case the telescopic failure is generally observed because the mortar-to-external wires stress transfer capacity is higher than the wire-to-wire one.

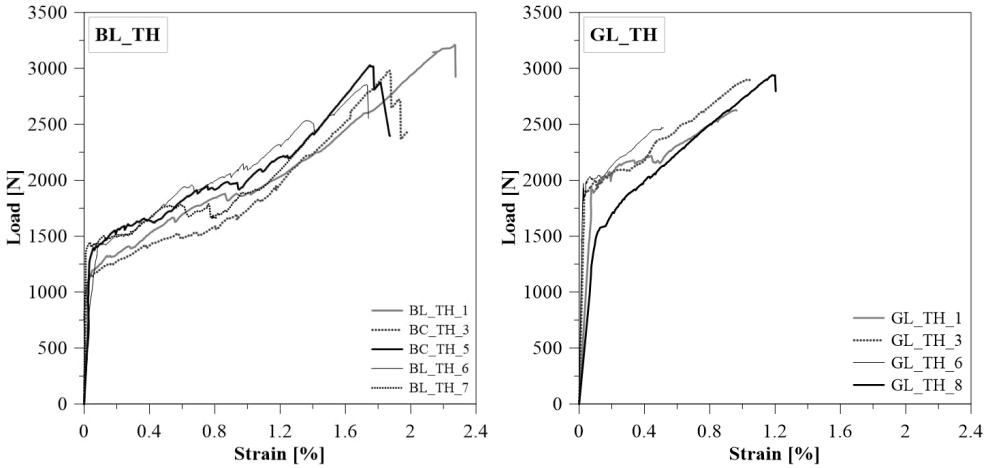

(a) BFRCM with lime-based mortar **(b)** GFRCM with lime-based mortar

Figure 3.27: Load-strain curves from DIC analysis.

It is worth pointing out that the measurements by DIC analysis provide values of the strain different from those provided by the testing machine presented in the previous Section 3.2.2. The latter are obtained from the global

displacement recorded by the testing machine, while the strain values from DIC analysis are evaluated by the central virtual extensometer positioned on the front side of each specimen in accordance with the observed crack pattern.

In general, the DIC measurements provide a more rigid first branch and and a lower slope of the third branch compared to the curves obtained by the measurement of the testing machine, as shown in the two comparisons reported in Figures 3.28(a) and 3.28(b). It is probably due to the fact that the testing machine provides a global measurement potentially affected by unexpected slippage. In particular, comparing the strain values from the two measurement systems (testing machine and DIC technique) and referring to the first un-cracked linear branch (Stage I) a difference of about the 74% and 72% is observed for specimens of group BL_TH and GL_TH, respectively. The variability between strains obtained by the two methods decreases in the Stage II (9% and 16%, respectively) up to a negligible percentage of 4% and 2% observed in the Stage III for the two groups of specimens, respectively.

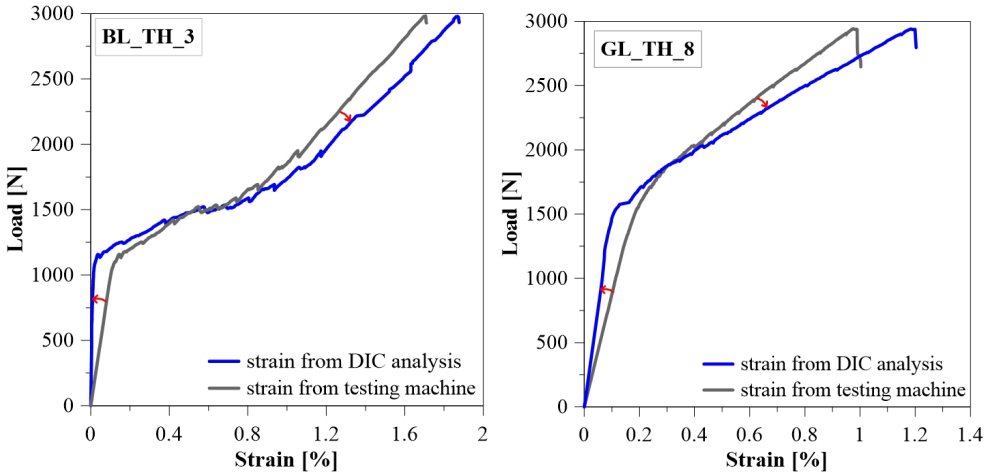

(a) specimen BL_TH_3 **(b)** specimen GL_TH_8

Figure 3.28: Comparison between measurements provided by DIC analysis and testing machine.

The post-treatment of the experimental results allows to define the peak loads P_I, P_{II}, P_{III} referred to the end of the three stages which characterize the tensile behaviour of the BFRCM and GFRCM system, the corresponding strain values from DIC analysis (ε_I, ε_{II}, ε_{III}) and the stiffness of each stage

(E_I, E_{II}, E_{III}). More in details, the values of the moduli were calculated considering the tensile stress values refer to the ratio between the applied load and the fibre cross-section (A_f). These data and the corresponding average and COV values are presented in Table 3.15 and Table 3.16 for specimens of group BL_TH and GL_TH , respectively.

Table 3.15: Results from DIC analysis: specimens of BFRCM with lime-based mortar (BL_TH group) in Stage I, II and III.

	Sample ID	P_I [N]	ε_I [%]	E_I [GPa]
STAGE I	BL_TH_1	1243.6	0.05	5889.8
	BL_TH_3	1154.2	0.04	2895.8
	BL_TH_5	1374.4	0.06	1243.2
	BL_TH_6	1442.02	0.08	1200.2
	BL_TH_7	1393.1	0.02	12708.6
	Average	**1321.5**	**0.05**	**2827.2**
	COV	**(8.0%)**	**(45.8%)**	**(55.4%)**
	Sample ID	P_{II} [N]	ε_{II} [%]	E_{II} [GPa]
STAGE II	BL_TH_1	1949.8	1.06	29.8
	BL_TH_3	1647.6	0.85	26.0
	BL_TH_5	2209.6	1.27	29.7
	BL_TH_6	2103.7	1.01	30.5
	BL_TH_7	1712.36	0.85	16.4
	Average	**1924.6**	**1.01**	**26.5**
	COV	**(11.3%)**	**(15.3%)**	**(19.9%)**
	Sample ID	P_{III} [N]	ε_{III} [%]	E_{III} [GPa]
STAGE III	BL_TH_1	3210.9	1.98	58.7
	BL_TH_3	2978.9	1.65	71.7
	BL_TH_5	3028.8	1.75	72.1
	BL_TH_6	2855.0	1.73	44.7
	BL_TH_7	2448.0	1.41	55.8
	Average	**2904.3**	**1.70**	**60.6**
	COV	**(8.8%)**	**(10.7%)**	**(17.1%)**

These outcomes compared with that reported in Table 3.16 for GFRCM with lime-based mortar (GL_TH group), show that although the same mortar type is used, the average force P_I recorded at the end of the Stage I for the two types of specimens is subjected to variations of about the +27.3% compared to GFRCM specimens. This is probably due to the fact that the GFRCM samples have a curing period longer than about 20 days.

A significant scatter of the stiffness values referred to the first stage (E_I) is observed, as well as for the strain values at the end of the linear branch (ε_I). The COV values for ε_I and E_I are 45.8% and 55.4% for the BFRCM

and 56.9% and 63.0% GFRCM specimens. This is probably due to the adopted gripping method, as discussed in the following section. In general, the BFRCM specimens reached an higher maximum load P_{III} compared to the GFRCM specimens. However, the GFRCM specimens achieve an ultimate load higher than the maximum strength reached by the dry fibre textile. This gain in strength could be attributed to an underestimate of the tensile strength of the dry textile or to the effect of the adhesion promoter. In regard to the stiffness of the third branch E_{III}, the average values referred to the two FRCM systems, 60.6 GPa for BFRCM and 45.2 GPa for GFRCM, are lower than the -15.6% and -36.2% compared to the stiffness of the elastic modulus of the corresponding fibre textile. A marked reduction is observed for GFRCM specimens because the good fibre-mortar bond allows the redistribution of the tensile load at the fibre-mortar interface between two consecutive cracks.

Table 3.16: Results from DIC analysis: specimens of GFRCM with lime-based mortar (GL_TH group) in Stage I, II and III.

	Sample ID	P_I [N]	ε_I [%]	E_I [GPa]
STAGE I	GL_TH_1	1921.7	0.08	982.4
	GL_TH_3	1859.5	0.03	2374.4
	GL_TH_6	1961.5	0.03	3694.3
	GL_TH_8	1523.9	0.11	639.1
	Average	**1816.6**	**0.06**	**1922.6**
	COV	**(11.8%)**	**(56.9%)**	**(63.0%)**
	Sample ID	P_{II} [N]	ε_{II} [%]	E_{II} [GPa]
STAGE II	GL_TH_1	2152.9	0.50	23.0
	GL_TH_3	2252.6	0.43	40.7
	GL_TH_6	2076.3	0.17	32.5
	GL_TH_8	-	-	-
	Average	**2160.6**	**0.37**	**32.1**
	COV	**(3.3%)**	**(38.1%)**	**(22.5%)**
	Sample ID	P_{III} [N]	ε_{III} [%]	E_{III} [GPa]
STAGE III	GL_TH_1	2627.9	0.96	42.7
	GL_TH_3	2900.1	1.03	44.6
	GL_TH_6	2472.2	0.52	49.7
	GL_TH_8	2940.06	1.18	43.8
	Average	**2735.1**	**0.92**	**45.2**
	COV	**(7.1%)**	**(27.6%)**	**(6.0%)**

3.2.5 Influence of different gripping methods

As demonstrated by several experimental studies available in the literature [10] [13], the gripping method adopted for tensile tests significantly affects the

mechanical response of the FRCM systems. In this section, the results provided by the two test set-ups (clamping and clevis grip method) for each FRCM system are compared in terms of stress-strain curves (Figure 3.29).

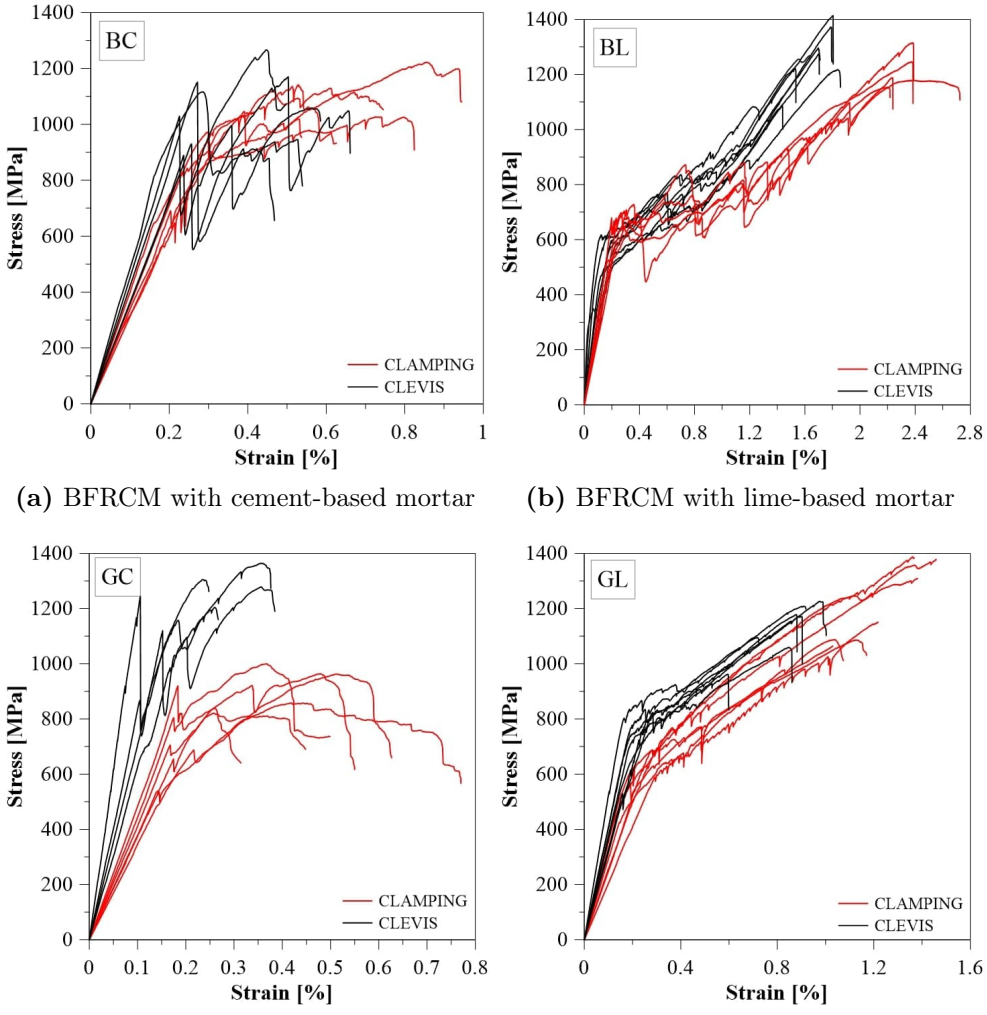

(a) BFRCM with cement-based mortar **(b)** BFRCM with lime-based mortar

(c) GFRCM with cement-based mortar **(d)** GFRCM with lime-based mortar

Figure 3.29: Tensile behaviour with the different test set-ups.

The comparison highlights some differences both in the trend of the curves and in the strength values and corresponding strains at the end of each stage

of the curve. In general, the specimens tested with the clevis grip method (black curves of Figure 3.29) show an average higher stiffness value of the first branch that ranges from the 16.0% for BFRCM with lime-based mortar up to the 42.5% for GFRCM with cement-based mortar (Table 3.17). As well as, the obtained stress values at the transition point σ_I for specimens tested with clamping grip method are lower compared to ones referred to specimens tested with clevis grip method.

These results probably are due to a difference in sample curing period rather than the adopted test set-up method. Tensile tests with clamping grip method are performed after 40 days of curing of the specimens while with clevis grip method after 250 days.

Table 3.17: Average values of the Stage I of the curve for the two test set-up.

Grip method	**Samples**	**Average** σ_I [MPa]	**Average** ε_I [%]	**Average** E_I [GPa]
CLAMPING	BC_TF	784.1	0.25	313.6
	BL_TF	633.4	0.27	234.6
	GC_TF	711.5	0.18	395.3
	GL_TF	614.9	0.25	246.0
CLEVIS	BC_TH	1019.7	0.2	509.9
	BL_TH	530.7	0.19	279.3
	GC_TH	1100.2	0.16	687.6
	GL_TH	706.2	0.2	353.1

The most significant influence of the grip method is observed in the third stage of the curves, especially for BFRCM with lime-based mortar (Figures 3.29(b). The average values referred to the Stage III are summarized in Table 3.18.

The values σ_{III} at the end of Stage III for BFRCM and GFRCM with lime-based mortar are quite close for the two test set-ups. The corresponding strain values ε_{III} when clevis grip method is adopted are always lower compared to the ones of specimens tested with clamping grip method. Consequently, the third stage of the curves referred to specimens tested with the clamping grip method is characterized by a lower stiffness. Stiffness reductions are mainly due to a good fibre-mortar interlooking ensuring by the clamping grip method adopted. While, in the specimens tested with the clevis grip method, the slippage of fibre within the mortar provide the detachment at the interface and the fibre-mortar interaction is lost.

Considering the average values summarized in Table 3.18, the tangent mod-

ulus E_{III} in Stage III for specimen of BFRCM and GFRM with lime-based mortar tested with clevis grip method is quite close to the average value obtained from basalt and glass grid strips, i.e. 1142.2 MPa and 665.4 MPa respectively.

These considerations are useful for the characterization of the FRCM materials. The maximum strength is obviously the main parameter that need to be define, but in a strengthened element not always it is achieved. When the goal is to deduce the design parameters, the possibility to take into account the sliding is necessary, for this reason the clevis system represent a suitable test set-up. However, in the case in which the exploitation of the maximum adhesion properties between fibre and mortar are required the clamping method is a proper alternative solution.

Table 3.18: Average values referred to the Stage III of the curve for the two test set-up.

Grip method	**Samples**	**Average** σ_{III} [MPa]	**Average** ε_{III} [%]	**Average** E_{III} [GPa]
CLAMPING	BC_TF	1108.0	0.65	-
	BL_TF	1216.4	2.32	45.3
	GC_TF	921.0	0.37	-
	GL_TF	1229.8	1.29	59.1
CLEVIS	BC_TH	1152.6	0.33	-
	BL_TH	1268.8	1.68	68.4
	GC_TH	1271.8	0.29	-
	GL_TH	1128.9	0.83	67.1

3.3 Double shear bond test results

In this section the bond properties of the BFRCM and GFRCM systems to calcarenite support are evaluated from double shear bond tests. The scope of this experimental investigation is aimed not only at presenting a comparative performance assessment of different FRCM systems applied on calarenite support, but also at providing meaningful indications for an effective and reliable double shear bond test set-up.

Firstly, the results related to shear bond behaviour of BFRCM and GFRCM systems applied on calcarenite support, through set-up DSB1 are presented in terms of stress-displacement curves. Then, the results from DIC analysis are also discussed in deep. Finally, stress-displacement results from shear bond tests on BFRCM systems to calcarenite support adopting set-up DSB2 and traditional measurement devices are presented and commented.

3.3.1 Results from DSB1 set-up

The outcomes of double shear bond tests adopting DSB1 set-up are presented in terms of stress-displacement curves for the BFRCM and GFRCM systems with cement/lime-based mortar, applied on calcarenite support. The curves reported in Figure 3.30 are referred to data recorded by the testing machine.

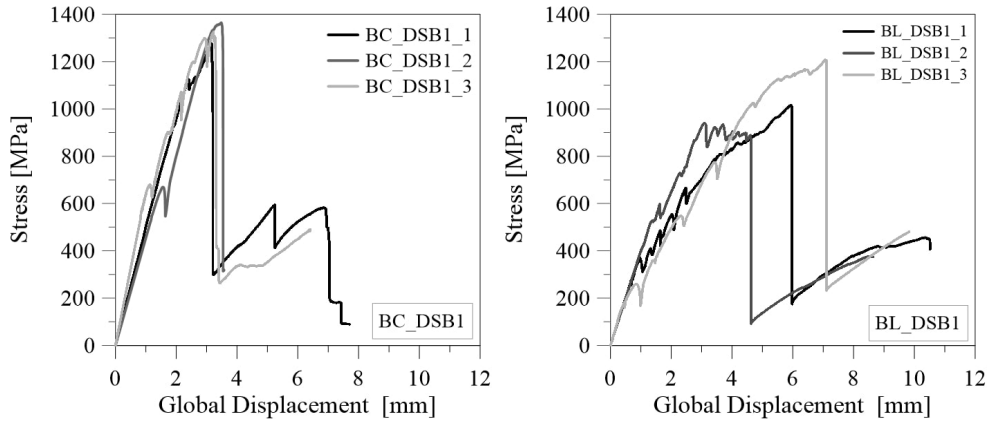

(a) BFRCM with cement-based mortar **(b)** BFRCM with lime-based mortar

(c) GFRCM with cement-based mortar **(d)** GFRCM with lime-based mortar

Figure 3.30: Experimental results from DSB1 set-up: stress-global displacement curves.

In detail, the stress values are derived from data measured by the load cell of the testing machine and the global displacement values are referred to the displacement measurements of the upper block. The displacement is defined as "global" because it included both the slip of the textile with respect to the support and the elongation of the un-bonded fibre strip. The axial stress is obtained as the load divided by the cross-section area of the fibre textile A_f. The peak stress is the maximum stress value attained in the shear bond test, referred to the cross-sectional area of load aligned (longitudinal) fibres.

The results in terms of stress-global displacement relationship, highlight an initial linear branch, followed by a nonlinear phase up to the attainment of the peak stress value. Then a significant load drop is observed due to the tensile failure of the textile (Figures 3.30(a), 3.30(c) and 3.30(d)) or the detachment at the textile-matrix interface (Figure 3.30(b)). Moreover, a residual phase is observed due to the remaining undamaged yarns (for samples of groups: BC_DSB1, GC_DSB1 and GL_DSB1) or the residual tangential stress at the textile-matrix interface due to friction (for samples of group BL_DSB1).

The experimental outcomes along with the average values and the corresponding COV are reported in Table 3.19 for all specimens.

The FRCM systems reached almost the same strength of the bare textile strength, with the only exception of GFRCM with lime-based mortar (samples of group GL_DSB1), where the exploitation ratio of fibre is much lower than one. The exploitation ratios are defined by dividing the peak stress reached during double shear bond tests by the average experimental tensile strength of bare textile, as done for FRCM tensile tests.

It is worth pointing out that the results of double shear bond tests on glass systems (i.e. specimens of group GC_DSB1 and GL_DSB1) are quite different from the tensile tests on the composites. Both specimens of group GC_DSB1 and GL_DSB1 failed by rupture of the fibre grid, however in the tensile tests on composites the exploitation ratio is larger than one, while in the bond tests the exploitation ratio is quite low (about 1 or lower). This is probably due to the un-bonded glass grid is dry, while in tensile tests fibre yarns are impregnated with the adhesion promoter.

Table 3.19 also lists the maximum (peak) stress, the corresponding displacement and the failure mode observed for each test, following the notation according to Recommendation of RILEM Technical Committee 250-CSM [7] (Figure 1.8): A = cohesive debonding in the substrate; C = debonding at the fibre-to-mortar interface; D = textile slippage within the mortar matrix; E1 = tensile rupture of the textile out of the matrix; E2 = tensile failure of the

textile within the matrix. It should be noted that the test uncertainty is much higher in the case of shear bond tests on specimens of group GL_DSB1 where the COV is quite greater: up to about 43.1% for peak stress and 27.8% for corresponding slip. This is mainly related to the accidental load eccentricities due to intrinsic defects on specimens.

Table 3.19: Detailed results of double shear bond tests adopting DSB1 set-up.

Sample ID	**Peak stress** [MPa]	**Peak displacement** [mm]	**Exploitation ratio of fibre**	**Failure mode**
BC_DSB1_1	1274.3	3.17	1.12	E2
BC_DSB1_2	1364.3	3.48	1.19	E1
BC_DSB1_3	1324.5	3.23	1.16	E1
Average	**1321.0**	**3.29**	**1.16**	
COV	**(2.8%)**	**(4.1%)**	**(2.8%)**	
BL_DSB1_1	1015.0	5.94	0.89	D/C
BL_DSB1_2	939.6	3.11	0.82	C/A
BL_DSB1_3	1207.7	7.06	1.06	C/A
Average	**1054.1**	**5.37**	**0.92**	
COV	**(10.7%)**	**(31.0%)**	**(10.7%)**	
GC_DSB1_0	712.9	3.67	1.07	E1
GC_DSB1_2	279.6*	2.43*	0.42*	E1
GC_DSB1_3	558.8	2.69	0.84	E1
Average	**635.9**	**3.18**	**0.96**	
COV	**(12.1%)**	**(15.3%)**	**(12.1%)**	
GL_DSB1_1	394.6	1.17	0.59	E1
GL_DSB1_2	447.8	1.79	0.67	E1
GL_DSB1_3	129.0	0.94	0.19	E1
Average	**323.8**	**1.30**	**0.49**	
COV	**(43.1%)**	**(27.8%)**	**(43.1%)**	

* values excluded from the calculation of the average.

The detachment of the external mortar layer is observed for specimens of BFRCM with lime-based mortar (i.e. group group BL_DSB1). In detail, only in one case (sample BL_DSB1_1), the debonding at the fibre-to-matrix interface (failure mode C) occurs in addiction to the fiber sliding within the matrix (failure mode D) (Figure 3.31). In this case the test is stopped when the total detachment of the upper mortar layer (Figure 3.31(b)) is achieved. For samples BL_DSB1_2 and BL_DSB1_3, the debonding at the fibre-matrix (failure mode C) spreads along a length between 70 and 100 mm (Figure 3.32(a)), then the cohesive debonding in the substrate occurs (failure mode A), as shown in

Figure 3.32(b).

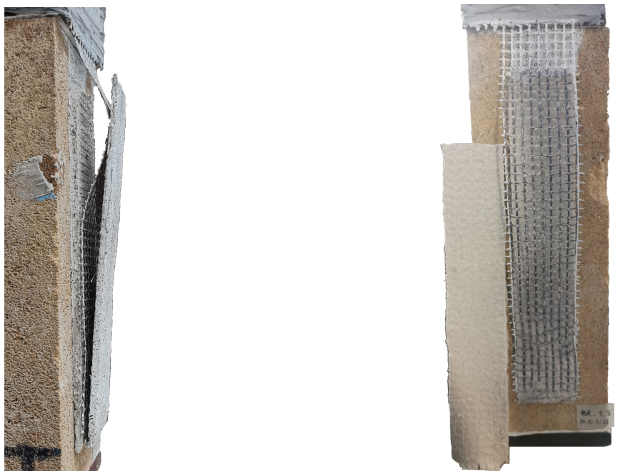

(a) debonding at fibre-matrix interface **(b)** detachment of the mortar layer

Figure 3.31: Observed failure mode C for specimen BL_DSB1_1.

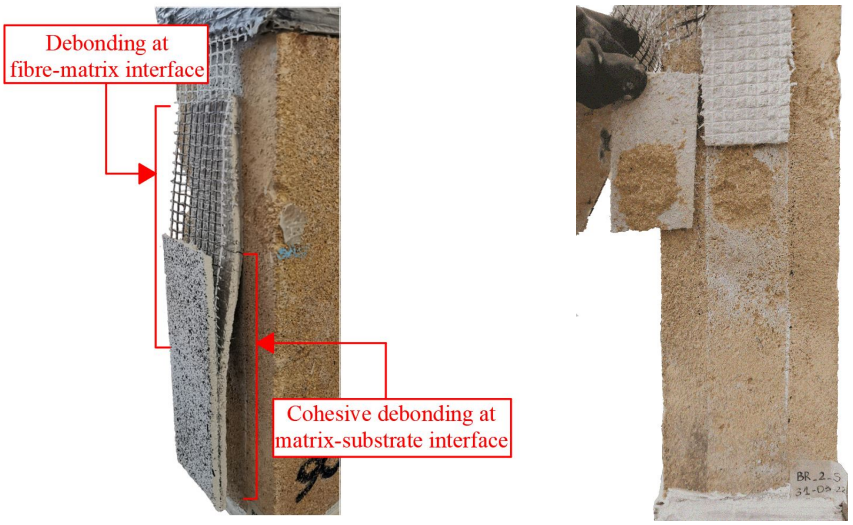

(a) debonding at the fibre-matrix and matrix-substrate interface **(b)** cohesive debonding in the substrate

Figure 3.32: Failure mode C and A for specimens BL_DSB1_2 and BL_DSB1_3.

As expected, the trends of the relative displacements (termed as local slip hereinafter) between the textile and the masonry substrate are quite uniform and allow to exclude significant load eccentricity phenomena during the elastic phase.

Local slips values are measured by the absolute linear displacement transducers that are placed on the two faces of the samples (i.e. front and rear), as shown in Figure 3.33.

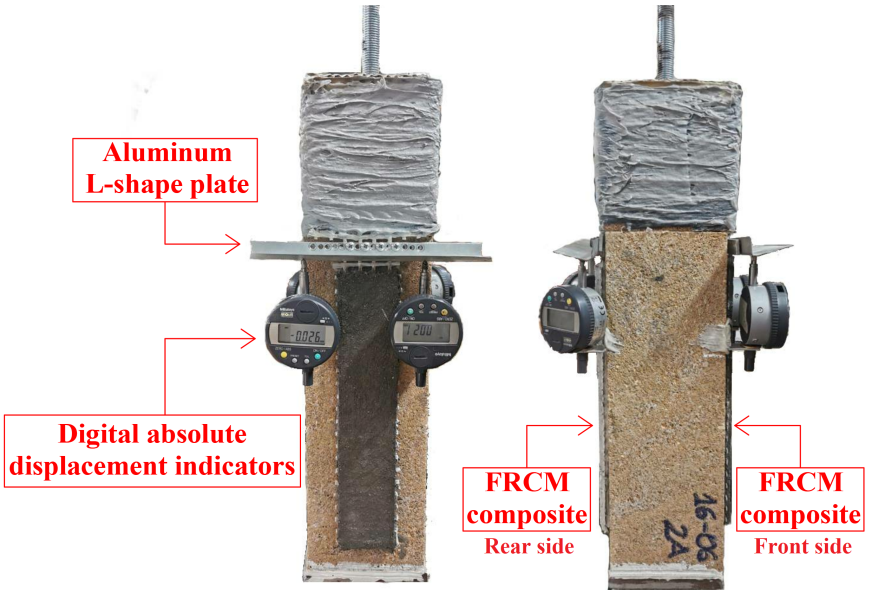

Figure 3.33: Arrangement of the digital absolute displacement indicators on specimens.

The average of measurements from the two absolute displacement transducers located on each faces of the samples are plotted in Figures 3.34.

They are useful in order to identify the the debonding load (P_{deb}). Initially, the absolute displacement transducers do not record local fibre sliding with respect to the support. When the debonding load (P_{deb}) is reached the curves change shape following a quite similar trend, as shown in Figures 3.34.

The aforementioned failure mode A occurs on the two sides of the sample in an almost symmetrical shape. From the outcomes of the absolute displacement transducers, Figure 3.34, it is clear that when the debonding load (P_{deb}) is achieved the perfect bond is lost and the slip profiles assume two different shape.

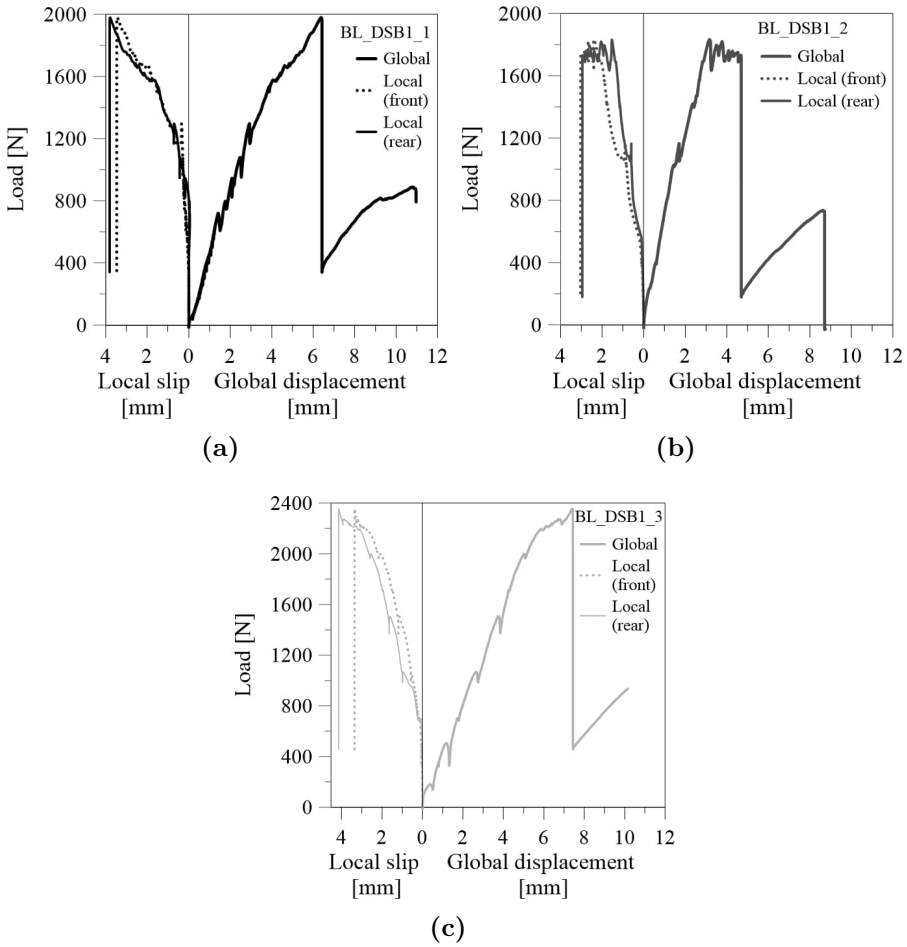

Figure 3.34: Comparison between global displacement and local slip for specimens of group BL_DSB1: **(a)** BL_DSB1_1; **(b)** BL_DSB1_1; **(c)** BL_DSB1_1.

In some cases, during the manufacture of the wrapping system, the unbonded fibre strips were not properly stretched. For this reason, during the loading phase, the load was not uniformly transferred to the two bare fibre strips. This phenomenon was detected by considering the average values of local slip measured by the absolute linear displacement transducers that are placed on the two faces of the samples (i.e. front and rear, Figure 3.33), as in the case of specimens of group GL_DSB1. These results are shown in Figure 3.35 in terms of load-local slip and load-global displacement curves. It is important

to point out that even if the load on each side has not been measured, it was estimated as half of the total load. In this case, the premature rupture in the samples occurs due to the load not being equally distributed between the two faces. Considering the results for specimens of group GL_DSB1, the average exploitation ratio of tensile strength of fibre textile is equal to 0.49%.

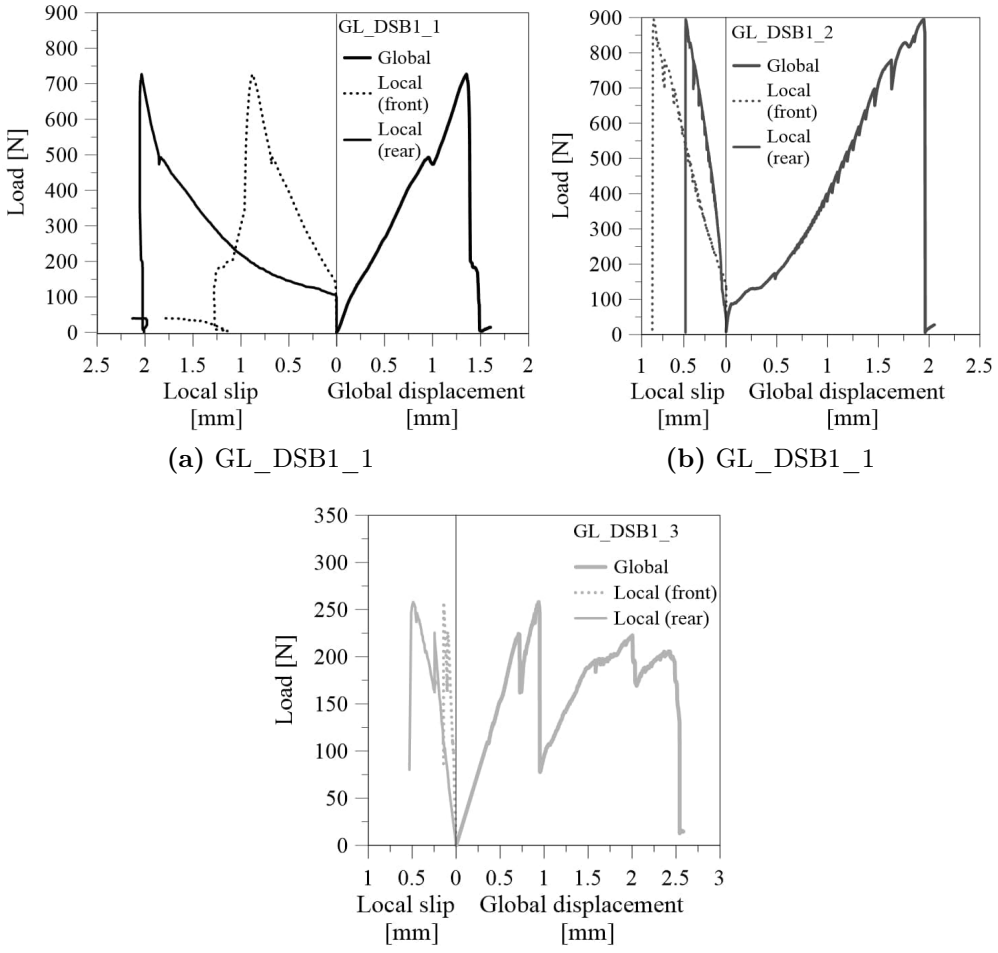

(a) GL_DSB1_1 **(b)** GL_DSB1_1

(c) GL_DSB1_1

Figure 3.35: Comparison between global displacement and local slip for specimens of group GL_DSB1.

As shown in Figure 3.36, the samples of group GL_DSB1 fail due to the

premature fibre textile rupture, without debonding at the interface levels, sliding or cracks formation in the mortar layer. It is a consequence of the stress concentration on a single un-bonded fibre strip due to the eccentricity load distribution, hence the validity of the observed failure mode is compromised and it is not possible to draw final conclusions.

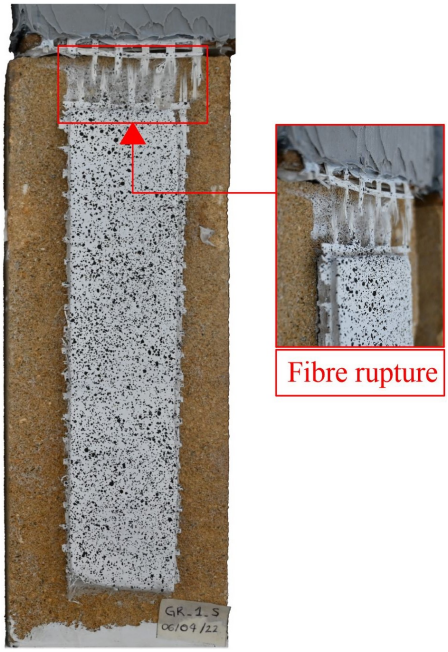

Figure 3.36: Failure mode for specimens of group GL_DSB1: tensile rupture of textile.

It is worth pointing out that the specimen preparation plays an important role on the repeatability of the testing results.

For specimens with cement-based mortar, i.e. group BC_DSB1 and GC_DSB1, the main failure mode is the tensile failure of the textile. Generally, the fibre rupture occurs out of the matrix: in the free un-bonded length for samples of group GC_DSB1, as shown in Figure 3.37(b); near the bonded region at the loaded end, for specimens of set BC_DSB1, as shown in Figure 3.37(a), with the exception of specimen BC_DSB1_1 where, first the debonding at fibre-matrix interface occurs (Figure 3.38(a)), then the telescopic failure of fibre bundles is observed within the matrix (Figure 3.38).

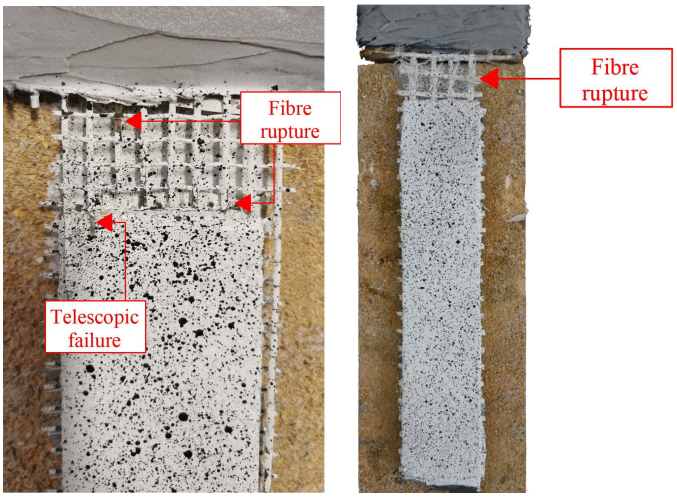

(a) Group BC_DSB1 **(b)** Group GC_DSB1

Figure 3.37: Tensile rupture of textile outside matrix: failure mode E1.

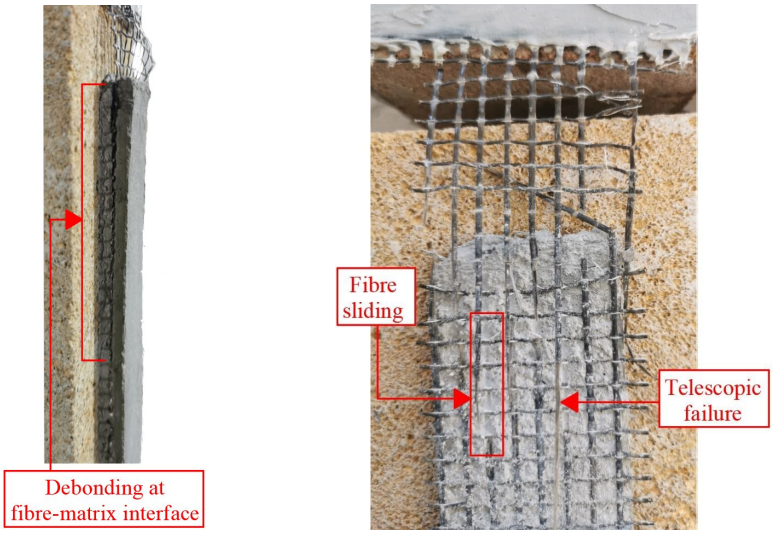

(a) delamination at fibre-matrix interface **(b)** telescopic rupture of fibre bundles

Figure 3.38: Tensile rupture of textile within matrix (failure mode E1): for specimen BC_DSB1_1.

In general, when the bond performance at the fibre-matrix and FRCM-substrate interface is good the scatter is reduced and the failure mode tends to be fibre rupture.

However, it should be pointed out that the tensile rupture of textile outside the matrix observed for specimens BC_DSB1_2 and BC_DSB1_3 (Figure 3.37(a)) is very different from the tensile rupture of textile inside the matrix observed for specimens BC_DSB1_1 (Figure 3.38) and could invalidate the experimental results.

Nevertheless, these two different failure modes observed on three nominally identical specimens can be associated with the inherent variability of FRCM systems and in particular to the hydration of the inorganic matrix which plays an important role in defining the fibre-matrix bond properties.

3.3.2 Results from DIC analysis

The outcomes from the DIC measurements provide the full-field displacement of the upper mortar layer. The distribution of strains along the bonded length, determined from the DIC measurements, for different load stages is presented in the following.

In general, for specimens with cement based mortar a very limited distribution of strains along the bonded length is observed.

The strain pattern evolution along the bonded length for selected points of the load-displacement curve in Figure 3.39 can be observed in Figure 3.40 for specimen BC_DSB1_2.

Differently, in the case of specimens of BFRCM with lime based mortar, where the debonding at the fibre-mortar interface occur, the evolution of strains along the bonded length with the load increment is clearly observed. The strain color pattern is shown in Figure 3.42 for different load stages, selected in the load-displacement curve (Figure 3.41).

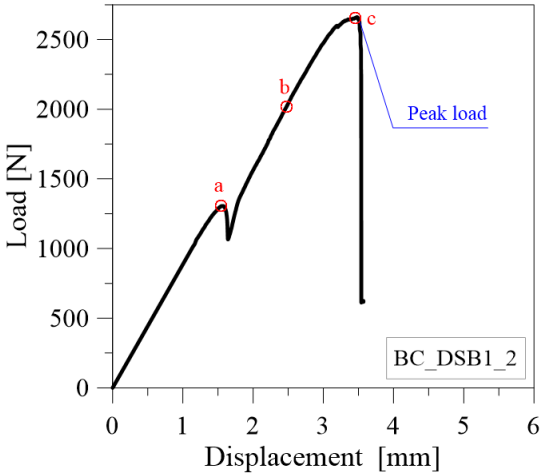

Figure 3.39: Load-displacement curve of specimen BC_DSB1_2 with the characteristic stages.

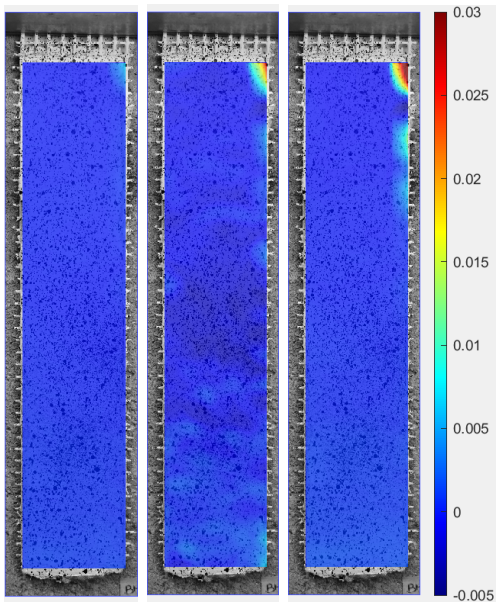

Figure 3.40: Strain pattern evolution for specimen BC_DSB1_2 exported from Ncorr.

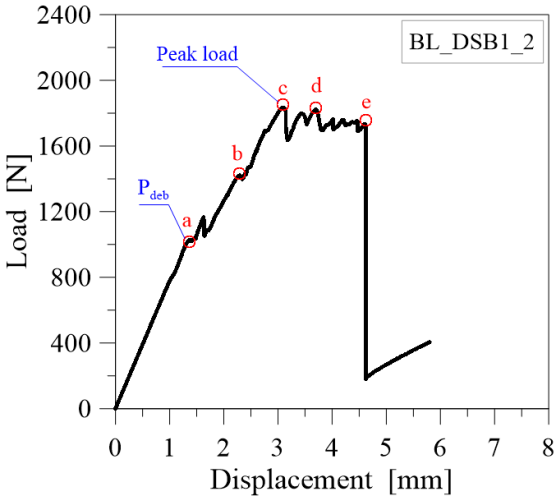

Figure 3.41: Load-displacement curve of specimen BL_DSB1_2 with the characteristic stages.

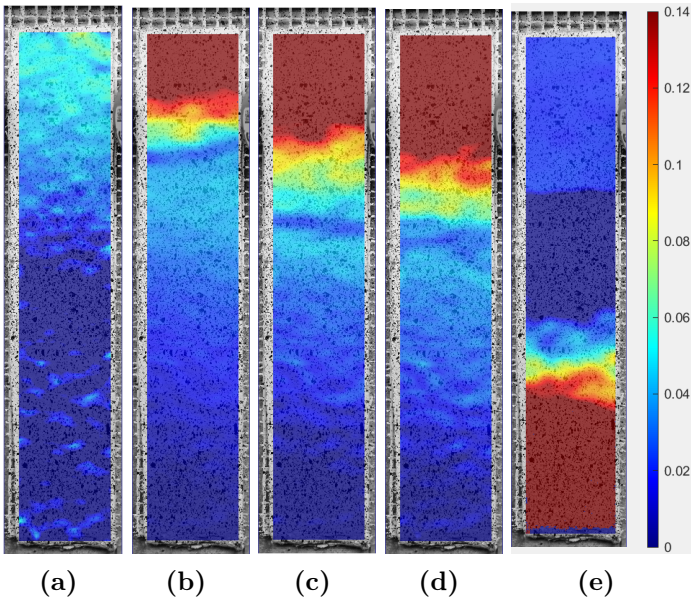

Figure 3.42: Strain pattern evolution for specimen BL_DSB1_2 exported from Ncorr.

It can be observed that for specimen BL_DSB1_2, the strain values develop from the loaded end toward the entire bond length. While, the debonding occurs from point "b". This is clearly observable in the strain profile along the bond length of the specimen, reported for different load stages in Figure 3.43.

When the debonding occur the curve changes the slope, identifying the length of mortar detachment. The observed fluctuations in the strain profiles can be partly attributed to some irregularity on the surface or bond imperfections.

In the specimen BL_DSB1_2 the cohesive debonding in the substrate occurs, this phenomenon is clearly identified. The strain profile became almost constant up to the section where the detachment at the mortar-substrate interface occur.

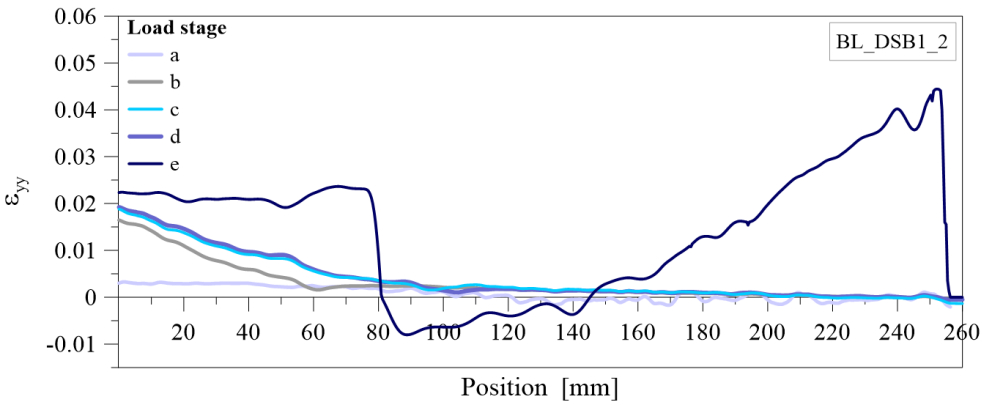

Figure 3.43: Longitudinal strain profiles at different load stages for specimen BL_DSB1_2.

An important parameter that can be obtained from the strain profiles is the effective bond length, defined as the length in which the stresses are fully transferred from the FRCM system to the substrate (i.e. the minimum length to achieve the maximum load carrying capacity). For obtaining the effective bond length, the strain profile (Figure 3.44) at failure is considered: such as for specimen GL_DSB1_2 the failure corresponds to point "c" of the load-displacement curve shown in Figure 3.45).

Initially, the strain values in the mortar are almost zero along the whole bond length as shown in Figure 3.44. Then, from point "b" of the load-displacement curve (Figure 3.45), the strains in the upper mortar layer start to spread from the loaded end (positioned at 0 mm) toward the free end (posi-

tioned at 260 mm), in the so called "stress transfer zone". Finally, at point "c" of the curve, no additional stress is transferred to the mortar and consequently to the substrate. The strain profile corresponding to point "c" (Figure 3.44) of the load-displacement curve (Figure 3.45) allows to identify the stress transfer zone. In this case, a length of about 230 mm may be considered the effective bond length.

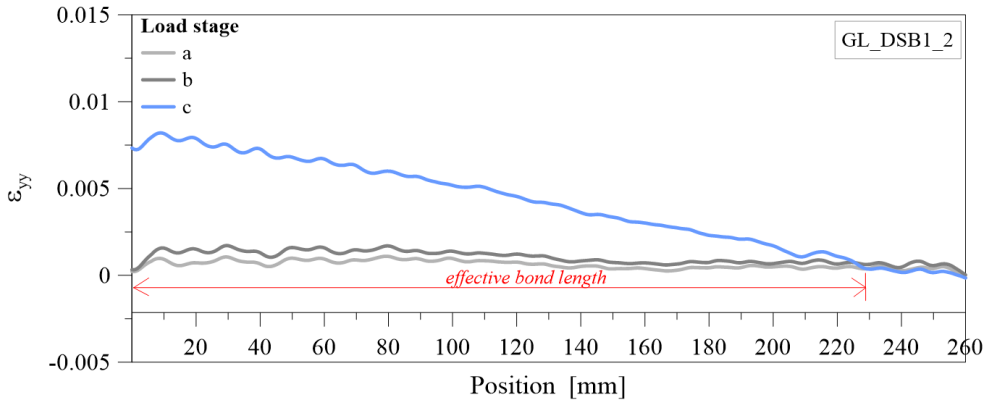

Figure 3.44: Longitudinal strain profiles at different load stages for specimen GL_DSB1_2.

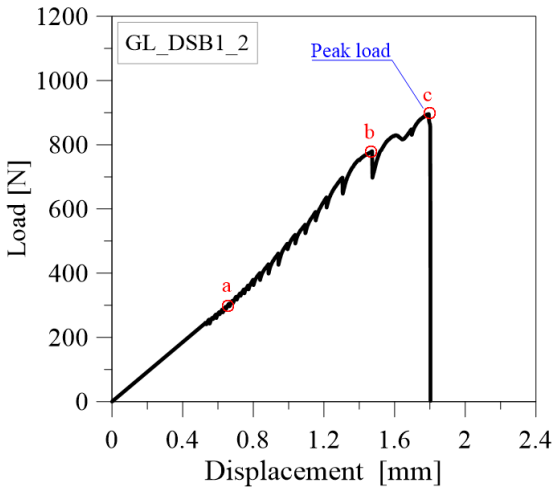

Figure 3.45: Load-displacement curve of specimen GL_DSB1_2 with the characteristic stages.

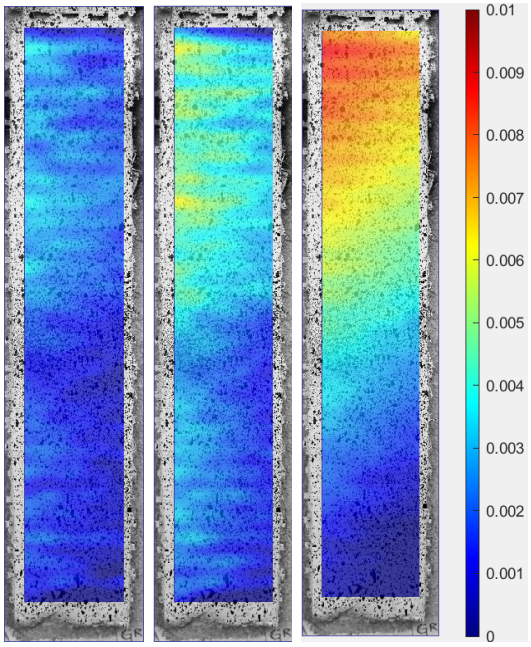

Figure 3.46: Strain pattern evolution for specimen GL_DSB1_2 exported from Ncorr.

3.3.3 Results from DSB2 set-up

Double shear bond tests with DSB2 set-up were carried out with the purpose to evaluate the bond properties on a greater length and width of the bonded area of BFRCM systems applied on calcarenite support.

Results are plotted in terms of stress-global displacement curves, as shown in Figures 3.47.

Moreover, curves in terms of stress- local slip are reported in Figures 3.48.

The local slip values are calculated considering the average measurements of the two digital absolute displacement indicators settled in the front and rear side of samples, in order to record the relative slip between fibre and substrate, and also to give information about eccentricity phenomena.

The experimental outcomes along with the average values and the corresponding COV are reported in Table 3.20 for all specimens.

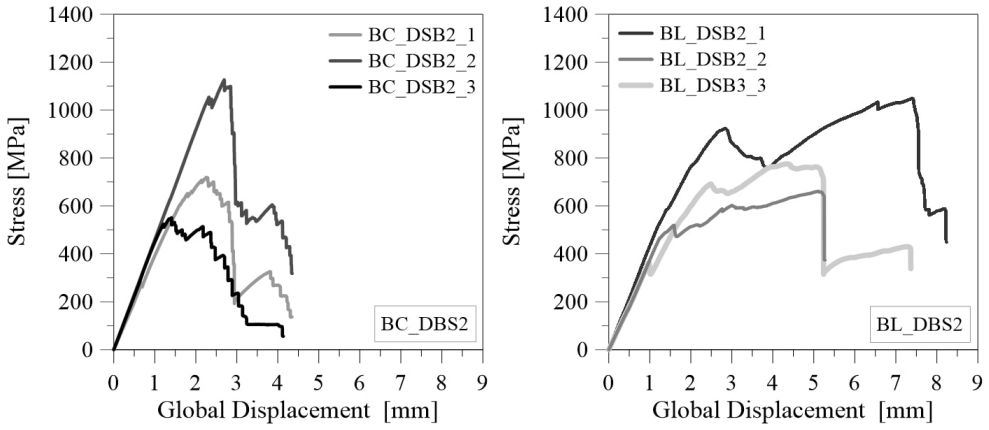

(a) BFRCM with cement-based mortar **(b)** BFRCM with lime-based mortar

Figure 3.47: Experimental results from DSB2 set-up: stress-global displacement curves.

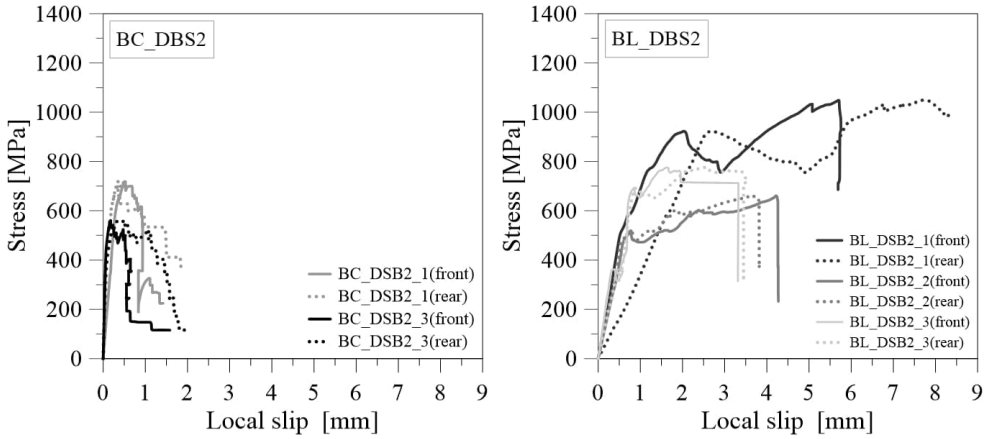

(a) BFRCM with cement-based mortar **(b)** BFRCM with lime-based mortar

Figure 3.48: Experimental outcomes from digital absolute displacement indicators, stress-local slip curves.

Table 3.20: Detailed results of double shear bond tests adopting DSB2 set-up.

Sample ID	**Peak stress** [MPa]	**Peak slip** [mm]	**Exploitation ratio of fibre**	**Failure mode**
BC_DSB2_1	719.2	2.25	0.63	E1
BC_DSB2_2	1126.7	2.69	0.99	E1
BC_DSB2_3	550.7	1.41	0.48	E1
Average	**798.9**	**2.12**	**0.70**	
COV	**(30.3%)**	**(25.1%)**	**(30.3%)**	
BL_DSB2_1	1048.8	7.40	0.92	C
BL_DSB2_2	661.3	5.11	0.58	C
BL_DSB2_3	775.9	4.34	0.68	C
Average	**828.7**	**5.62**	**0.73**	
COV	**(19.6%)**	**(23.1%)**	**(19.6%)**	

*values excluded from the calculation of the average.

A different global behaviour is observed from the comparison of the experimental curves related to the two groups of samples (BC_DSB2 and BL_DSB2).

Cement-based mortar has established a good adhesion with basalt fibre textile, for this reason experimental curves of BC_DSB2 group show a linear elastic behaviour up to the maximum fibre strength, followed by a limited post-peak phase.

The observed failure mode is governed by the fibre rupture in the un-bonded length (failure mode E1), as shown in Figure 3.49.

Figure 3.49: Observed failure mode E1 for specimens of group BC_DSB2.

Despite the great scatter observed for samples of BC_DSB2 group (average COV of 30.3% and 25.1% for peak stress and corresponding slip, respectively), data recorded by the digital absolute displacement indicators (Figure 3.48(a)) confirm that no eccentricity phenomena occur in the samples, so the variability of results is probably due to some defects in the fibre strips.

Samples of BL_DSB2 group (Figure 3.47(b)) highlight a different global behaviour characterized by a first linear branch up to reach the load of debonding P_{deb}. Then, the delamination of the upper mortar layer spreads from the loaded end to the entire bond length causing the total slip of the fibre textile, as shown in Figure 3.50.

Also, in this case negligible eccentricity phenomena are observed, with the exception of sample BL_DSB2_1, where the trend of local slips measured in the rear side (dash line) assumes a lower initial stiffness (Figure 3.48(b)).

Figure 3.50: Observed failure mode C for specimens of group BL_DSB2.

3.3.4 Comparison between the two test set-ups

The effect of the bond length and width is investigated for specimens of BFRCM with cement (BC) and lime-based (BL) mortar.

In details, for the first proposed set-up DSB1 the bond length is assumed equal to 260 mm and the bond width equal to 50 mm. The assumption of these dimensions of the bonded FRCM strip implies a small size of the sample, promoting a simple and manageable configuration of the test set-up.

A greater bond length (320 mm) and width (100 mm) of the FRCM strip implies a larger sample size and consequently a less easy set-up (DSB2).

The comparisons of stress-displacement curves for BFRCM strips bonded on calcarenite masonry substrate, according to the two test set-ups (DSB1 and DSB2), are plotted in Figure 3.51. The slopes of the curves are quite close. However, some inconsistency between the two test set-up is observed.

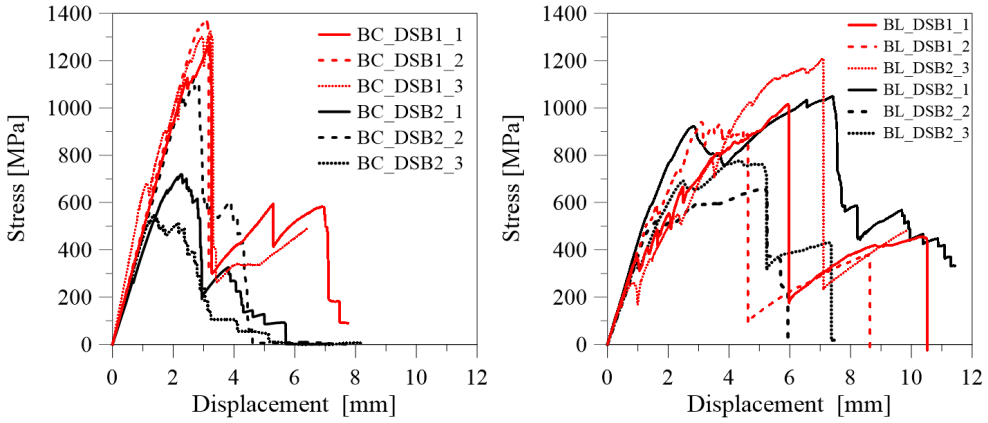

(a) BFRCM with cement-based mortar **(b)** BFRCM with lime-based mortar

Figure 3.51: Comparison of stress-displacement curves from the two test set-up methods (DSB1 and DSB2).

The experimental outcomes from the two test set-ups are compared in terms of ultimate capacity and failure modes in order to assess the repeatability of the results and the influence of the selected variables. In Table 3.21 the main values are listed: the peak stress and the corresponding displacement value, the exploitation ratios related to the average experimental tensile strength of basalt bare textile (vs. fibre) and the maximum strength of the FRCM system. This last is evaluated considered the average of σ_{III} from tensile test on BFRCM

with cement and lime-based mortar adopting both clamping and the clevis grip method. This is mainly related to the limited variation of the two data, about the 2%.

From the data presented in Table 3.21, it is clear that the uncertainty is much higher in the case of bond tests performed on BFRCM with cement-based mortar (BC) adopting set-up DSB2. In this case the COV is quite higher up to about 30%. Only specimen BC_DSB2_2 show a trend quite close the curves referred to specimen tested with DSB1 set-up (red curves of Figure 3.51(a)) for which a low scatter is observed.

The cement-based mortar achieves chemical compatibility and good adhesive features in respect to the calcarenite substrate, for this reason the observed failure mode for BFRCM with cement-based mortar is the fibre rupture (failure mode E1) both for set-up DSB1 and DSB2. The exploitation ratio with respect to the tensile strength of bare textile is expected should tend to the unity. However, for specimen tested with set-up DSB2 this exploitation ratios are lower than one, and the coefficient of variation is high. It is mainly due to the effect of bond test set-up yielding to underestimation of the bond strength. The eccentricity driven by the different composite size is probably the main cause of scatter of peak load. Since, the difficulty to guarantee a uniform load distribution among a larger number of longitudinal yarns is combined to the possible presence of more defects on a wider un-bonded fibre strip.

Further differences are observed when fibre slippage and debonding at the fibre-mortar interface occur (Figure 3.51(b)). The specimens of BFRCM with lime-based mortar show about the same initial stiffness in the first linear branch, followed by a non linear phase characterized by a significant scatter. In this case, the exploitation ratios with respect to the tensile strength of the bare textile and FRCM composite is lower than one. This is related to the higher degree of complexity of the fibre-mortar interaction.

In two cases, BL_DSB1_2 and BL_DSB1_3, the debonding at the mortar-to- support interface following by the cohesive rupture of the substrate is observed. From the observed failure mode A, it can be inferred that a bond length of 260 mm is insufficient for the exploitation of the fibre tensile strength.

Table 3.21: Results of shear bond tests referred to the two test set-ups: DSB1 and DSB2.

Test set-up	**FRCM system**	**Peak stress** [MPa]	**Peak slip** [mm]	**Exploitation ratio vs. fibre**	**Exploitation ratio vs. tesile test**	**Failure mode**
DSB1	BC	1274.3	3.17	1.12	1.13	E2
		1364.3	3.48	1.19	1.21	E1
		1324.5	3.23	1.16	1.17	E1
	Average	**1321.0**	**3.29**	**1.16**	**1.17**	
	COV	**(2.8%)**	**(4.1%)**	**(2.8%)**	**(2.8%)**	
DSB2	BC	719.2	2.25	0.63	0.64	E1
		1126.7	2.70	0.99	1.00	E1
		550.7	1.41	0.48	0.49	E1
	Average	**798.9**	**2.12**	**0.70**	**0.71**	
	COV	**(30.3%)**	**(25.1%)**	**(30.3%)**	**(30.3%)**	
DSB1	BL	1015.0	5.94	0.89	0.82	D/C
		939.6	3.11	0.82	0.76	C/A
		1207.7	7.06	1.06	0.97	C/A
	Average	**1054.1**	**5.37**	**0.92**	**0.85**	
	COV	**(10.7%)**	**31.0%)**	**(10.7%)**	**(10.7%)**	
DSB2	BL	1048.8	7.40	0.92	0.84	C
		661.3	5.11	0.58	0.53	C
		775.9	4.34	0.68	0.62	C
	Average	**828.7**	**5.62**	**0.73**	**0.67**	
	COV	**(19.6%)**	**23.1%)**	**(19.6%)**	**(19.6%)**	

In general, a lower scatter is observed for specimens tested with set-up DSB1. It provides to transfer two balanced tensile force to the two FRCM strips, without including compressive stress on the support resulting from the reaction of the steel frame used to constrain the prismatic block, as well as for DSB2 set-up. Moreover, these results are in accordance with the performance and the failure modes (i.e. tensile failure of fibre for BFRCM with cement-based mortar and debonding at the fibre-mortar interface for BFRCM with lime-based mortar) observed from tensile tests on the corresponding FRCM coupons.

Chapter 4

Numerical investigation

This chapter shows the development of two proposed numerical models which are developed to simulate respectively the tensile and shear bond behavior of FRCM composites. Both models take advantage of truss and non-linear spring elements to simulate the material components and the interface. The implementation is made through OpenseesPy [66], that is the Python interpreter of the Finite Element (FE) framework OpenSees [67].

The results shows that the models are able to reproduce the crack development in mortar, the friction and the slippage between fabric and mortar. Additionally, they provide the global mechanical response in terms of load-strain or load-slip relations. The accuracy of proposed models is validated against results of the experimental campaign presented in previous chapters.

4.1 Proposed numerical model for the tensile behaviour

The proposed model for simulating the behaviour of FRCM in tension employs truss elements for modelling the material constituents - i.e. fabric and matrix - while shear spring elements are introduced in order to simulate the fabric-to-matrix interaction. The model and the hypotheses made are studied to reproduce the behaviour of a FRCM sample subjected to tensile tests with a clamping test set-up, and the following assumptions are here made:

- (1) geometrical imperfections are neglected (i.e. the FRCM strip has a straight axis);
- (2) both phases behave only in pure tension;
- (3) the first crack opens at the member's ends;

- (4) the fabric-to-matrix interface can transfer pure shear stress.

On the basis of these hypotheses, the model is defined only along the FRCM strip's axis, and therefore it can be defined as an uniaxial model loaded at the free fibre ends, as depicted in Figure 4.1.

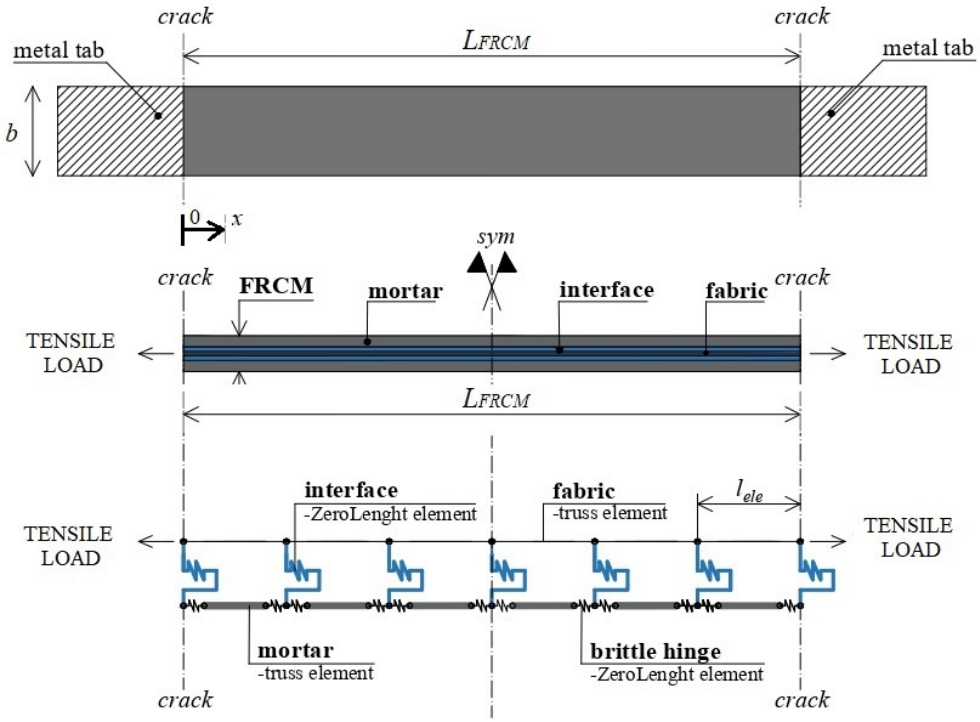

Figure 4.1: 1D numerical models for tensile behaviour.

In particular, two sets of trusses are considered, one for modelling the mortar and one for modelling the fabric. The groups of trusses modelling the mortar are connected to the row of fabric trusses through shear springs, for modelling the interface interaction.

Additionally, axial spring elements are also added in series at the ends of each matrix truss. These springs, called "brittle hinges", are introduced in order to simulate crack opening in the mortar.

The two series of truss elements are defined by their cross-sectional area, A_f for the fiber and A_m for the matrix. These last are assumed equal to

the nominal thickness for the mortar, while the conventional dry fiber cross section is assumed for the fabric. As stated by assumption no.(3), the model is generated under the hypothesis that the first cracks appear at the extremities of the FRCM strip, close the gripping area, as observed in several experimental studies. In this case, when the first cracking occurs, the tensile load is applied entirely to the fabric, and it is transferred to the mortar through the fabric-to-mortar interface (see assumption (4)). In the proposed model, the gripping area and tabs are not modelled and the system is loaded through the application of a displacement history at the free fibre end. For this reason, only the free length, namely L_{FRCM}, is considered in this model and it is discretized in a certain number of elements adequate to simulate the number of cracks.

Furthermore, the model takes advantage of the symmetry condition, so it is possible to study the half of the sample, fixing the degrees of freedom of the nodes at the center symmetry axis. The boundaries condition in the OpenSeesPy framework [66] are implemented using pinned support applied to these nodes.

The developed model requires easily only the definition of uniaxial material laws, and the assumptions made in the current study are resumed in Figure 4.2.

The materials adopted in the model for matrix and fibre are assumed to be elastic with a pure brittle constitutive law. In particular, the fabric is assumed to react only in tension with elastic modulus E_f and ultimate tensile strain ε_{fu}. Mortar is assumed working linear elastically in tension with elastic modulus E_m and tensile strength is labelled as $f_{m,t}$. This last is assumed equal to the 50% of the flexural strength.

It should be noted that in absence of detailed indications, the elastic modulus of the mortar is here calculated according to the following expression proposed in the Italian Code NTC18 [68] for the concrete in compression:

$$E_m = 22000 \left(\frac{f_{m,c}}{10} \right)^{\frac{1}{3}} \tag{4.1}$$

being $f_{m,c}$ the compressive strength of the mortar. This assumption is certainly a simplification (i.e. the elastic modulus of the mortar in tension is assumed equal to that in compression), but it can be accepted for low values of the tensile stress.

Brittle hinges are modelled as rigid elements, just by assigning the maximum stress $f_{h,t}$ equal to the cracking strength of the mortar $f_{m,t}$ in order to simulate the crack formation.

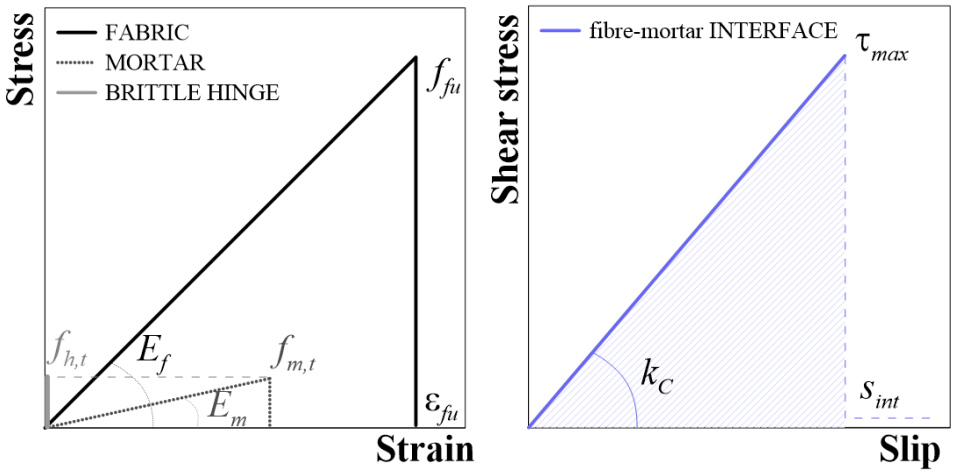

(a) stress-strain laws assumed for fabric, mortar and brittle hinges

(b) Shear stress-slip law assumed for fibre-mortar interface

Figure 4.2: Uniaxial material laws assumed in the model.

The interface is then defined with the introduction of discrete shear springs with a linear elastic shear force-slip relation. This law is defined by the stiffness $K_{D,fm}$ and the maximum force. The discrete value of the stiffness $K_{D,fm}$ is deduced from the continuous value $k_{C,fm}$, which is the slope of the first branch of the shear stress vs. slip law assumed at the interface. The relation between $K_{D,sm}$ and $k_{C,fm}$ is obtained by assuming that the shear stress is constant along two successive springs. Under this assumption, if the shear stress is integrated, the following relation holds:

$$K_{D,fm} = k_{C,fm} b \frac{L_{FRCM}}{n} \tag{4.2}$$

being b the width of the sample and n the number of nodes assumed in the model.

A maximum slip is also attributed to the interface as a function of the maximum value of the shear stress τ_{max}.

$$s_{int} = \frac{\tau_{max}}{k_{C,fm}} \tag{4.3}$$

The values of $k_{C,fm}$ and τ_{max} are calibrated on the basis of the experimental results in order to obtain a readable response curve consistent with the

expected result. The number of nodes n is obtained by a mesh sensitivity test, as discussed below. It is worth noting that the assumption of linear pure-brittle behaviour of the interface is an approximation, due to the fact that a more reliable law should include a softening branch of the shear stress-slip law and a limited residual stress. In this last case, the definition of the law requires the calibration of two further parameters (i.e. the slope of the softening branch and the residual stress) and it becomes more difficult to define. It is also observed that despite the simplification, the assumption of brittle linear behaviour was already adopted in the literature [69] and it was demonstrated that it can be accepted with good approximation.

4.1.1 Implementation and analysis settings

As discussed above, the model is formulated to work along one direction -i.e. 1D model-, which means that all the nodes have the same Y-coordinate, assumed equal to 0 in the current implementation, and therefore it is all defined along a line.

All the geometric nodes are implemented using a *for loop* dividing the model as a ratio of specimen length on nodes number. During this phase nodes object are initialized, the connectivity of the elements is generated and the tags are assigned. All the trusses are introduced by means of *Truss* elements, while *ZeroLength* elements are introduced in order to connect the extremities of mortar elements (by brittle hinges) and modelled the interface, connecting the nodes of the matrix elements with those of the fabric.

Despite the computational power of the OpenSees framework [67], the model implementation could be tricky, due to the fact that the model script needs to be coded. For this reason Python v3.8 environment [70] is used for the model implementation, using also numpy [71] and matplotlib [72] libraries for data analysis and plotting. Due to the complex model discretization, some classes are introduced for a better implementation of nodes and elements object's, and each one of them is identified between string tags. The implemented classes also includes some methods using OpenSeesPy recorders to retrieve the output data at each step of the analysis.

A non-linear static analysis is executed under displacement control where an axial displacement, applied to the rightmost fiber node, is increased until it reaches the target displacement, and using the Newton-Raphson algorithm for the solution of the non-linear system of equations. For each steps of the analysis the output results are stored inside each node and element objects,

in terms of displacements and reaction forces, to simplify the post-processing analysis for both global and local response.

4.1.2 Results

The proposed model is adopted to predict the results of the experimental investigation on FRCM coupons tested with clamping grip method and presented in Chapter 2.

The main geometric and mechanical properties adopted in the model are summarized in Table 4.1 and 4.2, respectively.

Table 4.1: Geometric characteristics of the samples.

SAMPLE ID	GEOMETRY			
	t_m [mm]	t_f [mm]	b [mm]	L_{FRCM} [mm]
BC_TF	10	0.039	50	200
BL_TF	10	0.039	50	200
GC_TF	10	0.04	50	200
GC_TF	10	0.04	50	200

Table 4.2: Mechanical properties assumed in the model.

SAMPLE ID	MORTAR		FIBRE			INTERFACE	
	$f_{m,t}$ [MPa]	E_m [GPa]	f_{fu} [MPa]	E_f [GPa]	ε_{fu} [%]	$k_{C,fm}$ [N/mm^3]	τ_{max} [MPa]
BC_TF	3.30	35.2	1142.2	71.8	1.59	4.50	1.00
BL_TF	3.13	25.7	1142.2	71.8	1.59	2.50	0.60
GC_TF	3.10	33.8	665.4	70.8	1.1	4.50	1.00
GC_TF	2.13	26.9	665.4	70.8	1.1	3.00	0.68

The values of tensile strength of mortar $f_{m,t}$ are assumed equal to the 50% of the flexural strength values $f_{m,f}$ experimentally evaluated for each sample group.

The number of nodes to be used for the discretization is evaluated according to the size of the sample to be simulated by performing a mesh sensitivity test. A variation of the response is noted as a function of the number of nodes n. This parameter, which is used to define the mesh of the model and therefore the number of elements, affect the definition of the elastic-brittle behaviour attributed to the tangential interface springs.

Figure 4.3 shows the results of the mesh sensitivity analysis.

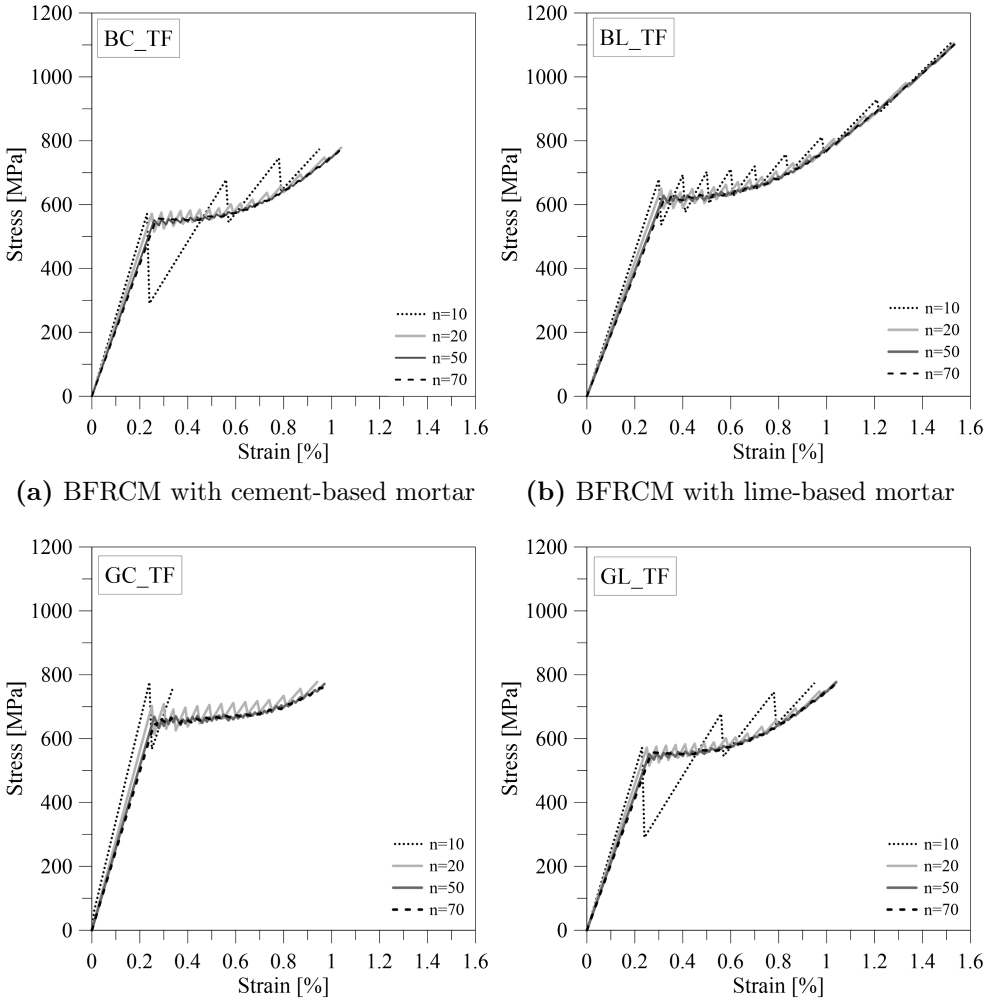

(a) BFRCM with cement-based mortar **(b)** BFRCM with lime-based mortar

(c) GFRCM with cement-based mortar **(d)** GFRCM with lime-based mortar

Figure 4.3: Sensitivity analysis of mesh size.

The variation of n, as observed, produces modifications to the response of the model, which are more or less evident. Figures 4.3(a) - 4.3(d) show the effects of the variation of the number of nodes on the load-strain curves.

The load-strain curves are characterized by significant load drops when a larger mesh of 10 mm (corresponding to a number of elements equal to n=10) is assumed. Moreover, problems of convergence of the analysis arise in the case

of model GC_TF. As shown in Figure 4.3(c), the analysis fails after the first crack opening, because the localization of failure in a mortar section causes the loss of interaction between fibre and mortar elements in the remaining part of the model. Increasing the number of elements (from n=10 up to n=70) the curves assume a more smooth trend and leads to a refined response of numerical analyses.

Mesh size influences numerical accuracy as well as the computation time. Therefore, on the base of the computation cost of simulation and lower deviation in results, a mesh size of 5 mm (corresponding to n=20) is chosen for the analysis.

The numerical outcomes in terms of global stress-strain curves are compared with the enveloped experimental results in the following Figure 4.4.

The best result is obtained from model BL_TF, as shown in Figure 4.4(b). The numerical curve shows a behaviour which may be approximately considered similar to the experimentally observed tri-linear trend, characterized by different slopes.

The model is able to predict the first cracking strength at the end of Stage I and simulate the cracks opening in the mortar during Stage II, which is characterized by several vertical drops in load bearing capacity. This response is mainly related to the stress-strain relationship adopted for fibre-mortar interface ruled by an elastic purely brittle law. When the maximum shear stress value at the interface is achieved, the fibre-mortar interlooking is lost and only the fabric carries the load, therefore, the slope of the curve reflects the elastic modulus of the dry fibre textile. Experimentally a lower slope of the Stage III is observed, this is attributed to a contribution of the un-cracked matrix between the cracks that is neglected in the numerical model.

An almost bi-linear trend is observed for model GL_TF (Figure 4.4(d)). In this case the numerical model underestimates the experimental response in the post cracking stage of about the 26%. As shown in Figure 4.4(d), the model well reproduces the first stage, but fails for values of stress and strain lower than the experimental ones. This mismatch is probably due to some improvement in the mechanical properties of the fibre layer as a consequence of the use of the adhesion promoter or some uncertainty in the experimental assessment of the fibre tensile strength.

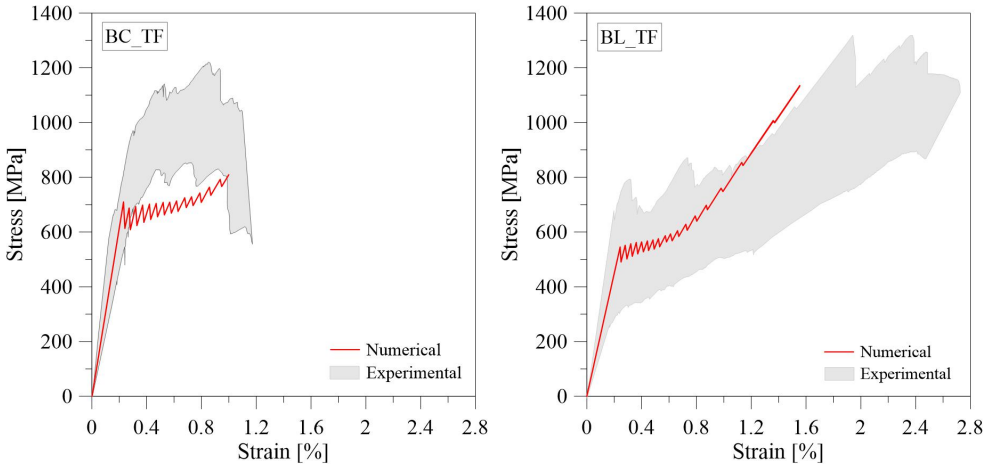

(a) BFRCM with cement-based mortar **(b)** BFRCM with lime-based mortar

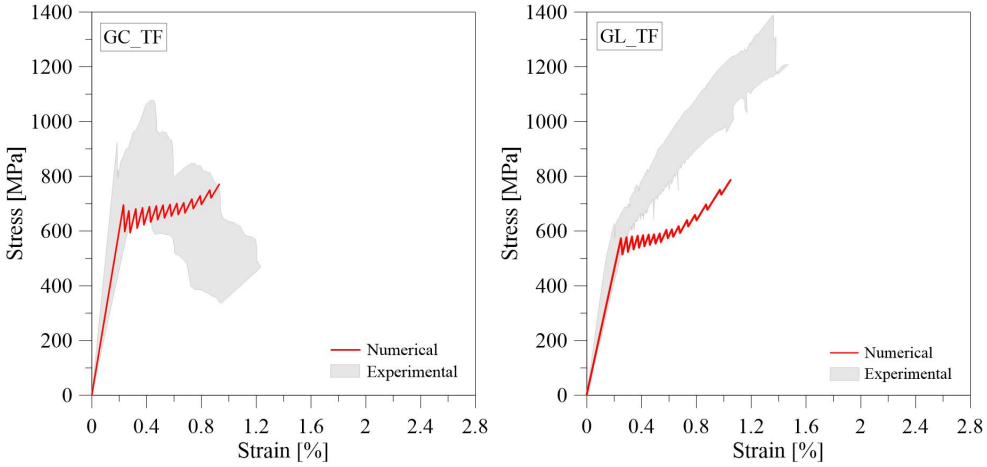

(c) GFRCM with cement-based mortar **(d)** GFRCM with lime-based mortar

Figure 4.4: Comparison between experimental and numerical results: stress-strain curves.

As shown in the Figure 4.5, the model reproduces the observed experimental trend, just assigning to the fabric layer the mechanical properties reported in the technical data sheet provided by supplier: tensile strength equal to f_{fu}=1400 MPa, Young's modulus of E_f=74 GPa and maximum strain of ε_{fu}=2%.

The numerical curve fits the experimental trend, specially the slope of the

third branch, predicting with good approximation the first cracking stress value at the end of Stage I of the curve and the maximum strength at the end of Stage III corresponding to the failure. However, the model provides an unexpected Stage II, not observed experimentally.

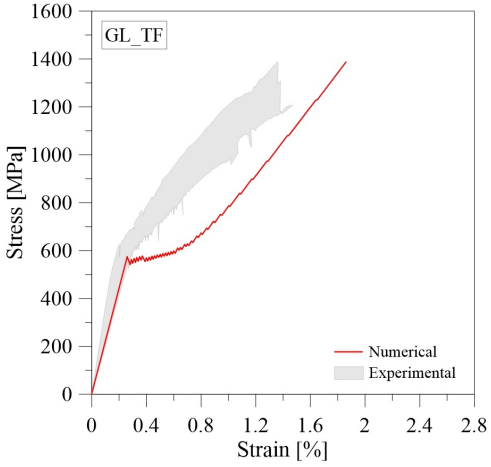

Figure 4.5: Numerical-experimental comparison for model GL_TF: mechanical properties of fabric referred to technical date sheet.

Moreover, the role played by the mechanical percentage of fibre reinforcement becomes quite clear when the numerical response of model BC_TF and GC_TF is considered (Figures 4.4(a) and 4.4(c)). The models are able to simulate the first linear branch (stage I) of the curve, but when the first cracking load is achieved the load keeps almost constant until the failure without the exploitation of the typical tri-linear trend.

The model is very simple, it allows to simulate with good agreement Stage I and Stage II (if it is present). However, the proposed model shows some limitations in the prediction of the third phase. This is probably related to the assumption of a too simplify constitutive law for fibre-mortar interface. The post-peak softening branch for fibre-mortar interface is very important to evaluate the contribution of the residual fibre-mortar interlooking on the cracking behaviour of composite systems. It is clear that the best choice would be to introduce a linear softening constitutive law for fibre-mortar interface, but it implies the need to calibrate a further unknown parameter. However, this simplification is consistent with the literature [73] therefore it is accepted, postponing to future developments.

4.2 Proposed numerical model for the bond behaviour

The modelling approach discussed above for tensile behaviour is extended to the case of shear bond behaviour, taking into account the presence of the possible mortar-to-substrate interaction. The model is schematized in Figure 4.6. In this case, the two mortar layers are modelled separately - i.e. upper mortar layer and lower mortar layer - and for each interface level (mortar-to-fabric and mortar-to-support) a specific constitutive law is assumed.

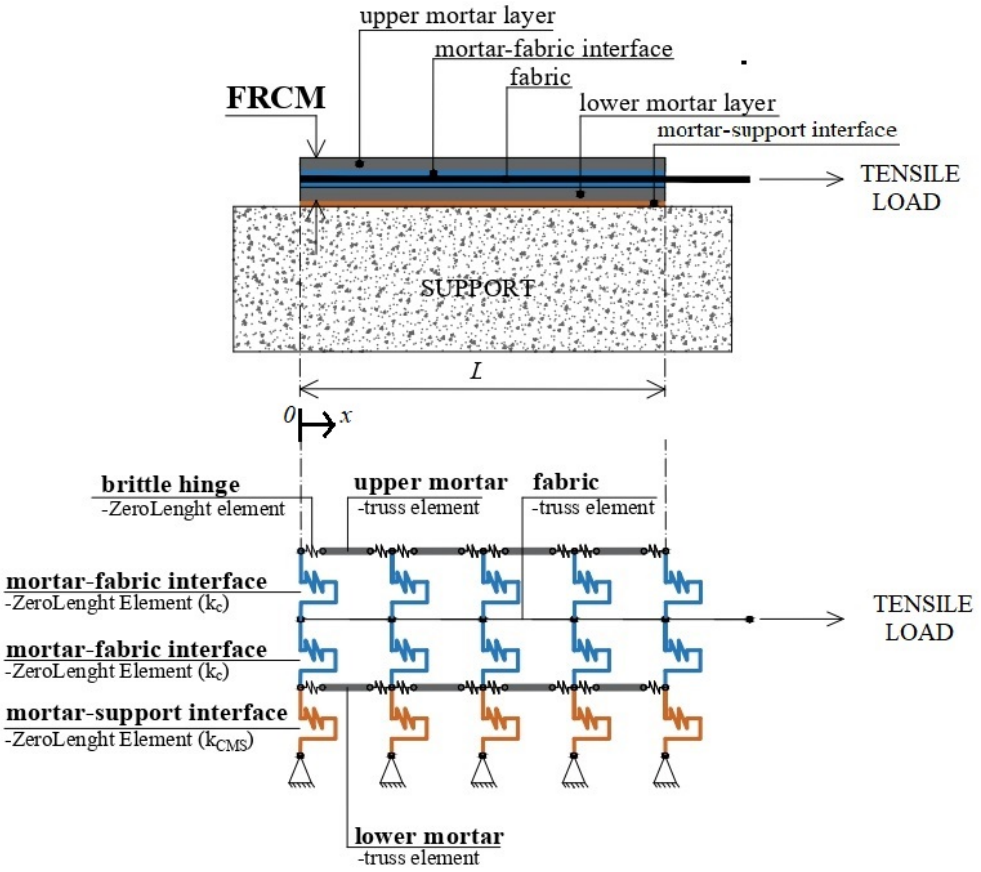

Figure 4.6: 1d numerical models for shear bond behaviour.

The FRCM strengthening system is modelled by means three rows of truss elements, of which two for mortar and one for fabric, connected to each other by linear shear springs. Under the assumption that the substrate is infinitely rigid

and properly constrained, the lower mortar layer is connected to constrained nodes through shear springs simulating the reaction of the support.

Also in this case, uniaxial material laws are assumed both for fabric and mortar truss elements, just assigning the elastic modulus (E_f and and E_m) and the corresponding ultimate strain. Two rows of discrete shear springs simulate the upper/lower mortar-fabric interface. These are characterized by the assumption of mechanical properties (i.e. $k_{C,fm}$ and τ_{max}) previously calibrated for tensile behaviour.

A further order of shear springs is introduced in order to take into account the interaction between the lower mortar layer and the substrate. For the sake of simplicity, a linear-elastic behaviour is assumed for mortar-substrate interface. The assigned law is defined by the discrete value of stiffness $K_{D,ms}$ obtained by multiplying the continuous value $k_{C,ms}$ by the bond area comprises between two successive shear springs at the mortar-support interface.

$$K_{D,ms} = k_{C,ms} B \frac{L}{n} \tag{4.4}$$

being B and L the width and length of the bonded FRCM strip, and n the number of nodes with which the model is discretized. The values of $k_{C,ms}$ are obtained by attempts up to find the best fitting response with the experimental results.

A number of nodes n=64 is assumed on the base of the mesh sensitivity analysis performed for tensile model and discussed in the previous Section 4.1.2.

The numerical analysis are performed adopting controlled displacement mode by applying constant displacement increments at the free extremity of the fibre up to the ultimate displacement value. The convergence of the numerical analysis is achieved by assuming the Newton-Raphson algorithm with norm test of unbalance.

4.2.1 Results

The proposed model for predicting shear bond behaviour is validated against the experimental outcomes from shear bond tests on BFRCM and GFRCM presented at Chapter 2.

The main geometric and mechanical properties adopted in the model are resumed in Table 4.3 and 4.4, respectively.

Table 4.3: Geometric characteristics of the samples.

SAMPLE ID	GEOMETRY			
	t_m [mm]	t_f [mm]	B [mm]	L [mm]
BC_DSB1	10	0.039	50	260
BC_DSB2	10	0.039	100	320
BL_DSB1	10	0.039	50	260
BL_DSB2	10	0.039	100	320
GC_DSB1	10	0.04	50	260
GC_DSB1	10	0.04	50	260

Table 4.4: Mechanical properties assumed in the model.

SAMPLE ID	MATERIALS				INTERFACE		
	Mortar		Fibre		fibre-mortar		mortar-support
	$f_{m,t}$ [MPa]	E_m [GPa]	E_f [GPa]	ε_{fu} [%]	$k_{C,fm}$ [N/mm^3]	τ_{max} [MPa]	$k_{C,ms}$ [N/mm^3]
BC_DSB1	3.30	35.2	71.8	1.59	4.50	1.00	0.7
BC_DSB2	3.30	35.2	71.8	1.59	4.50	1.00	0.7
BL_DSB1	3.15	25.7	71.8	1.59	2.50	0.60	0.5
BL_DSB2	3.15	25.7	71.8	1.59	2.50	0.60	0.5
GC_DSB1	3.30	33.8	70.8	1.1	4.50	0.5	0.7
GL_DSB1	3.15	26.9	70.8	1.1	3.00	0.35	0.5

Where the tensile strength values assigned to mortar elements, i.e. $f_{m,t}$=3.30 MPa for cement-based mortar and $f_{m,t}$=3.15 MPa for lime-based mortar, are deduced from the average values of flexural strength referred to the corresponding batches.

The stiffness and the maximum shear stress values assigned to the fibre-mortar interface laws, as function of fibre-mortar combinations, are the same as those calibrated for tensile models. Exceptions are the maximum shear stress values assigned to the glass fibre-mortar interface of model GC_DSB1 and GL_DSB1. On this case, a lower values of τ_{max} is introduced in order to achieve the best fitting response.

The numerical-experimental comparisons in terms of stress-global displacement curves are reported in Figure 4.7 for BFRCM systems applied on calcarenite support and tested according to the two test set-ups, i.e. DSB1 and DSB2.

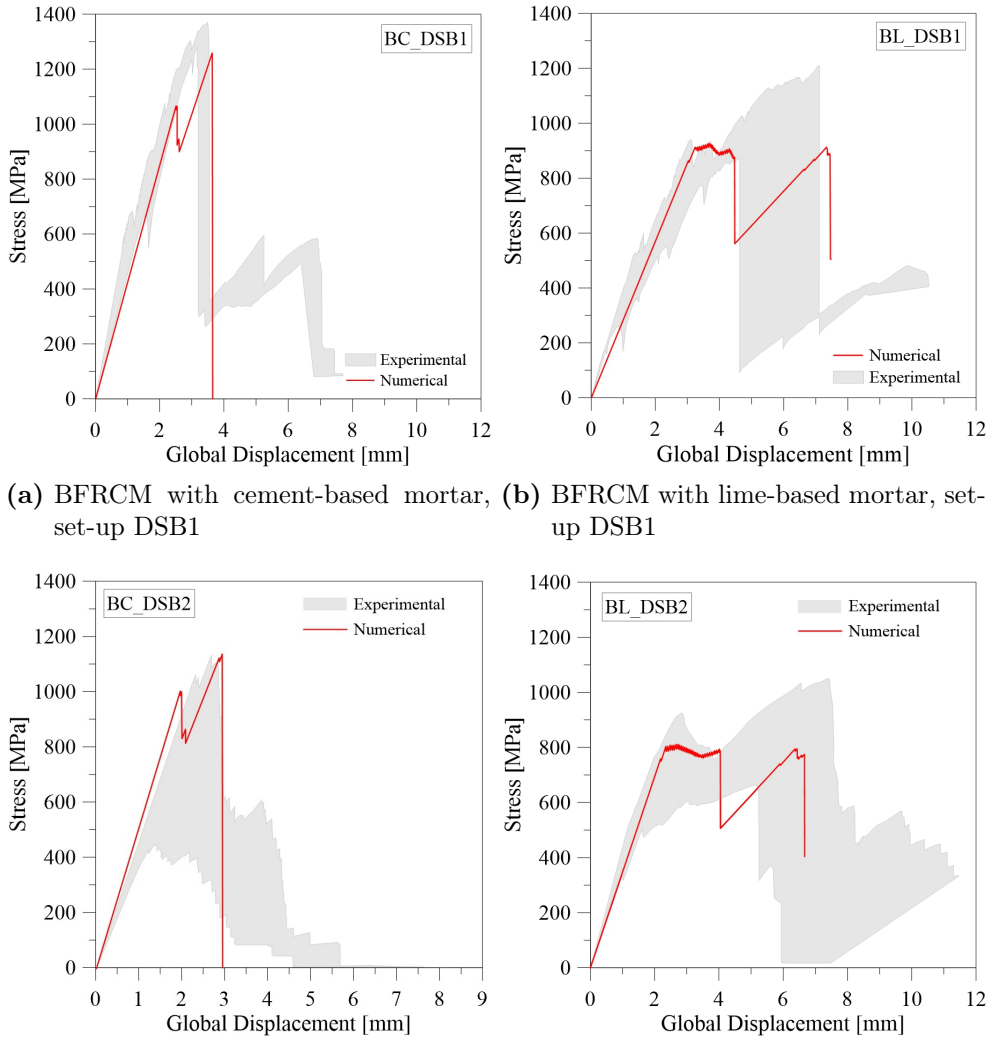

(a) BFRCM with cement-based mortar, set-up DSB1

(b) BFRCM with lime-based mortar, set-up DSB1

(c) BFRCM with cement-based mortar, set-up DSB2

(d) GFRCM with lime-based mortar, set-up DSB2

Figure 4.7: Numerical-experimental comparison in terms of stress-strain curves: shear bond behaviour of BFRCM composites applied on calcarenite support according to the two set-ups, DSB1 and DSB2.

It is worth pointing out that the proposed model is able to reproduce with good approximation the observed experimental response, in terms of stiffness

of the initial branch, up to the peak load.

Also the post-peak branch, observing in the curves referred to samples of group GL_DSB1 (Figure 4.7(b)) and GL_DSB2 (Figure 4.7(d)), is reproduced suitably. Predicted strengths and corresponding strains are in good accordance with the experimental averages.

Moreover, the model allows to take into account the influence of the fibre-mortar interface properties as function of the fibre-mortar combination (i.e. BC and BL), providing a certain repeatability of the numerical response also in function of different geometric features related to test set-ups.

The numerical-experimental comparisons for GFRCM systems applied on calcarenite support and tested according to the test set-up DSB1 are presented in Figure 4.8. In this case the best fitting response is obtained by assuming lower values of τ_{max} for fibre-mortar interface compared to the ones previous calibrated for tensile model. This discrepancy can be attributed to some drawbacks arisen during the test, as revealed by data recorded of the four transducers positioned on the two faces of the specimen.

Problems of eccentric load and uneven distribution of the stress along the two loaded fibre sections lead to limited exploitation of interface performances.

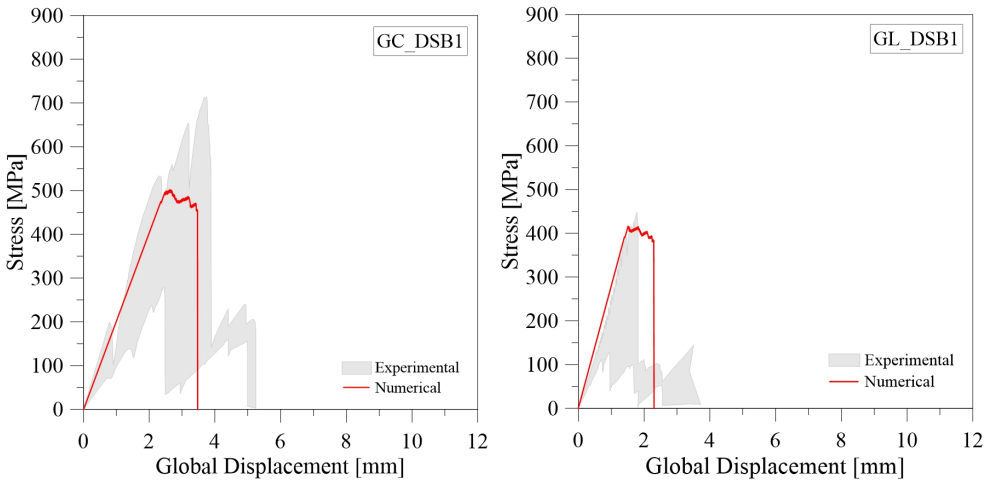

(a) GFRCM with cement-based mortar **(b)** GFRCM with lime-based mortar

Figure 4.8: Numerical-experimental comparison in terms of stress-strain curves: shear bond behaviour of GFRCM composites applied on calcarenite support.

If the values of τ_{max} provided from the calibration of tensile behaviour are

assumed, the results are those shown in Figure 4.9.

The numerical simulations highlight a gap of about the 25% and 57% between the predicted maximum strengths and the corresponding average experimental values calculated for GC_DSB1 and GL_DSB1, respectively.

Moreover, for model GC_DSB1 an overestimation of the tangent elastic modulus is observed: in particular, the theoretical value is about the +50% higher than the average experimental result.

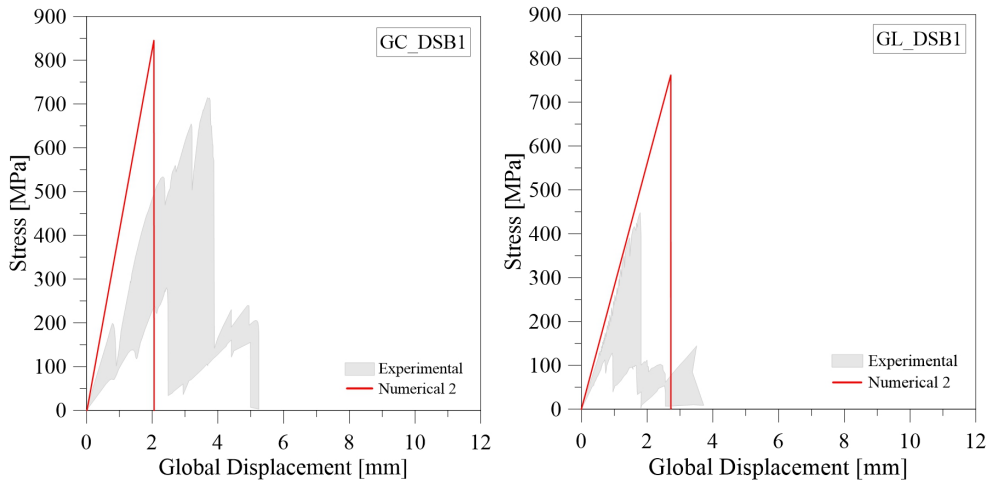

(a) GFRCM with cement-based mortar **(b)** GFRCM with lime-based mortar

Figure 4.9: Numerical-experimental comparison in terms of stress-strain curves: shear bond behaviour of GFRCM composites applied on calcarenite support.

Chapter 5

Conclusions and remarks

The goal of this thesis is to provide the constitutive characterization of different FRCM systems by studying the effect of different combinations of fibre textiles and inorganic matrices, obtained by varying the fibre nature (basalt and glass) and treatment (coating or use of adhesion promoter), mortar grade (with lime or cement-based binders) and setting method for tensile and bond tests. The bond properties of the aforementioned FRCM systems with the calcarenite stone support are investigated, providing new information about the compatibility between the FRCM and this kind of stone. For the scope, an innovative set-up is proposed to perform shear bond tests evaluating the effect of FRCM bond length and width.

Finally, a numerical investigation is carried out in order to support the extensive experimental investigation. The numerical study provides two proposed models for studying the tensile and bond behaviour through the use of truss and discrete shear interface FE.

The experimental program consists in the following parts:

- (1) test on material constituents, i.e. fibre and mortar;
- (2) tensile tests on BFRCM and GFRCM coupons, according to two test methods;
- (3) shear bond tests on FRCM systems applied on calcarenite substrate, according to the proposed set-up.

Tests on BFRCM and GFRCM composites are preceded by an extensive investigation on the mechanical properties of material constituents in order to relate the constitutive behaviour of the composites to the mechanical properties of the constituent materials: tensile tests of basalt and glass fibre grids

and flexural and compressive tests on mortar matrices (cement and lime based mortar).

The tensile tests on FRCM composites are addressed to an appropriate characterization of four series of BFRCM specimens and four of GFRCM, aiming to understand the best test set-up configuration with reference to two different gripping methods, and the influence of the mortar nature (cement or lime-based mortar) on the tensile stress-strain response of the composite strips.

The DIC technique is used to perform a strain full-field analysis on the surface of the FRCM coupons, allowing to investigate the uniform distribution of strains in specimens and the evolution of crack patterns during the test loading. On the basis of the obtained results by tensile tests on the FRCM composites, the following outcomes are highlighted :

- FRCM samples with high-strength cementitious matrix (i.e. cement-based mortar), lower fibre volume fractions and good mortar-fibre bond properties are unable to perform the typical tri-linear stress-strain response. Both BFRCM and GFRCM provide the exploitation of the maximum tensile strength of bare fibre textile, but the failure is achieved for values of strain lower than the 60% and 80% of the ultimate strain of fibre for specimens tested with clamping and clevis grip method, respectively;

- the average peak stresses of the four series of GFRCM specimens are found always higher compared to the peak stress of the dry glass grid, with an increase equal to 91% and 38% for BFRCM specimens with cement based-mortar, and 70% and 85% for BFRCM specimens with lime based-mortar, tested with clamping and clevis grip method, respectively;

- the stiffness of the third stage of the tensile curves for BFRCM and GFRCM with lime-based mortar proved to be slightly lower than the Young's modulus of the dry fibre textile. The gap is lower than the 10% when clevis grip method is adopted, and ranges between the 16% and 27% when clamping grip method is adopted;

- measurements from DIC analysis provide a stiffness of the first stage of the tensile curve greater than the 80% compared to that obtained from measurements provided by the testing machine. Differently, the stiffness of the third stage resulting from DIC measurements is lower than the 11.4 and 28.9 % compared to the measurements of testing machine for the specimens of group BL_TH and GL_TH, respectively;

- the crack pattern and the failure modes are influenced by the reinforcement ratio and the treatment of fibre. Specimens with an under-reinforced cross-section show the formation of one or maximum two cracks close to the gripping area and the observed failure mode is the fibre-rupture. Specimens of GFRCM with lime-based mortar fail due to fibre rupture after the formation of numerous cracks through the chemical fibre-matrix adhesion provided by the use of the applied promoter. Differently, the coated basalt textile establishes a lower bond with the lime-based mortar and fewer cracks develop in the free length of the specimens. In this case, the debonding at the fibre-mortar interface precedes the tensile failure of the basalt grid.

Subsequently, the attention is focused on the shear bond behaviour of aforementioned BFRCM and GFRCM composite systems applied on calcarenite support. Specimens are manufactured according to the proposal of an innovative double shear bond test set-up. Two different schemes are proposed with the aim of evaluating the influence of the bond length and width. Traditional measurement systems are adopted to evaluate the stress-slip relationship. Moreover, the DIC technique is also used in order to investigate on strain/displacement distribution on the upper mortar layer.

On the basis of the outcomes from double shear bond tests, the following conclusions can be drawn:

- double shear bond tests are repeatable and reproducible in particular in terms of peak stress when test set-up DSB1 is employed. The experimental outcomes from test set-up DSB1 provide values of the coefficient of variation ranging between the 2.8% and 12.1%, in absence of drawbacks mainly related on the manufacture of the samples, as observed in the case of the specimens of GFRCM with lime-based mortar (group GL_DSB1). While, the greatest scatter is mainly observed for slip values at peak stress (coefficient of variation of 31%) when the fibre slippage and the debonding at the fibre-mortar interface occur, as in the case of double shear bond tests on BFRCM with lime-base mortar applied on calcarenite support;

- generally, the exploitation ratio versus the tensile strength of the composite is much higher when good adhesion is established at the fibre-mortar interface. As observed for samples of BFRCM with cement-based mortar (group BC_DSB1) the peak stress of bonded fibres is about the 17% greater than peak stress of the composite in tension. In this case scatter

is reduced and the failure mode consists in the fibre rupture. Conversely, when other failure modes occur, involving the fibre slippage and the detachment of the external mortar layer, the scatter increases and the bond performance declines, as observed for samples of BFRCM with lime-based mortar (group BL_DSB1). Consequently, the exploitation ratio versus the tensile strength of the composite is lower than the 15%;

- the greatest scatter for specimens tested with set up DSB1 is recorded for samples of GFRCM with lime-based mortar (group GL_DSB1). In this case, the maximum peak stress values achieved in the bond tests are always lower than those attained in the tensile tests on bare textile, despite the observed failure mode is the fibre rupture in the un-bonded length. This result is imputable to the dry fibre textile that made the grid very sensitive to alignment problems, causing not uniform load conditions. Therefore, the reinforcement system is unable to provide the redistribution of the load when the most stressed fibre yarns fail. This is the cause of the high scattering of the results (coefficient of variation of 43.1%);

- for specimens tested with set-up DSB1, the DIC technique contributed to identify slipping phenomena at the fibre-mortar interface. It is evident for FRCM strengthening systems with lime-based mortar. Conversely, for both types of grid (basalt and glass) a more effective local bond behaviour is achieved whit cement-based mortar.

- by increasing the bond length and width of the FRCM strip, i.e. adopting test set-up DSB2, the main failure modes observed are the same as those of scaled samples (set-up DSB1). However, a certain scatter is observed. For peak stress values, the coefficient of variation increases up to the 30.3% for specimens of BFRCM with cement based-mortar (group BC_DSB2) and the 19.6% for specimens of BFRCM with lime based-mortar (group BL_DSB2). The efficiency of this systems, evaluated through the exploitation ratio versus the tensile strength of the composite, is about the 71% when the failure occurs due to the tensile fibre rupture out of the bond length for specimens of BFRCM with cement-based mortar. While, a lower efficiency of about the 67% is associated to the occurrence of fibre slippage and debonding at the fibre-mortar interface for specimens of BFRCM with lime-based mortar.

On the basis of the discussed results it is evident that the bond behaviour

(strength and failure mode) strictly depends on the fibre nature and the fibre-mortar interaction, the mechanical characteristic of the matrix, the manufacture of the samples and the experimental set-up. In details: - a relatively low chemical compatibility between fibre and mortar may provide the slippage of the fibre grid within the matrix, however the use of adhesion promoter allows to improve the bond strength between matrix and fibre; - the correct alignment ensures the reliability and repeatability of the test results; - scaled set-up DSB1 provides reliable response, so it can be considered a well easy alternative to the manufacturing of samples with a more larger size involving a more complex and less manageable set-up (DSB2).

Moreover, it is worth pointing out that unconventional strain/displacement measurement methods, such as DIC technique, are emerging as promising solution to be integrated with traditional devices, in order to detect local behaviour of fibre-mortar interaction characterized by complex shear stress transfer mechanisms.

Finally, the effectiveness of two proposed 1D numerical models are validated against the experimental results from tensile and shear bond tests. The numerical model reproduces with good approximation the observed experimental tensile and shear bond behaviour. It is a very simplified model based of few variables, easily to deduce. However, other comparisons with experimental results would be necessary in order to achieve a proper calibration of the interface parameters.

Further investigations are suggested to study the tensile behaviour of BFRCM and GFRCM with cement-based mortar, assuming a lower thickness of the mortar, in order to allow the exploitation of the typical tri-linear trend. These results are request to set a proper comparison with the outcomes from samples of BFRCM and GFRCM with lime-based mortar, in order to investigate the influence of the mortar nature (cementitious or lime based) on the tensile behaviour.

Moreover, it may be interesting to improve the shear bond test set-up for GFRCM systems applied of calcarenite support, in order to avoid the problems related to the misalignment of dry fibre, for example by impregnating the unbonded fibre strip with an epoxy resin.

Bibliography

[1] A. Bellini, M. Bovo, C. Mazzotti, Experimental and numerical evaluation of fiber-matrix interface behaviour of different FRCM systems, Composites Part B: Engineering 161 (2019) 411–426.

[2] A. Committee, et al., Guide to design and construction of externally bonded fabric-reinforced cementitious matrix and steel-reinforced grout systems for repair and strengthening of concrete structures; ACI 549.4 R-20; ACI: Farmington hills, MI, USA, (2020).

[3] J. Donnini, G. Chiappini, G. Lancioni, V. Corinaldesi, Tensile behaviour of glass FRCM systems with fabrics overlap: Experimental results and numerical modeling, Composite structures 212 (2019) 398–411.

[4] RILEM Technical Committee 232-TDT. Recommendation of RILEM TC 232- TDT: test methods and design of textile reinforced concrete: uniaxial tensile test: test method to determine the load bearing behavior of tensile specimens made of textile reinforced concrete, Materials and Structures 49 (12) (2016) 4923–4927.

[5] H.-S. Kim, G. T. Truong, S.-H. Park, K.-K. Choi, Tensile properties of carbon fiber-textile reinforced mortar (TRM) characterized by different anchorage methods, International Journal of Concrete Structures and Materials 12 (1) (2018) 1–13.

[6] T. D'Antino, C. Papanicolaou, Mechanical characterization of textile reinforced inorganic-matrix composites, Composites Part B: Engineering 127 (2017) 78–91.

[7] G. De Felice, M. A. Aiello, C. Caggegi, F. Ceroni, S. De Santis, E. Garbin, N. Gattesco, Ł. Hojdys, P. Krajewski, A. Kwiecień, et al., Recommendation of RILEM Technical Committee 250-CSM: Test method for textile

reinforced mortar to substrate bond characterization, Materials and Structures 51 (4) (2018) 1–9.

[8] CSLLPP, Italian guideline for the identification, qualification and acceptance control of fibre reinforced cementitious matrix (FRCM) used for the structural consolidation of existing constructions (2018).

[9] A. Hedayat, S. Ashur, Digital image correlation and its application in an undergraduate civil engineering materials laboratory, US: Fort Wayne (2015).

[10] D. Arboleda, F. G. Carozzi, A. Nanni, C. Poggi, Testing procedures for the uniaxial tensile characterization of fabric reinforced cementitious matrix (FRCM) composites, J. Compos. Constr 20 (2016) 04015063.

[11] T. D'antino, C. C. Papanicolaou, Comparison between different tensile test set-ups for the mechanical characterization of inorganic-matrix composites, Construction and Building Materials 171 (2018) 140–151.

[12] AC434-ICC-evaluation service: Acceptance criteria for masonry and concrete strengthening using fiber-reinforced cementitious matrix (FRCM) composite systems AC434:2013 (2013).

[13] R. Contamine, A. S. Larbi, P. Hamelin, Contribution to direct tensile testing of textile reinforced concrete (TRC) composites, Materials Science and Engineering: A 528 (29-30) (2011) 8589–8598.

[14] S. De Santis, F. G. Carozzi, G. de Felice, C. Poggi, Test methods for textile reinforced mortar systems, Composites Part B: Engineering 127 (2017) 121–132.

[15] C. Caggegi, E. Lanoye, K. Djama, A. Bassil, A. Gabor, Tensile behaviour of a basalt TRM strengthening system: Influence of mortar and reinforcing textile ratios, Composites Part B: Engineering 130 (2017) 90–102.

[16] M. Tekieli, S. De Santis, G. de Felice, A. Kwiecień, F. Roscini, Application of digital image correlation to composite reinforcements testing, Composite Structures 160 (2017) 670–688.

[17] G. P. Lignola, C. Caggegi, F. Ceroni, S. De Santis, P. Krajewski, P. B. Lourenço, M. Morganti, C. C. Papanicolaou, C. Pellegrino, A. Prota, et al., Performance assessment of basalt FRCM for retrofit applications on masonry, Composites Part B: Engineering 128 (2017) 1–18.

[18] C. Carloni, T. D'Antino, L. Sneed, C. Pellegrino, Role of the matrix layers in the stress-transfer mechanism of FRCM composites bonded to a concrete substrate, J. Eng. Mech 141 (6) (2015) 04014165.

[19] T. D'Antino, C. Carloni, L. Sneed, C. Pellegrino, Matrix-fiber bond behavior in PBO FRCM composites: A fracture mechanics approach, Engineering Fracture Mechanics 117 (2014) 94–111.

[20] A. D'Ambrisi, L. Feo, F. Focacci, Experimental analysis on bond between pbo-frcm strengthening materials and concrete, Composites Part B: Engineering 44 (1) (2013) 524–532.

[21] L. Sneed, T. D'Antino, C. Carloni, C. Pellegrino, A comparison of the bond behavior of PBO-FRCM composites determined by double-lap and single-lap shear tests, Cement and Concrete Composites 64 (2015) 37–48.

[22] S. Barducci, V. Alecci, M. De Stefano, G. Misseri, L. Rovero, G. Stipo, Experimental and analytical investigations on bond behavior of basalt-FRCM systems, Journal of Composites for Construction 24 (1) (2020) 04019055.

[23] F. G. Carozzi, A. Bellini, T. D'Antino, G. de Felice, F. Focacci, Ł. Hojdys, L. Laghi, E. Lanoye, F. Micelli, M. Panizza, et al., Experimental investigation of tensile and bond properties of carbon-FRCM composites for strengthening masonry elements, Composites Part B: Engineering 128 (2017) 100–119.

[24] A. Bellini, M. A. Aiello, F. Bencardino, C. B. de Carvalho Bello, G. Castori, A. Cecchi, F. Ceroni, M. Corradi, T. D'Antino, S. De Santis, et al., Influence of different set-up parameters on the bond behavior of FRCM composites, Construction and Building Materials 308 (2021) 124964.

[25] J. D'Anna, G. Amato, J. F. Chen, G. Minafò, L. La Mendola, Experimental application of digital image correlation for the tensile characterization of basalt FRCM composites, Construction and Building Materials 271 (2021) 121770.

[26] M. Leone, M. A. Aiello, Bond tests on clay bricks and natural stone masonry externally bonded with FRP, Materials 14 (23) (2021) 7439.

[27] P. Larrinaga, C. Chastre, H. C. Biscaia, J. T. San-José, Experimental and numerical modeling of basalt textile reinforced mortar behavior under uniaxial tensile stress, Materials & Design 55 (2014) 66–74.

[28] L.-L. Wei, J.-H. Zhu, T. Ueda, M.-N. Su, J. Liu, W. Liu, L.-P. Tang, F. Xing, Tensile behaviour of carbon fabric reinforced cementitious matrix composites as both strengthening and anode materials, Composite Structures 234 (2020) 111675.

[29] E. Bertolesi, F. G. Carozzi, G. Milani, C. Poggi, Numerical modeling of fabric reinforce cementitious matrix composites (frcm) in tension, Construction and Building Materials 70 (2014) 531–548.

[30] C. Caggegi, F. G. Carozzi, S. De Santis, F. Fabbrocino, F. Focacci, Ł. Hojdys, E. Lanoye, L. Zuccarino, Experimental analysis on tensile and bond properties of PBO and aramid fabric reinforced cementitious matrix for strengthening masonry structures, Composites Part B: Engineering 127 (2017) 175–195.

[31] F. Bompadre, J. Donnini, Fabric-reinforced cementitious matrix (FRCM) carbon yarns with different surface treatments embedded in a cementitious mortar: Mechanical and durability studies, Materials 15 (11) (2022) 3927.

[32] G. Ferrara, C. Caggegi, A. Gabor, E. Martinelli, Experimental study on the adhesion of basalt textile reinforced mortars (TRM) to clay brick masonry: the influence of textile density, Fibers 7 (12) (2019) 103.

[33] G. Minafò, L. La Mendola, Experimental investigation on the effect of mortar grade on the compressive behaviour of FRCM confined masonry columns, Composites Part B: Engineering 146 (2018) 1–12.

[34] J. Aveston, G. Cooper, A. Kelly, Single and multiple fracture, the properties of fibre composites, Proceedings of the conference national physical laboratories (1971) 15–24.

[35] B. Massicotte, A. E. Elwi, J. G. MacGregor, Tension-stiffening model for planar reinforced concrete members, Journal of Structural Engineering 116 (11) (1990) 3039–3058.

[36] M. C. Oddo, G. Minafò, L. La Mendola, Constitutive models for the tensile behaviour of TRM materials: Literature review and experimental verification, Materials 14 (3) (2021) 700.

[37] A. Monaco, G. Minafò, J. D'Anna, M. C. Oddo, L. La Mendola, Constitutive numerical model of FRCM strips under traction, Frontiers in Built Environment 6 (2020) 60.

[38] F. Nerilli, S. Marfia, E. Sacco, Micromechanical modeling of the constitutive response of frcm composites, Construction and Building Materials 236 (2020) 117539.

[39] A. Monaco, J. D'Anna, M. C. Oddo, G. Minafò, L. La Mendola, Numerical modelling of the tensile behaviour of BFRCM strips, in: Key Engineering Materials, Vol. 817, Trans Tech Publ, (2019), pp. 15–22.

[40] G. Milani, E. Grande, Simple bisection procedure in quickly convergent explicit ODE solver to numerically analyze FRCM strengthening systems, Composites Part B: Engineering 199 (2020) 108322.

[41] ISO13934-1-determination of tensile strength of textile fabric with universal tensile strength test method ISO13934-1:2013 (2013).

[42] EN1015-11-methods of test for mortar for masonry–part 11: Determination of flexural and compressive strength of hardened mortar EN1015-11 (1999).

[43] Calcarenite stone - Technical data sheet (2022).
URL https://www.pietrasabucina.it/pietra-di-sabucina

[44] M. Zimbardo, N. Nocilla, A. Evangelista, M. Ramondini, A. Scotto di Santolo, Destructuration of typical sicilian calcarenites, Bulletin of Engineering Geology and the Environment 70 (3) (2011) 507–515.

[45] EN1926-natural stone test methods - determination of uniaxial compressive strength EN 1926 (2006).

[46] Planitop HDM MAXI - Technical data sheet (2022).
URL https://www.mapei.com/it/it/prodotti-e-soluzioni/prodotti/dettaglio/planitop-hdm-maxi

[47] Planitop HDM RESTAURO - Technical data sheet (2022).
URL https://www.mapei.com/it/it/prodotti-e-soluzioni/prodotti/dettaglio/planitop-hdm-restauro

[48] Mapewrap 31 - Technical data sheet (2022).
URL https://www.mapei.com/it/it/prodotti-e-soluzioni/prodotti/dettaglio/mapewrap-31

[49] M. Accardi, C. Cucchiara, L. La Mendola, Bond behavior between CFRP strips and calcarenite stone, in: Proceedings of the 6th international conference on fracture mechanics of concrete and concrete structures, Catania, Italy, 2007, pp. 17–22.

[50] Mapewrap 1 - Technical data sheet (2022).
URL https://www.mapei.com/it/it/prodotti-e-soluzioni/prodotti/dettaglio/mapewrap-primer-1

[51] Mapewrap 11 - Technical data sheet (2022).
URL https://www.mapei.com/it/it/prodotti-e-soluzioni/prodotti/dettaglio/mapewrap-11

[52] M. Sutton, C. Mingqi, W. Peters, Y. Chao, S. McNeill, Application of an optimized digital correlation method to planar deformation analysis, Image and Vision Computing 4 (3) (1986) 143–150.

[53] J. D'Anna, G. Amato, J. F. Chen, G. Minafò, L. La Mendola, On the use of Digital Image Correlation (DIC) for evaluating the tensile behaviour of BFRCM strips, in: Key Engineering Materials, Vol. 817, Trans Tech Publ, (2019), pp. 377–384.

[54] A. Bilotta, F. Ceroni, G. Lignola, A. Prota, Use of DIC technique for investigating the behaviour of FRCM materials for strengthening masonry elements, Composites Part B: Engineering 129 (2017) 251–270.

[55] B. Pan, K. Qian, H. Xie, A. Asundi, Two-dimensional digital image correlation for in-plane displacement and strain measurement: a review, Measurement science and technology 20 (6) (2009) 062001.

[56] B. Pan, H. Xie, Z. Wang, Equivalence of digital image correlation criteria for pattern matching, Applied optics 49 (28) (2010) 5501–5509.

[57] J. Blaber, B. Adair, A. Antoniou, Ncorr: open-source 2d digital image correlation matlab software, Experimental Mechanics 55 (6) (2015) 1105–1122.

[58] B. Pan, Z. Wang, Z. Lu, Genuine full-field deformation measurement of an object with complex shape using reliability-guided digital image correlation, Optics express 18 (2) (2010) 1011–1023.

[59] B. Pan, Reliability-guided digital image correlation for image deformation measurement, Applied optics 48 (8) (2009) 1535–1542.

[60] B. Pan, A. Asundi, H. Xie, J. Gao, Digital image correlation using iterative least squares and pointwise least squares for displacement field and strain field measurements, Optics and Lasers in Engineering 47 (7-8) (2009) 865–874.

[61] H. W. Schreier, J. R. Braasch, M. A. Sutton, Systematic errors in digital image correlation caused by intensity interpolation, Optical engineering 39 (11) (2000) 2915–2921.

[62] B. Pan, K. Li, A fast digital image correlation method for deformation measurement, Optics and Lasers in Engineering 49 (7) (2011) 841–847.

[63] The MathWorks Inc., MATLAB R2021a (2021).
URL https://matlab.mathworks.com/

[64] V. Nežerka, Ncorr_post: DIC Post−Processing Tool (2014).
URL http://mech.fsv.cvut.cz/nezerka/dic/index.htm

[65] J. D'Anna, G. Amato, J. Chen, G. Minafò, L. La Mendola, Effects of different test setups on the experimental tensile behaviour of basalt fibre bidirectional grids for FRCM composites, Fibers 8 (11) (2020) 68.

[66] M. Zhu, F. McKenna, M. H. Scott, Openseespy: Python library for the opensees finite element framework, SoftwareX 7 (2018) 6–11.

[67] F. McKenna, Opensees: a framework for earthquake engineering simulation, Computing in Science & Engineering 13 (4) (2011) 58–66.

[68] N. Mordà, A. Mancini, Norme tecniche per le costruzioni (ntc 2018) d. min. infrastrutture e trasporti 17 gennaio 2018 (2018).

[69] E. Grande, G. Milani, Numerical simulation of the tensile behavior of FRCM strengthening systems, Composites Part B: Engineering 189 (2020) 107886.

[70] G. Van Rossum, F. L. Drake, Python 3 reference manual (2009).

[71] C. R. Harris, K. J. Millman, S. J. Van Der Walt, R. Gommers, P. Virtanen, D. Cournapeau, E. Wieser, J. Taylor, S. Berg, N. J. Smith, et al., Array programming with numpy, Nature 585 (7825) (2020) 357–362.

[72] J. D. Hunter, Matplotlib: A 2D graphics environment, Computing in science & engineering 9 (03) (2007) 90–95.

[73] E. Grande, G. Milani, Procedure for the numerical characterization of the local bond behavior of FRCM, Composite Structures 258 (2021) 113404.

ACKNOWLEDGEMENTS

This thesis is the product of three intense years of work, but also personal and professional growth, during which I had the good luck to be supported by people whom I feel like I need to thank.

First and foremost, I am extremely grateful to my supervisors, Prof. Lidia La Mendola and Prof. Giovanni Minafò for their invaluable advice and unconditional support. Their immense knowledge and plentiful experience have encouraged me in all the time of my academic research and daily life.

My gratitude extends to my foreign supervisor, Prof. Chaterine Papanicolaou for her treasured support which was really influential in shaping my experiment methods and critiquing my results.

I feel like thanking the lab technician, Eng. Erasmo Cataldo for his technical support on my experimental work and his kind help that have made my laboratory life a wonderful time.

Additionally, I would like to express gratitude to the PhD Coordinator, Prof. Antonina Pirrotta for all her help and availability with this PhD.

I enjoyed the time spent in the company of my colleague Gaetano Camarda. Thanks for your tremendous encouragement and your great-heartedness.

My special thanks to Dario e all my friends, Mary, Valeria, Luisa, Ilaria, Lory, Fabiola.

Last but not least, I will never thank enough my wonderful family: my little brother Marco for his unconditional love; Claudia, Maria, Enza, Rosalia, my beautiful aunt Nunzia and all the others.

RINGRAZIAMENTI

Questa tesi è il frutto di tre anni di intenso lavoro, ma anche e soprattutto di crescita personale e professionale, durante la quale ho avuto la fortuna di essere stata costantemente sostenuta da persone che mi sento in dovere di ringraziare.

In primis, sono estremamente grata ai miei supervisori e tutors, Prof. Lidia La Mendola e Prof. Giovanni Minafò, grazie per i vostri preziosi consigli e il sostegno incondizionato che mi avete dato. La vostra immensa conoscenza e la vostra incommensurabile esperienza mi hanno incoraggiato durante tutto il mio percorso accademico e sopratutto nella vita quotidiana.

La mia gratitudine si estende anche al mio supervisore straniero Prof. Chaterine Papanicolaou, per il suo prezioso sostegno che è stato davvero influente nel plasmare i miei metodi di prova sperimentale e nel criticare in maniera costruttiva i miei risultati.

Mi sento di ringraziare il tecnico di laboratorio, Ing. Erasmo Cataldo, per il suo supporto tecnico durante tutto il mio studio sperimentale e il suo gentile aiuto, che hanno reso la mia vita di laboratorio un momento meraviglioso.

Inoltre, vorrei esprimere la mia gratitudine al Coordinatore del Dottorato, la Prof. Antonina Pirrotta per tutto il suo aiuto e la sua disponibilità.

Ho apprezzato molto il tempo trascorso in compagnia del mio collega di stanza Gaetano Camarda. Grazie per il tuo enorme incoraggiamento e il tuo grande cuore.

Un ringraziamento speciale va anche a Dario e a tutte le mie amiche, Mary, Valeria, Luisa, Ilaria, Lory, Fabiola.

Ultimi ma non meno importanti, non ringrazierò mai abbastanza la mia meravigliosa famiglia: il mio fratellino Marco per il suo amore incondizionato; Claudia, Maria, Enza, Rosalia, la mia stupenda zia Nunzia e tutti gli altri.